TECHNISCHE UNIVERSITÄT WIEN

HEPHY INSTITUT FÜR HOCHENERGIEPHYSIK

DIPLOMARBEIT

Investigation of ultra fast silicon detectors for ion imaging methods

zur Erlangung des akademischen Grades

Diplom-Ingenieur

im Rahmen des Studiums

Technische Physik

eingereicht von

Manuel Ruckerbauer, BSc
Matrikelnummer 01455153

ausgeführt am Atominstitut
der Fakultät für Physik der Technischen Universität Wien
in Zusammenarbeit mit dem Institut für Hochenergiephysik

Betreuung
Betreuer: Privatdoz. Dipl.-Ing. Dr.techn. Christoph Schwanda
Mitwirkung: Univ.Lektor Dipl.-Ing. Dr.techn. Thomas Bergauer

Wien, 27.2.2021

Unterschrift Verfasser

Unterschrift Betreuer

Abstract

MedAustron is a new medical facility in which cancer patients are successfully treated by the use of irradiation with charged particles. For the treatment planning, medical imaging methods are used to establish a 3D image of the tumor volume and its surroundings. Currently, conventional computer tomography (CT) based on X-rays is used. Due to the different interaction mechanisms of X-rays and charged particles, uncertainties are introduced. An imaging modality based on the same charged particles could reduce these uncertainties and, as a consequence, results in a higher medical success. Such an imaging process is referred to as proton- or ion-CT. Here, protons (or ions) with energies well above the ones used for treatment pass through the patient and lose energy in the process. The residual energy and deflection of the particles are then measured to reconstruct the energy loss along the traversed path. Tracking detectors are used to measure the direction of the traversing particle and the energy is obtained by a calorimeter. In this work, the use of a time-of-flight calorimeter based on a novel semiconductor detector technology is investigated. In such a setup, the residual energy is measured indirectly by the time a particle needs to pass a fixed distance. The duration of the process is then measured by ultra fast silicon detectors, often referred to as Low Gain Avalanche Detectors (LGAD), which are currently being prepared for use at CERN's CMS experiment. The aim of this master thesis is to characterize and optimize a time-of-flight setup for pCT, based on the above-mentioned silicon detectors.

Zusammenfassung

MedAustron ist eine neue medizinische Einrichtung, in der Krebspatienten mithilfe von Teilchenstrahlung erfolgreich behandelt werden. Für die Bestrahlungsplanung werden bildgebende Verfahren verwendet, um ein 3D-Bild des Tumors und dessen umliegendes Gewebe zu erstellen. Die Erstellung dieser Bilder wird zurzeit mittels Computer Tomographie (CT), also mit Röntgenstrahlung durchgeführt. Aufgrund der unterschiedlichen Wechselwirkung mit Materie durch Photonenstrahlung als Bildgebung und der Teilchenstrahlung zur Behandlung gibt es Unsicherheiten bei der Genauigkeit der Bestrahlung. Wenn man die Bildgebung nun auch mit Teilchenstrahlung durchführen könnte, wäre die Behandlung von Tumoren aufgrund höherer Genauigkeit medizinisch erfolgreicher. Ionen-Computer-Tomographie bzw. Protonen-Computer-Tomographie (pCT) sind solche bildgebenden Verfahren an denen zurzeit geforscht wird. Dabei werden Protonen (oder Ionen) mit viel höherer Energie als bei der Strahlentherapie durch den Patienten geschickt und verlieren durch die Wechselwirkung mit der Materie an Energie. Die Restenergie und die Ablenkung der Teilchen werden gemessen, um den Energieverlust entlang des Pfades zu rekonstruieren. Dafür werden einerseits ein Kalorimeter zur Energiebestimmung und sogenannte Tracking Detektoren für das Messen der Ablenkung der Teilchen benötigt. In dieser Arbeit wurde die Messung der Restenergie über ein Time-of-flight Kalorimeter durchgeführt, welches auf neuartiger Halbleiterdetektortechnologie basiert. In solch einem Messaufbau kann die benötigte Restenergie indirekt über eine Messung der Zeit erfolgen, die das durchtretende Teilchen für eine bestimmte Strecke benötigt. Diese Zeit wird von LGADs (Low Gain Avalanche Detector) gemessen, die aufgrund ihrer verbesserten Zeitauflösung aktuell gerade für den Einsatz für das CMS Experiment am CERN vorbereitet werden. Das Ziel dieser Diplomarbeit ist die Charakterisierung und die Optimierung dieser Silizium Detektoren für bildgebende Verfahren in der medizinischen Anwendung.

Contents

1 Introduction and Motivation

The idea of proton therapy was started by Harvard physicist Robert Wilson in 1946 and the first patients were treated with protons in 1955 [1]. Nowadays, proton treatments are carried out in hospital-based facilities and in 2016, the first patients in Austria were treated with protons at the MedAustron facility [2]. In cancer treatment the first paradigm is that the maligne tissue is damaged while the surrounded healthy tissue should be spared. Irradiation with photons is the most common technique, because it is cheaper and the infrastructure is more compact when compared to the irradiation with ions. The latter is superior to photons, because of its energy loss properties, but the infrastructure is technically extensive and therefore rare.

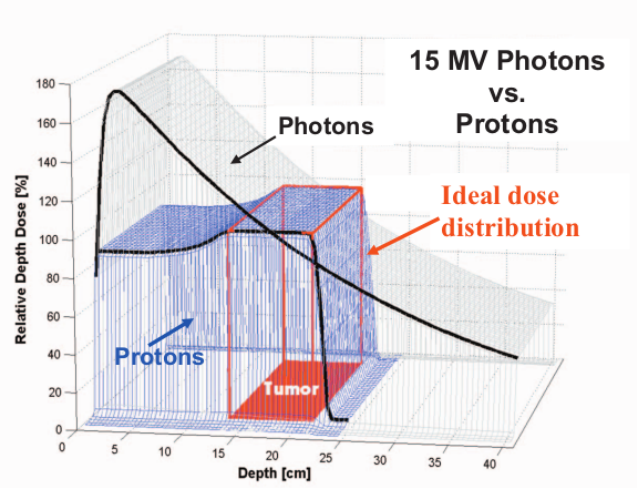

Figure 1: Depth dose curves of photons and protons. The red area is the target volume for the ideal dose distribution. The abruptly dropping of the proton dose is the great advantage over photons [2].

While the dose distribution of photons follow a sharp rise and a gentle decrease when entering the body, protons show a smooth rise and an abrupt drop. This property of the dose distribution can be used to focus the proton's energy in a volume that is needed for energy deposition and the killing of tumorous cells (Fig. 1). The precondition is that the treatment plan, based on an image of the tumor, is accurate. The range of protons in the patient is dependent on their energy and the stopping power of the tissue they traverse. With the information of the different stopping power in different tissues inside a body, an RSP map can be drawn. RSP stands for relative stopping power and describes the stopping power of protons relative to water. Conventional imaging methods are based on X-ray irradiation which use linear attenuation coefficients. To get the final RSP images, an additional conversion step is needed and this calibration process introduces uncertainties of up to 3.5% [3]. These uncertainties reduce the quality of the image and decrease the precision of the whole treatment [4]. Especially for tumors located on critical locations such as the optical nerve or the spinal chord, a very high precision of the dose distribution is crucial. To improve the accuracy, pCT is used to measure the RSP directly, which can be processed by reconstruction algorithms and deliver three-dimensional RSP maps that subsequently achieve an RSP accuracy of 1.39% [3].

In order to obtain information of the RSP, a tracker system for the ion's directions and a calorimeter for measuring the residual energy of the ions is needed. This work investigates the possibility of replacing the calorimeter by a time-of-flight setup. With this type of setup, the residual energy is obtained by the time a particle needs for a specified length. The time resolution required for such a measurement can be achieved by LGADs (Low Gain Avalanche Detectors). These instruments are based on the same principle as common semiconductor diodes: When radiation hits the diode, electron-hole-pairs are created and can then be processed into an additional electronic circuit. In addition, LGADs use internal gain structures to amplify the signal, thus improving S/N (signal to noise) and consequently, the time resolution.

For a structured approach of this novel imaging method with a time-of-flight calorimeter this work is mainly split into two parts:

- The experimental part will cover the characterisation and performance studies on the LGADs and their usage in pCT.
- The simulation part examines the design of the beam experiment with software tools and simulates the time-of-flight setup by adjusting the free parameters in order to improve the experiment.

2 Theoretical Background

2.1 Proton Computed Tomography (pCT)

2.1.1 Computed Tomography (CT)

Ion beam therapy is technically challenging because it requires a lot of technical equipment: a particle accelerator, the associated facility, as well as highly trained personnel. As already stated in Sec. 1, the common imaging approach is done via X-rays even in facilities, where appropriate infrastructure is available. However, the imaging process implicates uncertainties, mainly due to the calibration process. According to the Beer-Lambert Law (eq. 2.17), μ is the attenuation coefficient depending on the traversed material and has to be obtained by normalizing it to the coefficients of water and air. These normalized attenuation coefficients are given in Hounsfield units (HU) represented by a greyscale.

$$HU = \frac{\mu - \mu_{\text{water}}}{\mu_{\text{water}} - \mu_{\text{air}}} \times 1000 \tag{2.1}$$

In order to obtain the information of the stopping power, the HU, which are based on photon interaction with the target material, needs to be converted into an RSP map. This conversion leads to uncertainties of up to 3.5%, which can be translated into a spatial resolution of a few millimeters [4]. In ion beam therapy, these uncertainties lead to either insufficiently irradiated tumors, or in the worst case, the irradiation of healthy tissue, which should stay intact. Imprecisions like these can cause fatal consequences when treating tumors seated in sensitive areas such as the spinal cord, the optical nerve or complex areas in the brain. In order to address these problems, the idea of ion imaging comes into play using protons, $^{12}C^{6+}$ carbon ions and alpha particles.

2.1.2 RSP map

The advantage of pCT over CT with X-rays is the direct measurement of the stopping power. To obtain the stopping power inside the patients body, the following equations give a short overview, while a detailed determination is presented in [5]. The linear stopping power S over a path length $\mathrm{d}l$ at a point (x, y) equals the energy loss $\mathrm{d}E$ of a charged particle with energy E.

$$-\,\mathrm{d}E = S(x, y, E)\mathrm{d}l \tag{2.2}$$

When introducing the density of the material ρ, the mass stopping power can be defined based on eq. 2.2

$$-\,\frac{S}{\rho}(x, y, E_0)\mathrm{d}E = \frac{S}{\rho}(x, y, E_0)\frac{S}{\rho}(x, y, E)\rho(x, y)\mathrm{d}l \tag{2.3}$$

where E_0 is the particle's initial energy. Eq. 2.3 can be rewritten by the help of dividing it by $\frac{S}{\rho}(x, y, E)$ as follows

$$-\frac{\frac{S}{\rho}(x,y,E_0)}{\frac{S}{\rho}(x,y,E)}\mathrm{d}E = S(x,y,E_0)\mathrm{d}l \tag{2.4}$$

According to [5], where the density is stated to be $\rho < 6 \cdot 10^{-3}$, the left side of Eq. 2.4 can be replaced by the known stopping power ratio for water [6].

$$-\left[\frac{S}{\rho}(H_2O)\right]_E^{E_0} = S(x,y,E_0)\mathrm{d}l \tag{2.5}$$

with

$$\left[\frac{S}{\rho}(H_2O)\right]_E^{E_0} \cong \left[\frac{S}{\rho}(x,y)\right]_E^{E_0} = \frac{\frac{S}{\rho}(x,y,E_0)}{\frac{S}{\rho}(x,y,E)} \tag{2.6}$$

Finally, the tomographic equation can be found by integrating Eq. 2.5 along the ion path:

$$-\int_{E_{in}}^{E_{out}}\left[\frac{S}{\rho}(H_2O)\right]_E^{E_0}\mathrm{d}E = \int_{path} S(x,y,E_0)\mathrm{d}l \tag{2.7}$$

where the path of the ion beam can be obtained either by the straight line (SL), cubic spline, or the most likely path (MLP) approach. The initial energy E_{in} is fixed by the accelerator settings and potential material in front of the patient and E_{out} is measured by a calorimeter.
For calculating the CT projections out of Eq. 2.7 with computational iterative reconstruction algorithms, it needs to be discretized by dividing the phantom into N pixels:

$$p_i = -\int_{E_{in}}^{E_{out}}\left[\frac{S}{\rho}(H_2O)\right]_E^{E_0}\mathrm{d}E = \sum_{j=i}^{N} w_{ij}S_j(E_0) \tag{2.8}$$

with w_{ij} being the path length of proton i in pixel j and $S_j(E_0)$ the stopping power respectively. In the end, this set of equation with size N_p and N unknowns needs to be solved for a successful creation of the RSP map.

The path of the ion can be estimated for example with the MLP approach mentioned earlier, but is not part of this work. For further details on path estimations, see the following references: [5] [7] [8] [9].

2.1.3 pCT Setup

In Fig. 2, a typical pCT setup is shown where the incoming ion beam is detected by the first two trackers. Subsequently, it undergoes scattering processes inside the patient's body and afterwards, the deflection and the residual energy of the beam is monitored by the last two trackers and the calorimeter respectively. The part of the patients body which is of interest for therapy, often just referred to as "phantom", needs to be rotated in a specified angle and irradiated again. This process is repeated until the 3D image can be reconstructed.

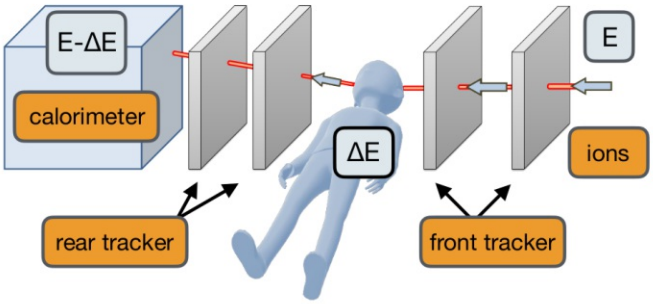

Figure 2: Overview of a pCT setup containing two front and two rear trackers to obtain the beam deflection, a phantom between the front- and rear trackers and a calorimeter, in which the residual energy of the ion beam is measured.

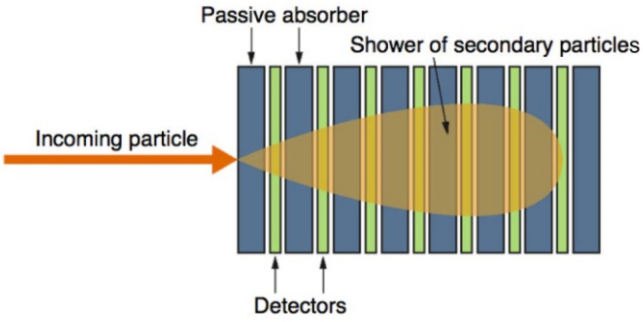

Figure 3: Schematic view of a sampling calorimeter consisting of slices of passive absorbers and detectors. The incoming particle deposits its energy as a secondary particle shower that is monitored by the detectors [10].

The energy of particles entering a calorimeter is fully absorbed by the creation of a secondary shower in the whole volume of the calorimeter as shown in Fig. 3. The absorbed energy is measured by either plastic scintillators, semiconductor- or gas detectors and the initial energy of the particle can be obtained. Conventional calorimeters can be divided into sampling- and homogenous calorimeters, as well as by their application in electromagnetic and hadronic calorimeters. Due to the higher mass of hadrons compared to e.g. electrons, the hadronic shower is more extended than the electromagnetic shower of the electron, which means that the design of the calorimeter needs to be larger in size [10].

2.2 Time-of-Flight (ToF)

Instead of measuring the residual energy directly via a conventional calorimeter, this can also be done indirectly via a time-of-flight calorimeter. Mandatory requirements are precise detectors to keep the uncertainty in time measures as small as possible in order to prevent the propagation of the uncertainty into the calculation of the residual energy. With ultra fast silicon detectors (UFSD), more specific Low-Gain-Avalanche detectors (LGAD), these requirements are met. In this section, the connection between the energy of the particle and the time of flight is stated.
Due to the fact that the energy range of the particles coming from the accelerator is between 50-800MeV and therefore the velocity is correspondingly high, the relativistic energy-momentum relation needs to be used:

$$E = \sqrt{p^2c^2 + m_0^2c^2} = E_{\text{kin}} + E_{\text{pot}} \tag{2.9}$$

with

$$E_{\text{pot}} = m_0c^2 \tag{2.10}$$

$$E_{\text{kin}} = m_0c^2(\gamma - 1) \tag{2.11}$$

where γ is defined as follows and can be expressed with the help of 2.10 and 2.11 as E_{kin} and E_{pot}:

$$\gamma = \frac{1}{\sqrt{1 - \frac{v^2}{c^2}}} = \frac{E_{\text{kin}}}{E_{\text{pot}}} + 1 = \frac{E_{\text{kin}} + E_{\text{pot}}}{E_{\text{pot}}} \tag{2.12}$$

For the calculation of the time-of-flight, first, the velocity of the particle needs to be calculated and eq. 2.12 is rearranged to:

$$\frac{v^2}{c^2} = 1 - \frac{E_{\text{pot}}^2}{(E_{\text{kin}} + E_{\text{pot}})^2} = \frac{E_{\text{kin}}^2 + 2E_{\text{kin}}E_{\text{pot}} + E_{\text{pot}}^2 - E_{\text{pot}}^2}{(E_{\text{kin}} + E_{\text{pot}})^2} \tag{2.13}$$

and obtain the velocity in dependence of its flight path $\vec{x}$:

$$v(\vec{x}) = c\frac{E_{\text{kin}}(\vec{x})}{E_{\text{kin}}(\vec{x}) + E_{\text{pot}}}\sqrt{1 - 2\frac{E_{\text{pot}}}{E_{\text{kin}}(\vec{x})}} \tag{2.14}$$

by using the relation that time is distance divided by velocity the time-of-flight can be stated finally as:

$$TOF = \int_0^L \frac{\mathrm{d}s}{v(\vec{x}(s))} \tag{2.15}$$

where the last step in Eq. 2.15 can be simplified when a straight line with defined distance is approached. When using a time-of-flight calorimeter to obtain the residual energy of an ion beam, this is the most common case.

2.3 Interaction of Particles with Matter

The principle of particle detection can be described by a simple gas detector: The gas inside a volume is ionized and with the help of an electrical field, the generated electron-hole-pairs drift towards the electrodes and can therefore be recognised as a signal. This signal is proportional to the energy of the irradiation and subsequently, a correlation to the incoming particle can be established. The deposited energy can be described via the *Linear Energy Transfer* (LET) and is given in terms of energy change per depth:

$$\mathrm{LET} = -\frac{\mathrm{d}E}{\mathrm{d}x} \tag{2.16}$$

This energy depends on the type of irradiation and in this work, the important types are electromagnetic radiation on the one and charged particles on the other side. Fig. 4 shows the difference of the two types when referring to the penetration of a medium.

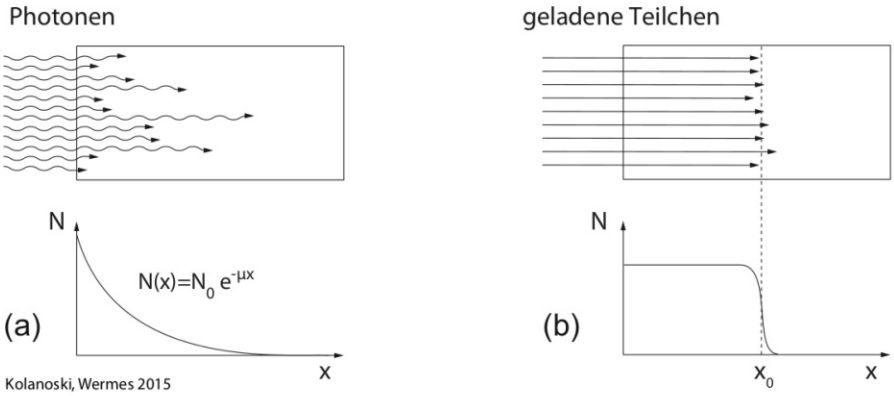

Figure 4: (a) Absorption of photons in a material follows an exponential decay of the intensity. (b) Energy loss of charged particles inside a medium leads to a limited range with a localized decrease of intensity [11].

The energy loss processes for photons are the photo effect, compton scattering and pair production of electrons and positrons (Fig. 5). The photo effect is characterized by absorption of the photon by an electron in the atomic shell, while in the compton scattering, the wavelength of the photon is shifted by deflecting on an electron, which absorbs parts of the kinetic energy of the transferred photon. At high energies ($>$ 1.022 MeV), pair production can take place in the presence of a nucleus (conservation of momentum), where an electron-positron pair is generated.
The intensity as a function of the distance as a quantity for the depth of the penetrating photon inside a material is stated by the *Beer-Lambert Law* and follows an exponential decay:

$$N(x) = N_0 \mathrm{e}^{-\mu x} \tag{2.17}$$

where N_0 is the number of particles (intensity) in the beginning, μ is the absorption coefficient of the material and x is the penetration depth.

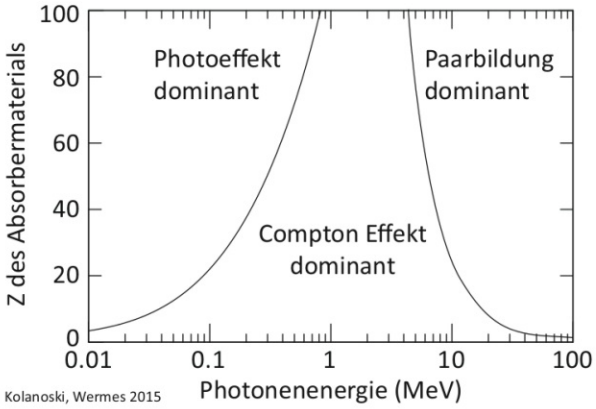

Figure 5: At low energies, the photo effect dominates, the compton scattering is present in the medium energy range and pair production occurs with high photon energies [11].

Hadrons are sub-atomic particles, such as neutrons and protons that are bound together via the strong force. Depending on the energy regime and the detector material, electromagnetic interaction (collision with atoms) and nuclear interaction can occur. Electromagnetic interaction initiates the following processes:

- **Ionization of atoms**: An atom that acquires an electrical charge by losing or gaining electrons is called an ion. By losing electrons, the ion becomes positively and by gaining electrons negatively charged.
- **Excitation of atoms**: The electrons or the nucleus of an atom occupies a higher energy level by absorption of a descrete amount of energy.
- **Bremsstrahlung**: By deflecting of a charged particle due to the field of another charged particle (e.g. electron by an atomic nucleus), electromagnetic radiation is emitted.
- **Cherenkov radiation**: Electromagnetic radiation is emitted when a charged particle passes through matter and exceeds the material's velocity of light.
- **Transition radiation**: Another form of electromagnetic radiation that is emitted when a charged particle passes a boundary of materials with different dielectric constants.

Hadronic showers inside a calorimeter are a series of inelastic hadronic interactions of a primary particle with the nuclei of the target material, releasing more particles that undergo further inelastic interactions. These interactions of high energy hadrons can be:

- **Production of mesons (π, K, ...) and baryons (n,p ...)**: Components of the nucleus receive enough energy to interact with each other (intra-nuclear) or escape the nucleus and hit another nucleus (inter-nuclear). Secondary particles, such as mesons and baryons are created in each process.
- **Spallation**: Transformation of a nucleus caused by a hadronically interacting particle where a large number of elementary particles, α-particles and larger debris of the nucleus are emitted.

- **Excitation of nuclei**: Caused by spallation, where the nuclei are in an excited state and releases further particles or undergoes fission.
- **Nuclear evaporation**: Excited nuclei emit particles until the remaining energy is below the binding energy of the components in the nucleus.
- **Nuclear fission**: In heavy elements, fission may occur, following spallation or due to the capturing of slow neutrons. The nucleus decays in two or three approximately equal debris. Additionally, photons and neutrons are emitted and if enough excitation energy remains, further hadrons are emitted.

The *Bethe-Bloch Formula* describes the average energy loss of a charged particle in a medium as a function of the particle energy and is called stopping power:

$$-\frac{\mathrm{d}E}{\mathrm{d}x} = 4\pi N_\mathrm{A} r_\mathrm{e}^2 m_\mathrm{e} c^2 z^2 \frac{Z}{A}\frac{1}{\beta^2}\left[\frac{1}{2}\ln\left(\frac{2m_\mathrm{e}c^2\beta^2\gamma^2 T_\mathrm{max}}{I^2}\right) - \beta^2 - \frac{\delta(\gamma)}{2}\right] \tag{2.18}$$

where N_A is the Avogadro Number, r_e and m_e the classical electron radius and the rest mass of the electron, c the vacuum light speed, z the charge of the incident particle, Z and A the atomic number and the atomic mass, $\beta = v/c$ and $\gamma = \frac{1}{1-\beta^2}$, I is the mean excitation energy, T_max the maximum kinetic energy which can be imparted to a free electron in a single collision, δ is the density effect correction.
In Fig. 6, the Bethe-Bloch curve, here as an example muon on copper, is shown, where the stopping power as a function of the momentum can be seen. In Fig. 7, the dependency of the stopping power on the kinetic energy of protons on silicon is drawn and it can be seen, that the shape of the curve is very similar to Fig. 6, because myons and protons are hadrons and interact with matter in the same way.
In Fig. 7, the maximum of the stopping power at $7 \cdot 10^{-2}$ MeV and the minimum stopping power at $1 \cdot 10^3$ MeV, referring to the MIP (minimum ionizing particle), can be seen. The total stopping power contains the nuclear- and the electronic stopping power.
The interaction of charged particles with matter is a statistical process forming a *Landau distribution* in thin absorbers. The *Landau − distribution* is characterized by a strong increase and a smooth tail (see chapter 3.6 for visualization). This is due to the higher possibility of small energy transfers. The significant tail is formed by rare interactions with small impact parameters generating electrons in the keV-regime (δ - electrons). Due to the asymmetric shape of the *Landau distribution*, the statistical mean value and the most probable value (MPV) differ from each other, while the mean value is the basis of obtaining the mean energy loss inside matter. The tail in the *Landau distribution* approaches a *Gauss distribution* for thick absorbers.

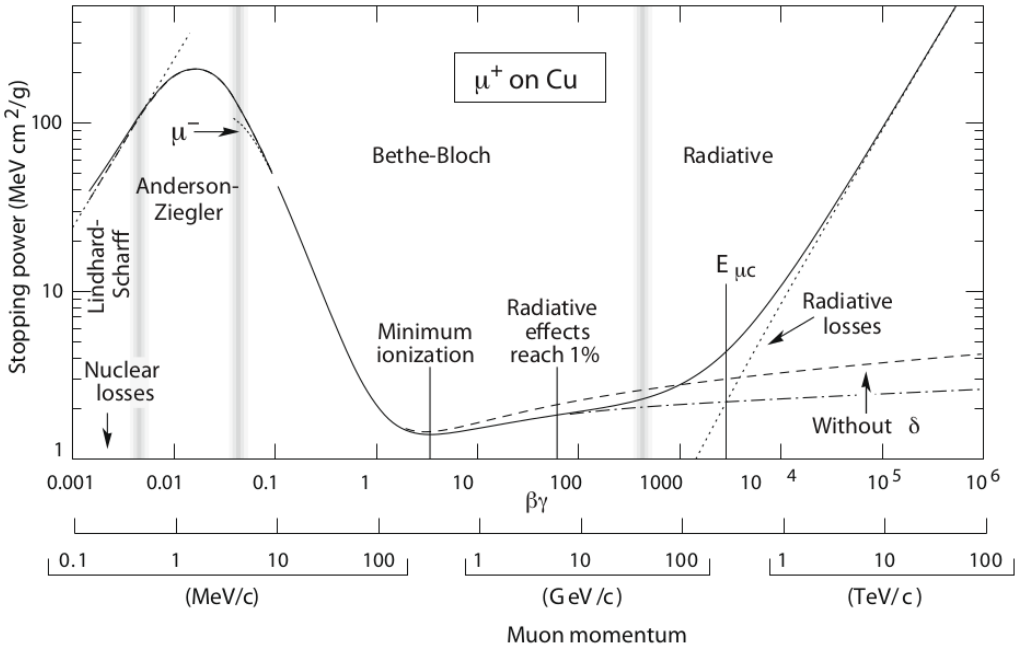

Figure 6: Energy loss for positive muons on copper. The vertical lines designate the borders for the different theoretical descriptions, where in the middle, the Bethe-Bloch-Area can be seen. From the left Bethe-Bloch border to the "Minimum ionization"-marker, the curve is defined by a decreasing of the stopping power. With an increasing of the energy from the "Minimum ionization"-marker to the right, the stopping power experiences a smooth rise [11].

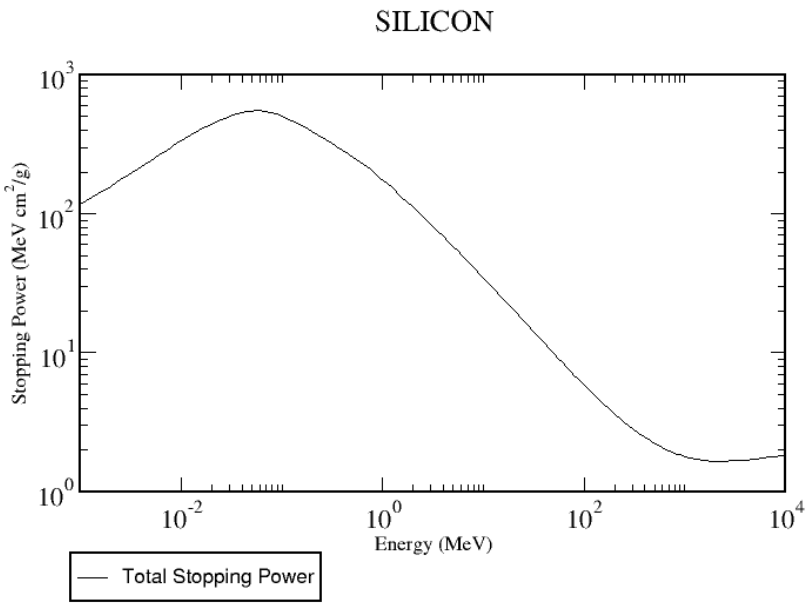

Figure 7: Stopping power of protons in silicon as a function of the energy. The maximum energy and the MIP-energy can be seen [6].

From the entry point of a charged particle beam into matter the energy loss slowly increases, with deeper penetration into the material the particle loses more energy and this leads to the formation of a peak in the energy loss vs. depth curve. This formation of the so-called *Bragg Peak* is the direct result of the *Bethe-Bloch Curve*. As can be seen in Fig. 8, the *Bragg Peak* dominates the energy loss in a specific depth of the material. For cancer treatment, the *Bragg Peak* is of high interest, because the energy deposition can be controlled via the initial kinetic energy of the particles and tumorous cells can therefore be destroyed [11] [12] [13].

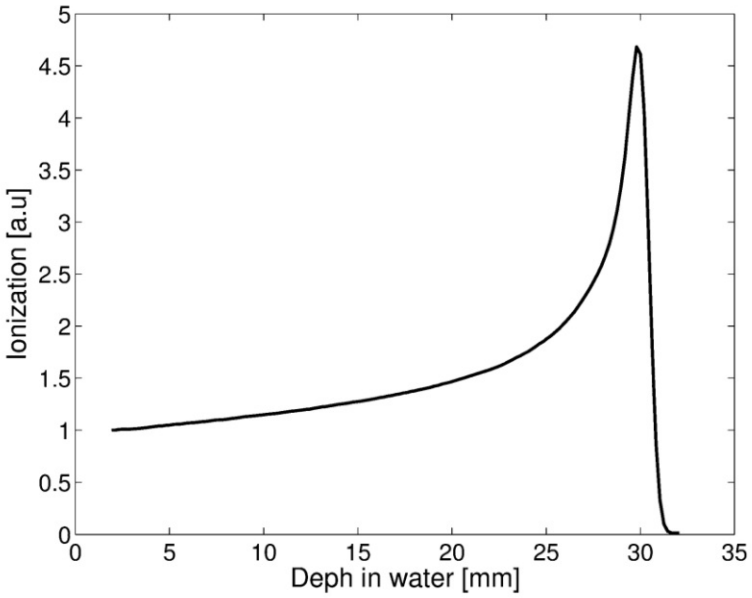

Figure 8: Bragg peak of a 62 MeV proton beam acquired in a water-tank [14].

2.4 Semiconductor Detectors

The most common semiconducting materials are silicon and germanium. The valence- and the conduction band of semiconductors are separated by a band gap, which can be surmounted by the electrons by thermal or other excitations, creating an electron-hole pair. This leads to a conduction of electrical current, referring to an intrinsic semiconductor. For a better usage, most semiconductors are doped with elements from nearby chemical groups, often referred to as an extrinsic semiconductor. For example silicon is an element belonging to the 4th main group in the periodic system. When doped with aluminium from the 3rd main group, which is an electron acceptor, an electron deficit is created referring to a p-type semiconductor as can be seen in Fig. 9a. On the other side, silicon can also be doped with an element from the 5th main group like phosphorous and an electron abundance appears. This results in an n-type semiconductor as shown in Fig. 9b. A thermal equilibrium is established inside the doped semiconductor, whether it indicates an electron surplus or an electron deficit [11].

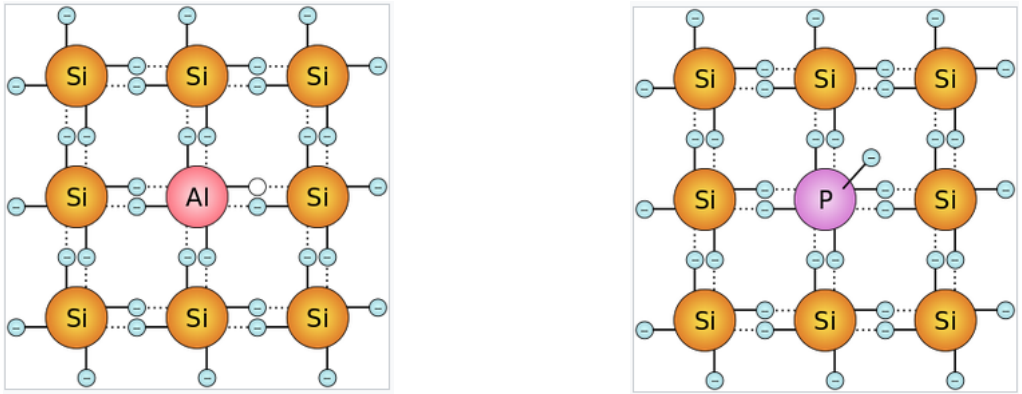

Figure 9: a) p-doped silicon: a Si-atom is replaced by an Al-atom from the 3rd main group. b) n-doped silicon: replacing by a P-atom from the 5th main group.

When n- and p-type semiconductors are in contact, they form a so-called pn-junction, an area, where differently charged regions meet. In order to balance the potential difference in this region, the majority charge carriers diffuse into the contrarily charged area resulting in a current (I) and subsequently, an electric field (E) that forces the electrons and holes to move until they reach an equilibrium. A depletion zone is created between the undepleted p- and n-regions, where there are no free charge carriers but an electric field due to an electric potential (V_D) [13].
The electric field in the depletion region will sweep mobile carriers to the electrodes (p- and n-region), so the diode forms an ionization chamber. By applying a reverse bias voltage $|U|$, the thin depletion region (in orders of µm can be extended and the sensitive volume of the detector can be increased. The depletion width increases with the square root of the reverse bias voltage, but the maximum voltage one can apply is limited, because at fields $> 10^5$ V/cm electrons acquire sufficient energy to form secondary electron–hole pairs, ultimately leading to an uncontrolled charge multiplication, called "breakdown" [15].

Fig. 10 shows the impact of the bias voltage $|U|$ on the pn-junction, where the change of the electrical field can be expressed as $-e(V_D - |U|)$ in forward bias- or $-e(V_D + |U|)$ in reversed bias mode [16]. The elementary charge e is a fundamental constant with the following value:

$$e = 1.602 \cdot 10^{-19}\text{coulomb}$$

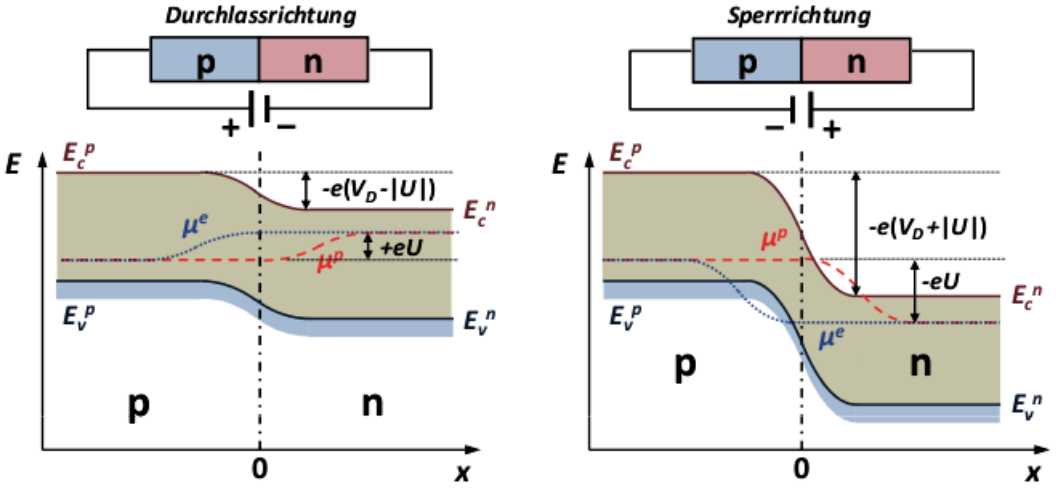

Figure 10: pn-junction in forward (left) and reverse direction (right). A detector is used as a diode with reversed bias voltage (right). The conduction band- and the valence band edge is shown (black continuous line) as well as the electrochemical quasi-potential of the electrons (blue dotted line) and the holes (red dashed line). In reversed bias mode, the voltage (U) is positive on the n-side, therefore the potential energy of the electrons ($(-e)(U)$) is negative [16].

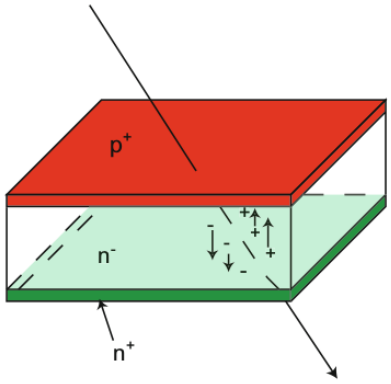

Figure 11: Scheme of a pn-semiconductor detector, where an incident particle creates electron-hole pairs drifting to opposite directions, due to the electrical field inside the sensor [17].

In Fig. 11, a simple design of a semiconductor detector is shown, where a highly doped p-layer (p^+) is divided from a highly doped n-layer (n^+) with a low doped n-layer (n^-) in between. When radiation hits this device, energy is deposited in the low doped layer along its path and electron-hole pairs are created, which drift to the higher doped areas where they can be recognised as a signal. This signals specifications depend mostly on the thickness of the sensor, the velocity of the charge carriers and the electric field. The *Drude model* gives the drift velocity v_D by known charge carrier mobility μ and the electrical field E as follows:

$$v_D = \mu \cdot E \tag{2.19}$$

Ramo's Theorem states that the induced current $i(t)$ in the electrodes is proportional to the forced movement $v(t)$ of the charges q by the electric field E:

$$i(t) = E \cdot q \cdot v(t) \tag{2.20}$$

Essentially, *Ramo's Theorem* states that there is a signal (current) whether or not the charges reach the electrodes [12] [13].

2.5 Low Gain Avalanche Detector (LGAD)

The signal formation process in traditional silicon detectors limits the ability to measure the arrival time of the incoming particle to values of 200 ps. This refers to a local resolution of 5 cm when assuming particles at the speed of light [18]. For time-of-flight experiments, a better resolution is needed. LGADs have a better time resolution than the classic semiconductor detectors using charge multiplication. This effect occurs in large electrical fields, where single charge carriers created by passing of a particle through matter generate even more charge carriers that help to increase the outcoming signal (more detailed in section 2.6). While in avalanche photon detectors, the gain is 100 and more, LGADs only show a gain of 10 - 20 [19] [20]. The low gain is the result of the underlying need for fast detectors with the lowest gain possible to sufficiently perform accurate single particle time measurements. A gain of 10 - 20 is referred to as the multiplication region, where the signal is proportional to dE/dx and further, a gain of ~ 10 is optimal for S/N, due to the negligible influence of shot noise. The avalanche mode is defined as being in the gain-region of $10^5 - 10^6$, where the signal is not proportional to dE/dx anymore and it cannot be distinguished between noise or thermal excitation from a minimal ionizing particle (MIP). LGADs are additionally designed with a small thickness to provide a faster rising edge ("slew rate"). But the thickness also has to be in balance, due to the high capacitance of very thin detectors. The results of experiments and simulations using these boundary conditions show an optimum performance with a thickness of $\sim 50\,\mu m$ and a gain of ~ 20 [18]. A schematic view of the design of the LGAD is shown in Fig. 12.

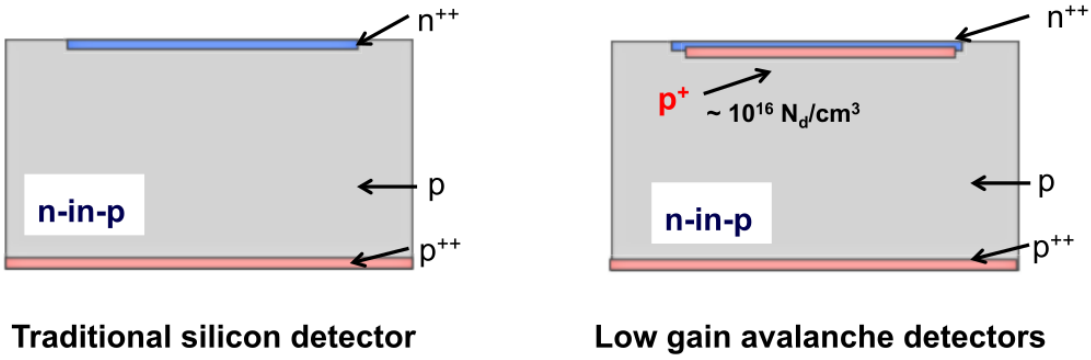

Figure 12: Scheme of a traditional silicon diode (left) and of a Low-Gain Avalanche Diode (right) [17].

n-in-p means that the multiplication process is initiated by the electrons drifting towards the n^{++} electrode. With the additional doping layer placed close to the junction, the doping concentration is increased and therefore the electric field in this region causing the multiplication of charge carriers (Fig. 13).
The big difference between the internal gain mechanism of an LGAD and an external amplifier lies in the signal to noise ratio (SNR). Though the signal noise is increased due to the internal gain in an LGAD, the dominating noise source is typically electronic noise. While the amplification of an external amplifier works on the signal and the noise without a net improvement, the internal gain of the LGAD increases the total SNR. This is only possible at low amplifications, otherwise the noise would be too high to separate it from the real signal [17] [18] [21].

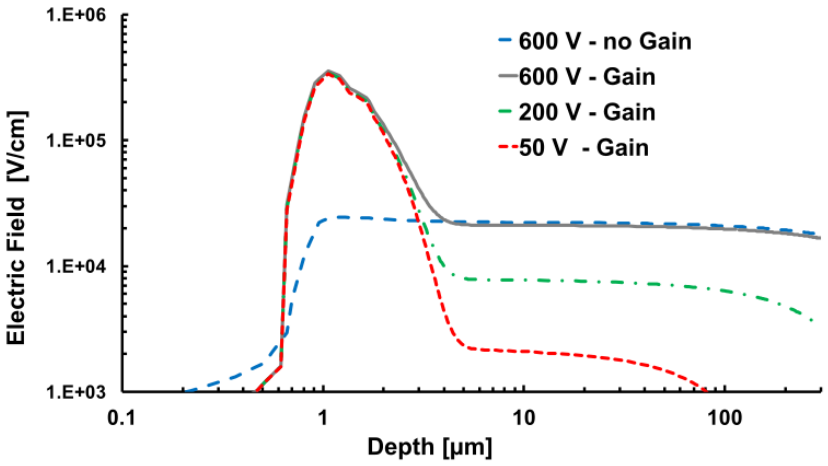

Figure 13: The electric field of a 300 µm thick LGAD at different bias voltages compared to a PiN (no gain) Si sensor in logarithmic scale [18].

For a time-of-flight experiment, the time resolution is the crucial quantity and for LGADs it can be expressed as follows:

$$\sigma_t^2 \approx \left(\frac{a_{\text{jitter}}}{S/N}\right)^2 + c_{\text{floor}}^2 \tag{2.21}$$

where the jitter term is dominated by the rise time of the signal t_{rise} and the constant term mainly depends on the Landau noise, synchronisation between channels and TDC [22] [23] [24] [25] [26]. This will be explained further in Sec. 2.6.

2.6 Signal Processing

2.6.1 Theoretical Background

The creation of a signal inside a semiconductor detector was explained in chapter 2.4. According to *Ramo's Theorem* (eq. 2.20), the theoretical shape of a signal has its peak at the very beginning, because the most free charge carriers contribute to the current and decrease with an exponential-like decay as shown in Fig. 14.
In the readout circuit, the bandwidth is mainly determined by the transmission lines and the input/output resistance and capacitance of the involved devices. This limitation in bandwidth causes a reshaping of the theoretical signal as can be seen in Fig. 15.

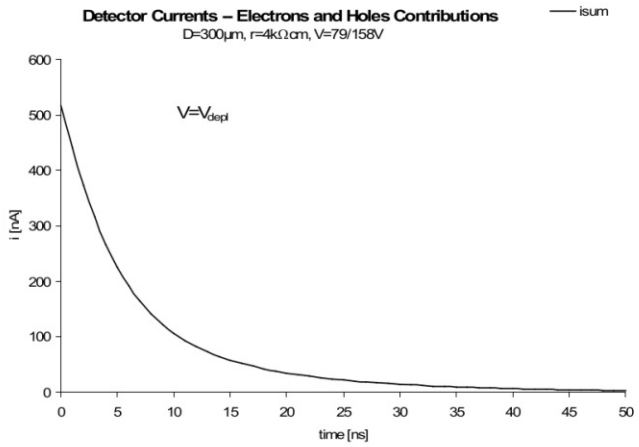

Figure 14: Theoretical signal that is produced by a single particle inside a semiconductor detector. All of the created electrons and holes contribute to the current signal with a maximum at 0 ns and an exponential-like decay. [10].

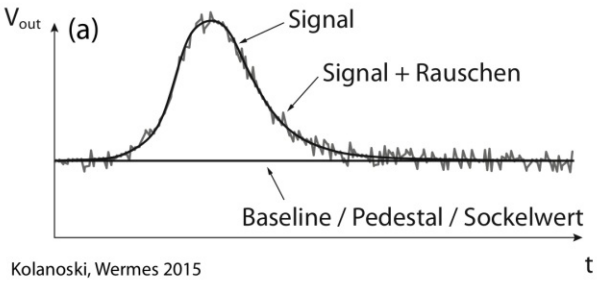

Figure 15: The processible signal of a semiconductor detector consists of a baseline, noise and the signal itself. Due to the limited bandwidth inside a circuit, the real signal shape is characterised by a positive gradient, a maximum and a decreasing distal part [11].

The offset (baseline) is the output signal in the absence of an input signal from the detector, while the noise is mainly induced due to electronic noise that is generated by the random thermal motion of charge carriers in an electrical conductor [11]. The pulse of a detector system is a combination of the detector signal, the offset and the noise as shown in Fig. 15. There are also other types of noise, such as low-frequency noise, shot noise, flicker-, burst- and transit-time noise and are expressed as N [15]. In the following section, the noise and uncertainties will be addressed in detail.

2.6.2 Uncertainties in time resolution

However, if time should be measured, the time precision is influenced by the following uncertainties that occur either in the detector or the readout circuit itself [18]:

- Landau Noise

  Caused by non-uniform charge deposition in the active volume of the sensor

- Time Walk

  Larger signals cross a given threshold V_{th} earlier than smaller ones introducing a time delay t_d

$$\sigma_{\text{Time Walk}} = [t_{\text{d}}]_{\text{RMS}} = \left[\frac{V_{\text{th}}}{S/t_{\text{rise}}}\right]_{\text{RMS}} \propto \left[\frac{N}{\text{d}V/\text{d}t}\right]_{\text{RMS}} \tag{2.22}$$

- Distortion

  Due to varying charge carrier drift velocity and non-uniform weighting fields signal distortion contributes a part to the total uncertainty

- TDC (time-to-digital converter)

  The digitization of the timing information is done by placing it into a time bin of width ΔT given by the TDC least significant bit and adding a timing uncertainty:

$$\sigma_{\text{TDC}} = \Delta T/\sqrt{12} \tag{2.23}$$

- Jitter

  Due to the presence of noise on the signal or the electronics, the comparator fires too early or too late. This type of uncertainty is directly proportional due to the noise N as the following equation shows:

$$\sigma_{\text{Jitter}} = \frac{N}{\text{d}V/\text{d}t} \approx t_{\text{rise}}/\left(\frac{S}{N}\right) \tag{2.24}$$

Time resolution can be expressed as the sum of the above terms:

$$\sigma_{\text{t}}^2 = \sigma_{\text{Landau Noise}}^2 + \sigma_{\text{Time Walk}}^2 + \sigma_{\text{Distortion}}^2 + \sigma_{\text{TDC}}^2 + \sigma_{\text{Jitter}}^2 \tag{2.25}$$

2.6.3 Time stamps and time resolution

For a time-of-flight setup, it is necessary to define a reference point in a signal curve that is used in consecutive pulses to measure the time between them. The experiments show that the best choice is a linear fit to the leading edge of the pulse where a time stamp is extracted at 30% of pulse amplitude. This is shown in Fig. 16. The Figure shows the two signals coming from two different channels of the oscilloscope, referred to as LGAD 1 and LGAD 2 that were produced by a single proton, which hits both detectors. The procedure of introducing time stamps to each signal makes it possible to obtain the time-of-flight of a particle. When recording thousands or more particles and their time-of-flight from one spill of the MedAustron accelerator, a statistical distribution with the mean value and its standard deviation can be obtained and the time resolution of the LGADs can be extracted.

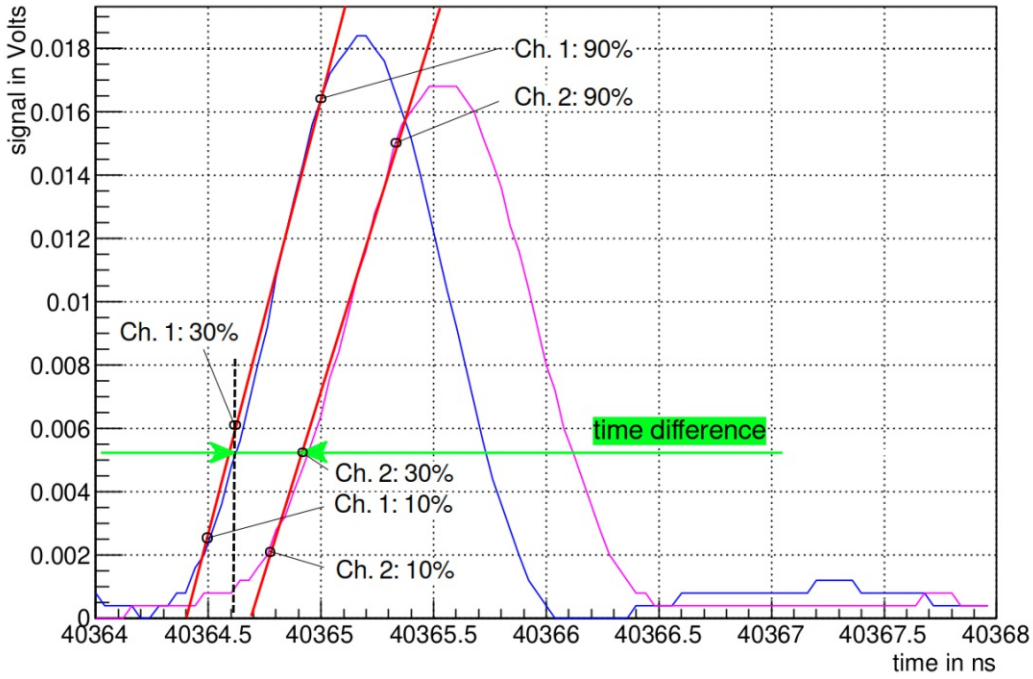

Figure 16: The signals of channel 1 (blue) and channel 2 (magenta) as recorded by the oscilloscope during the MedAustron experiment. For determining the time difference between the signals, a time stamp is extracted at 30% of pulse amplitude with the help of a leading edge linear fit (red lines). The linear fit is based on the points at 10% and 90% of pulse amplitude.

From all the signals produced by the particles of one spill, first, the time-of-flight $(t_1 - t_2)$ is calculated where t_1 refers to the time stamp at LGAD 1 and t_2 to LGAD 2. This leads to a Gaussian distribution with mean $\mu(t_1 - t_2)$ and the standard deviation $\sigma(t_1 - t_2)$. In order to obtain the time resolution for one LGAD, the standard deviation has to be divided by $\sqrt{2}$.

$$\sigma_{\mathrm{LGAD}} = \frac{1}{\sqrt{2}}\,\sigma(t_1 - t_2) \tag{2.26}$$

3 Experimental and Computational Methods

3.1 MedAustron ion therapy and research center

Located in Wiener Neustadt, the MedAustron is a modern medical and research facility that is able to deliver proton beams with kinetic energies up to 250MeV and carbon ion beams up to 400MeV/nucleon for clinical applications, by the help of a particle accelerator. For research applications the accelerator can provide with proton energies even up to 800MeV. Fig. 17 provides an overview of the accelerator complex.

Figure 17: Layout of the MedAustron facility, where the ion sources, the linear accelerator and the synchrotron can be seen. Via magnets, the ion beam is guided to the irradiation rooms that are divided into clinical and non-clinical research [27].

At the beginning of the injection chain, either H^{3+} ions or $^{12}C^{4+}$ ions are generated in an ECR (Electron Cyclotron Resonance) ion source and extracted at a kinetic energy of 8 keV/u. Subsequently, the energy of the particles is gradually increased starting in the RFQ (Radio Frequency Quadrupole) and followed by an IH linac (Interdigital H-Mode linear accelerator) that boosts the energy up to 7 MeV/u. At the end of the low-energy beam transport line (LEBT), a stripping foil removes the remaining electrons from the ions. Either protons, stemming from fragmentation of the H^{3+} ions, or fully ionized carbon $^{12}C^{6+}$ ions are then transferred to the synchrotron by the Medium Energy Beam Transfer line (MEBT).
The synchrotron is a circular vacuum tube with a circumference of 77.6m consisting of 16 2-metre-long dipoles, 24 quadrupoles, 4 sextupoles and one resonance sextupole. All these magnets are used to accelerate and stabilize the ions to keep them on the circular track until they reach the desired kinetic energy. The extraction from the synchrotron is done via the high-energy beam transport line (HEBT), which connects the synchrotoron with the irradiation rooms and contains the beam qualification diagnostics for quality assurance.

During the shifts at MedAustron, a close communication with the operators is crucial to get the right beam settings. Treatment plans have to be created before the shifts as a custom schedule of settings that are being executed during the experiments. These treatment plans are created via the MedAustron PlugIn (MAPI) that interfaces the medical software frontend of the MedAustron particle therapy accelerator (MAPTA) and is able to provide for settings listed below [27] [28] [29] [30].

Protons (p):

- Nominal rate: 2×10^{10} p/spill
- degrader: 10, 20, 50, 100
- available energies: 62.4 - 252.7 MeV
- Spotsize for 62.4 MeV $\approx$ 2.1 cm
- Spotsize for 252.7 MeV $\approx$ 0.7 cm
- additional 800 MeV with the same degrader settings and spotsizes: 0.45, 0.8, 2 cm

carbon ions ($^{12}C^{6+}$):

- Nominal rate: 2×10^{8} p/spill
- degrader: 10, 20, 50, 100
- available energies: 120 - 402.8 MeV/nucleon

3.2 Overview of the used type of setups

The basic components for a time-of-flight experiment are as follows: A particle source, two detectors defining the distance the particles have to travel and a signal processing device. In this work, two different experimental setups were used. On the one hand, the laser setup at the HEPHY institute in Vienna for characterizing and studying the behaviour of the LGADs and on the other hand, the ion beam setup at MedAustron in Wiener Neustadt for testing the whole installation via proton and carbon beams. At the HEPHY setup, only one LGAD board could be characterised at once because the photons of the laser beam are not able to penetrate the detector like particles would do at the beam setup at MedAustron.
Apart from the experimental access to the time-of-flight topic, also a simulation part was done in this work. With the help of the Geant4 simulation framework, the beam setup was designed and delivered information for comparison with the "real" experiment and also gave the opportunity to go further: examining an optimised time-of-flight setup.

3.3 Ion beam setup at MedAustron

While in Sec. 3.1, the MedAustron facility in general was introduced, here the time-of-flight setup with LGADs, assembled in the IR1, is explained. Referring to Fig. 18, the setup consisted of 2 LGAD boards (*LGAD1* and *LGAD2*) with a distance of 2.5 cm between each other and contained the silicon detector itself, the on-board amplifier and connections like the high-voltage and low-voltage input, a calibration input and the signal output. The distance of 2.5 cm was chosen, because the active LGAD diodes have an area of only $1mm^2$ and when using a spot size of the ion beam of e.g. 8x8mm and the beam widening with a greater distance appears, the possibility of even hitting the diode is decreasing rapidly. The low-voltage power supply ($LV - Power\ Supply$ (3.3.4)) provided the first-stage amplifier on the LGAD boards with 2.25 V, while the high-voltage power supply ($HV - Power\ Supply$ (3.3.3)) was connected to the boards, providing a bias-potential between 0 V and 400 V to the silicon sensors. The oscilloscope (3.3.1) was responsible for acquiring the data by sampling the output signal with 25 GS/s and saving it to the bult-in hard disc. The data of the oscilloscope was accessed remotedly via the wireless network, because it was not allowed for any person to stay inside the irradiation room (IR1) during the experiments.

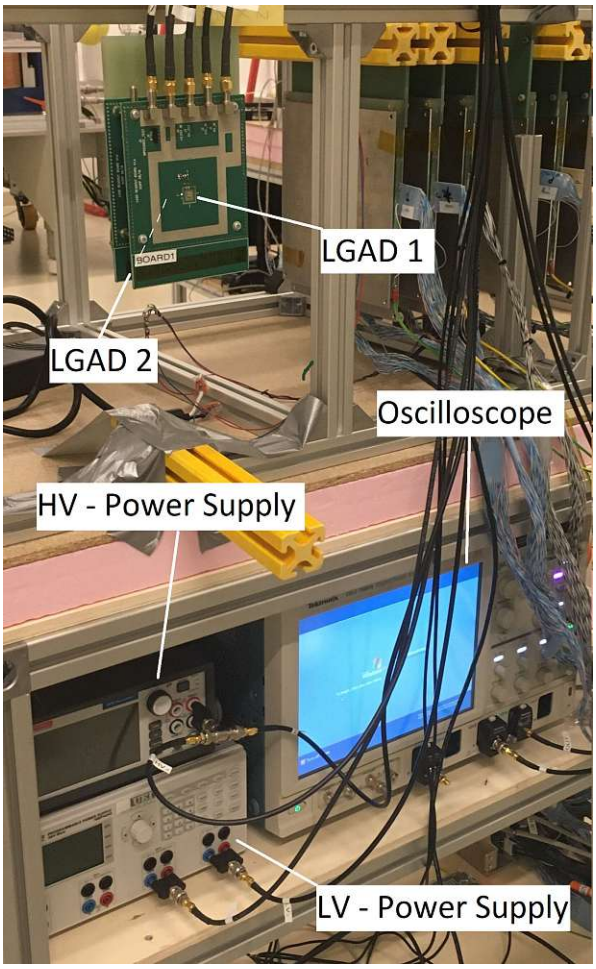

Figure 18: Overview of the LGAD setup for the test beams at MedAustron. The 2 LGAD boards were situated directly behind each other with a horizontal space of 2.5 cm. They were connected to a low-voltage- and a high-voltage power supply as input and the output of the LGADs were transferred to an oscilloscope.

The setup in Fig. 18 included two external amplifiers (Cividec amplifier Sec. 3.4.3) in the first experiments done at MedAustron. These amplifiers were situated between the LGAD outputs and the oscilloscope inputs, but it turned out that these devices were not necessary (Sec. 4.3).

3.3.1 The Oscilloscope

One of the most important devices for the collection of data is the *Tektronix DSA 70804* oscilloscope with 25 GS/s and a bandwidth of up to 8 GHz. Due to the measurement of the high frequency pulses of the ion beam and the 40 MHz pulses of the laser, this is needed to get a high resolution and a good signal shape of the signal from the detector. A high definition analysis of the signal is essential and this can be achieved when it is measured with a high bandwidth and a high sampling rate. The oscilloscope has two internal options for the 8 GHz setting: The default one (8 GHz (DSP - digital signal processing)), where the digital filters option is enabled or the 8 GHz (HW) option. By the latter setting, the HW stands for Hardware (-analog bandwidth) and does not include the digital filters, but with built-in analogue ones.

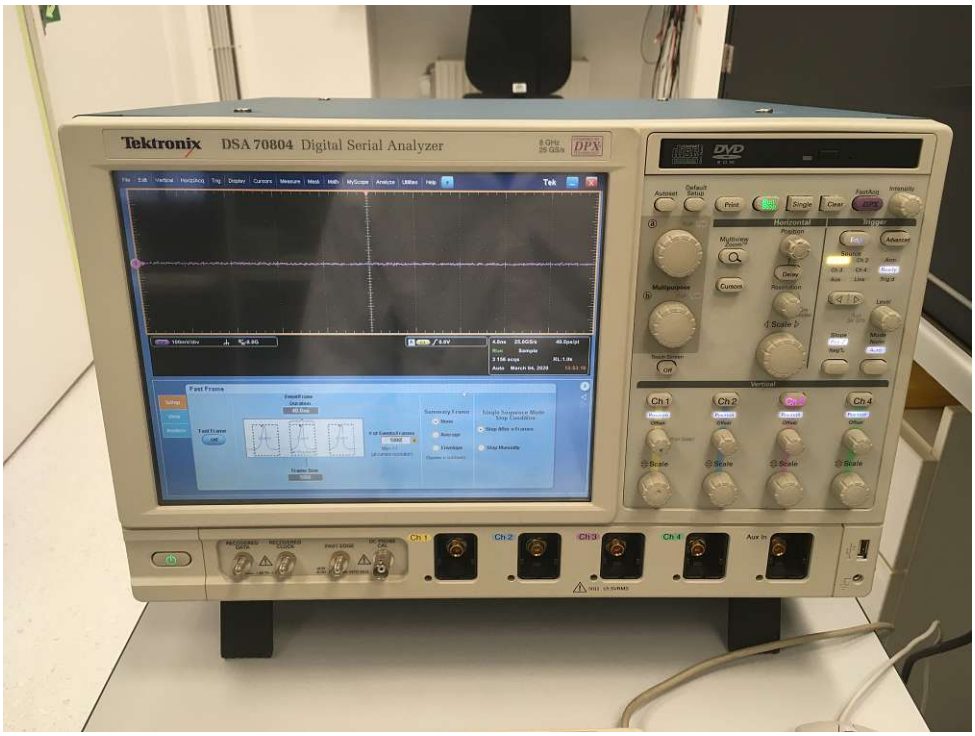

Figure 19: The *Tektronix DSA 70804* oscilloscope runs Windows XP and works with the TekScope software. From choosing the input channel to the trigger menu, all the options can either be set by the buttons on the hardware side or with the equivalent software functions.

The oscilloscope runs Windows XP and works with the TekScope software. From the choice of the input channel to the settings in the trigger menu, all the options can either be set by the buttons on the device itself or with the equivalent software functions (Fig. 19). The maximum duration of the oscilloscope when choosing the highest possible real-time resolution of 40 ps (25 GS/s) is internally limited to 400 µs with standard memory (see appendix 7.1). For some applications, the maximum duration is too short and requires a higher recording time. The *FastFrame* mode of the oscilloscope allows to capture many trigger events as single records in a larger record and then view and measure each record individually. To save the records in a file, the individual records are merged by the oscilloscope, giving the opportunity to extend the recording time.

3.3.2 LGAD

The LGAD samples and the readout board design were provided by Nicolo Cartiglia (Istituto Nazionale di Fisica Nucleare - Sezione di Torino) and Hartmut Sadrozinski (Santa Cruz Institute for Particle Physics (SCIPP)). The single diode LGADs were manufactored by Fondazione Bruno Kessler (FBK) and were part of the UFSD2 production series [19]. The LGAD boards are built up by 50 µm Si, 105 µm Cu and 1.5mm FR4. The active area of the diode is just 1 mm^2 (Fig. 20), so a precise alignment to the laser beam is important to make sure the beam is hitting the sensor.

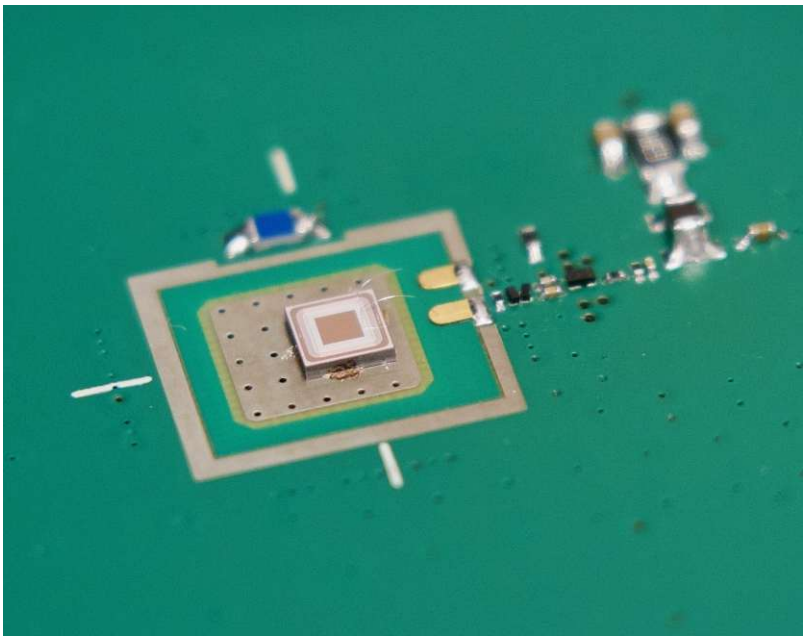

Figure 20: A close-up look on the LGAD diode, where the bias voltage is applied onto the bias pads via wire bonded lines. The first stage amplifier is also visible beside the diode.

The first stage amplifier, type BFR840 SiGe developed by Infineon, which is situated on the LGAD board is connected to the LGAD diode with the help of wire bonding as can be seen on the upper right corner of Fig. 20 [22]. Fig. 21 shows the 6 connections on the LGAD board, where only 3 of them are actually needed for the laser tests. The J1 HV_IN connection is fed by the SMU 1 HV (Fig. 22) and a coax cable to get the reverse bias voltage onto the detector. The output signal of the sensor can be taken by the connection named J3 CH_OUT and is preamplified by the on-board first stage amplifier, which is fed by the low voltage SMU (Fig. 22) via the J4 +2.25V IN connection. Further information on the electrical layout of the LGAD board is provided in Sec. 7.3.

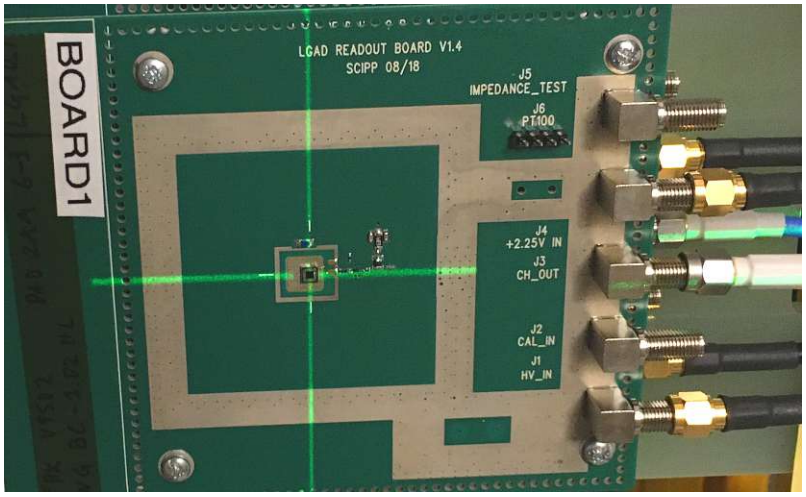

Figure 21: Picture of the whole LGAD board with the sensor in the center, the first stage amplifier on its right hand side and the 5 connections on the right hand side of the picture (from top to bottom): IMPEDANCE_TEST, +2.25V IN, CH_OUT, CAL_IN, HV_IN. Besides the IMPEDANCE_TEST connection, there is the 4 position rectangular connection for a PT100 temperature sensor.

3.3.3 The HV Power Supply

For the bias voltage, the *Keithley 2470 SourceMeter* Source Measurement Unit is responsible and provides the detector with up to 390 V. The breakdown voltage of the LGADs equal 390 V, therefore, no higher bias voltages are needed. The integrated current limiter is set to 104 µA to prevent damage on the sensor above the breakdown voltage. On the backside of the SMU, a modified interlock plug had to be inserted for increasing the voltage over a value of 180 V. (Fig. 22 top)

3.3.4 The LV Power Supply

Low voltage of 2.25 V is used for the first stage amplifier on the detector board and is supplied by the *Hameg HMP4040* programmable power supply with the current limit set to 30 µA. (Fig. 22 bottom)

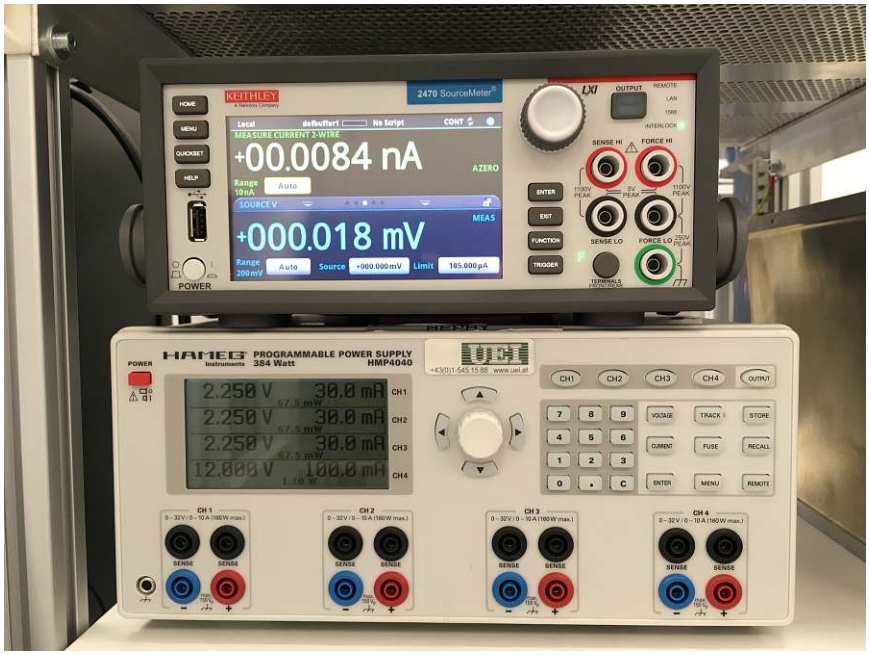

Figure 22: On top, the high voltage SMU (*Keithley 2470*) can be seen that sits on the low voltage SMU (*Hameg HMP4040*)

3.4 Laser beam setup at HEPHY

Most of the laser setup is hidden in a box to prevent its user from exposure to the photon beam. In Figure 23, the overview of the installation with its devices and connections is shown. With the software on a PC, the tune value can be adjusted, because the intensity of the beam has to be adapted to the sensitivity of the sensor. Therefore, the beam is split by a so-called beam splitter as a part of the laser hardware box, where 90% of the intensity of the beam is guided into a Photo Diode (PM100) and on the screen the laser intensity on the PM100 diode can be monitored as integrated power value. The laser driver is equipped with an integrated trigger driven by an internal clock that can also be set via the PC and provides the pulses of the beam, which hits the detector via the laser lens. Between laser head and laser lens an attenuator is installed, which can be used for damping the laser intensity. The X-Y-Plane can be adjusted to place the diode of the detector board directly below the photon beam to get a precise signal.

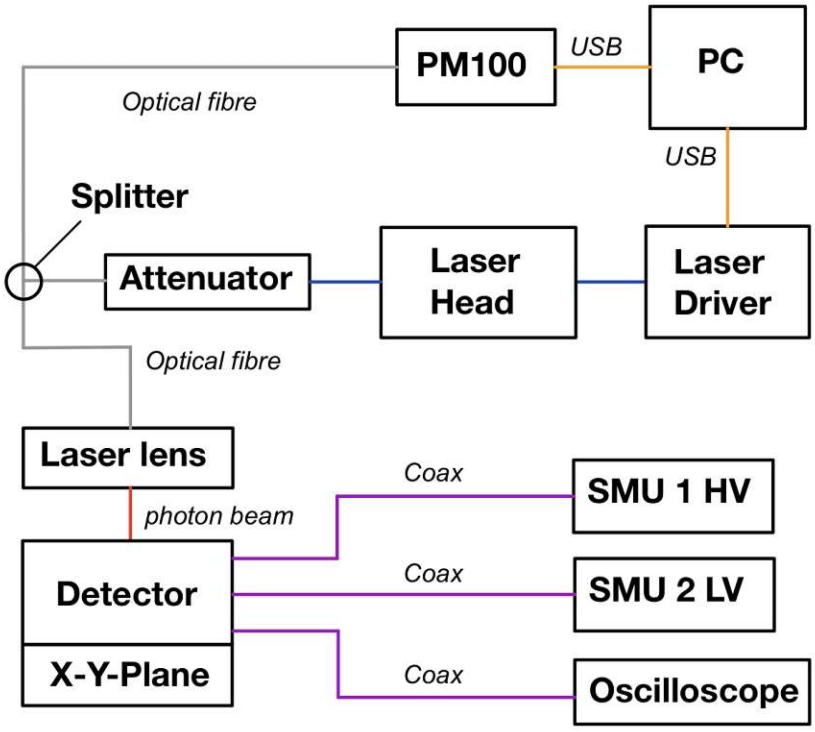

Figure 23: Basic scheme of the laser setup. The detector sits on a movable table (X-Y-plane) for the diode to be placed directly below the photon beam. The SMU 1 HV provides the sensor with the bias voltage while the SMU 2 LV is responsible for the low voltage supply. Inside the laser driver, there is an integrated trigger for the laser pulse. A beam splitter as one part of the laser hardware guides a fraction of the beam inside a Photo Diode (PM100). The oscilloscope collects the signal from the detector.

3.4.1 The Laser

The laser in the clean room at the HEPHY institute in Vienna consists of an ALS Picosecond Diode Laser (PiL106X) with a wavelength of 1054 nm, a pulse width of 40 ps and 1500 mW peak radiant power. For the test, the max. pulse repetition rate of 40 MHz is used to adapt it to the proton beam at MedAustron. In Fig. 24, the "front-end" of the laser system can be seen which consists of the optical fibre (yellow), the laser lens at the end of the fibre and the mounting device. The whole stack where the laser lens is fixed is height adjustable, while the black table with the white mounting box for the detector is movable in x- and y- direction.

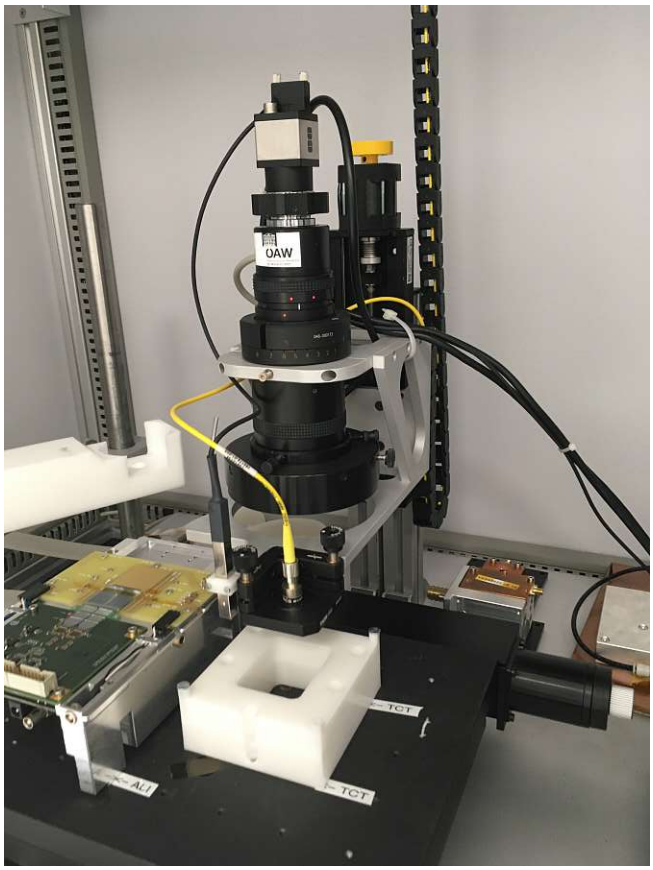

Figure 24: Photo of the "front-end" of the laser system, with the optical fibre (yellow), the laser lens and the mounting device (white).

Between laser controller and the front-end laser system there is an adjustable attenuator for the coarse setting of the tune value. It can not be seen in Figure 24 because it is situated inside a cage that was installed for better grounding to prevent pickup of external HF noise.

3.4.2 Laser hardware

The laser controller *EIG2000DX* is a hardware device that can be connected to the PC, which computes and sends the options that can be set either via the software or on the controller itself to the laser lens. Options are the frequency, the tune value (laser intensity) and the trigger menu. The key element of the laser controller is its internal clock that oscillates with up to 40 MHz and sets the trigger for the laser pulse. This internal clock can be set by the help of the control buttons on the device itself or the software and its electrical output that is represented either by NIM (Nuclear Instrumentation Standard) or TTL (Transistor-Transistor-Logic) levels acts as trigger input in the external scope. The TRIG IN TTL- and TRIG IN -5V/+5V sockets on the laser contoller (Figure 25) can be used to connect an external function generator which creates a periodic signal that can be used as a trigger for the laser and is only firing when an electrical pulse is detected. For stability reasons, the pulses of the function generator are often coupled to the freely oscillating clock of the laser controller to only set the trigger, when there is a clock signal as well for avoiding jitter uncertainties coming from the function generator. The internal clock signal can be picked up by the TRIG OUT +5V socket of the laser controller.

Figure 25: The laser controller *EIG2000DX* with the status monitor, buttons for the settings, the key-switch and the serial connenction to the PC.

3.4.3 Second stage amplifier

To increase the output signal of the LGADs, a second stage amplifier besides the amplifier on the LGAD board was used. The cividec amplifier was situated between the LGAD output and the oscilloscope input at the first MedAustron- and the laser measurements. The C2-HV broadband amplifier (Fig. 26) is a low-noise current amplifier with an analogue bandwidth of 2 GHz and 40 dB gain and is optimized for single MIP particle detection.
The electronic calibration was done at cividec and the amplification diagram is shown in Fig. 27, where the signal input is shown in red and the amplified output signal of the amplifier is shown in blue. The amplifier's input impedance is 50 Ω and the output range covers ±1 V with an effective gain of 43 dB. The linear behaviour can be seen in the range of ±8 mV, while a significant deviation begins at 6 mV [31]. The datasheet can be seen in the Appendix 7.2.

Figure 26: Front view of the cividec C2-HV Broadband amplifier that was used in the laser test for characterising it and in the first MedAustron experiment as a second stage amplifier [31].

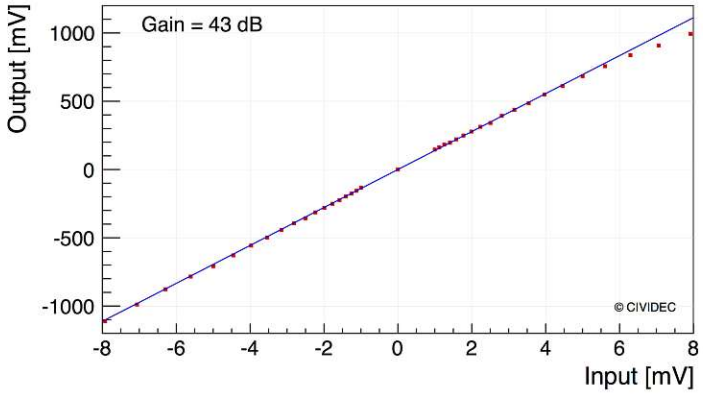

Figure 27: Calibration curve with the input signal shown in red and the amplified output signal in blue [31].

3.5 MedAustron experiments: Data collection

The LGAD signals at the MedAustron beam experiment were recorded by the oscilloscope (Sec. 3.3.1). To get enough signal peaks for statistical calculations, the oscilloscope's maximum recording time of 400 µs was chosen, referring to approximately 16 k peaks from each LGAD. The first 4 µs of the raw signal can be seen in Fig. 28, where the amplitudes of the two signals are visible. Depending on the type of interaction between the protons and the detector material, the amplitudes may vary in height as can be seen in Fig. 32. In Fig. 29, the detail of a pair of a signal is shown and the differences in the shifting of the one signal to the other are visible, referring to the different time of arrival of the proton and the time resolution of the LGADs.

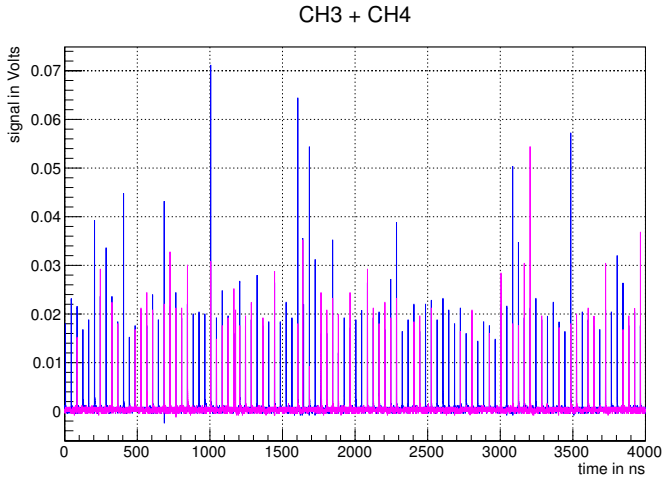

Figure 28: First 4 µs of the LGAD 1 and LGAD 2 signals recorded by the oscilloscope with 250 MeV protons at 300 V bias voltage.

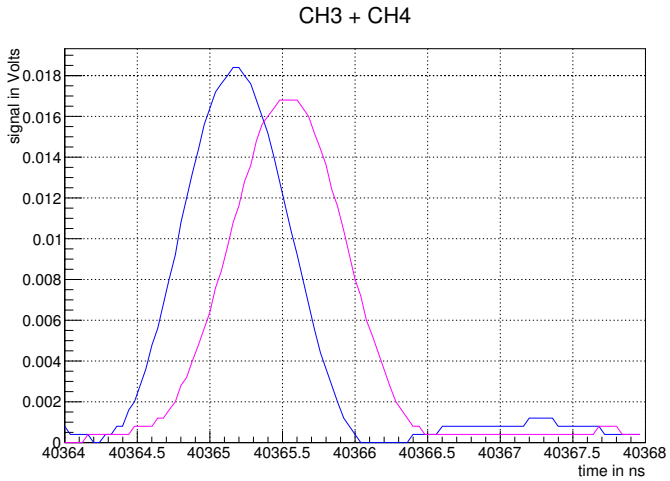

Figure 29: 4ns detail of the LGAD 1 and LGAD 2 signals recorded by the oscilloscope (CH3 + CH4) with 100 MeV protons at 360 V bias voltage.

3.6 Convert oscilloscope data into histograms

The raw data was then analyzed by a software algorithm written in C++ that recognised the signals by passing a specified threshold. The amplitude is obtained by the C++ software as the data point with the highest value of a specified data set containing the peak. Based on the peak's value of the abscissa, the right region of interest (ROI-R) and the left region of interest (ROI-L) give the borders of the area under the curve that is calculated as the sum of the signal values with respect to the offset as can be seen in Fig. 30. The offset is determined by the C++ software as a result of the noise analysis (Fig. 37) and represents the mean value of the noise amplitudes that is shifted by the from the abscissa.

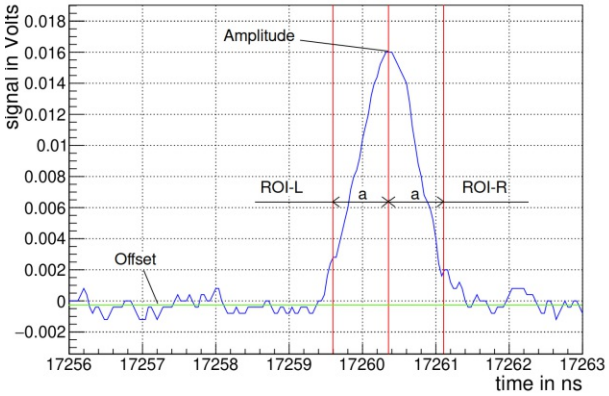

Figure 30: Example pulse with definition of the amplitude as highest signal value of the peak region. The charge is the sum of the signal values inside the left region of interest (ROI-L) and the right region of interest (ROI-R) with respect to the offset.

The rise time is evaluated by the C++ program as well, where the algorithm searches for the amplitude in the signal and determines the point at 10% and 90% of the pulse. With these points, a linear fit is made that gives the information on the offset and the slope of the straight line. When applying the linear equation on the two points, the rise time can be calculated. For a graphical explanation see Fig. 31. The distribution of the rise time is shown as an example in Fig. 36a and Fig. 36b.

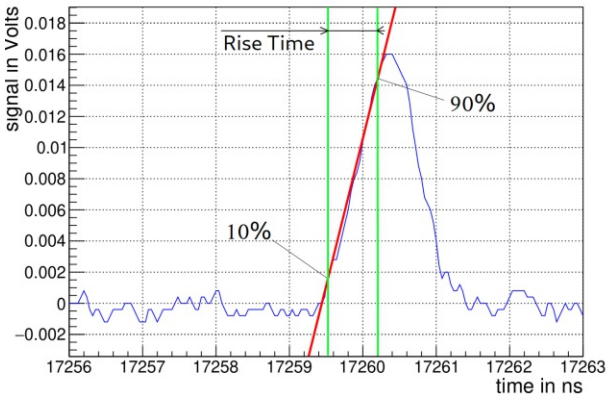

Figure 31: Example pulse with linear fit from 10% to 90% of the amplitude. The rise time is the difference of the two points on the time axis, while the information of the offset and the slope of the line has first to be evaluated.

With the help of the software tool ROOT, the amplitude, charge, rise time and time differences were put into histograms and this data was fitted with a Gauss or Landau distribution respectively. The amplitude distribution is shown in Fig. 32 with the statistical quantities presented in the "specifications" box. Besides the number of entries, also the mean value, the standard deviation, the χ^2 value and the most probable value (MPV) with the related standard deviation of the Landau fit is extracted.
The distribution of the charge of LGAD 1 (CH3) and LGAD 2 (CH4) is plotted in Fig. 33, where the Landau character can clearly be seen.

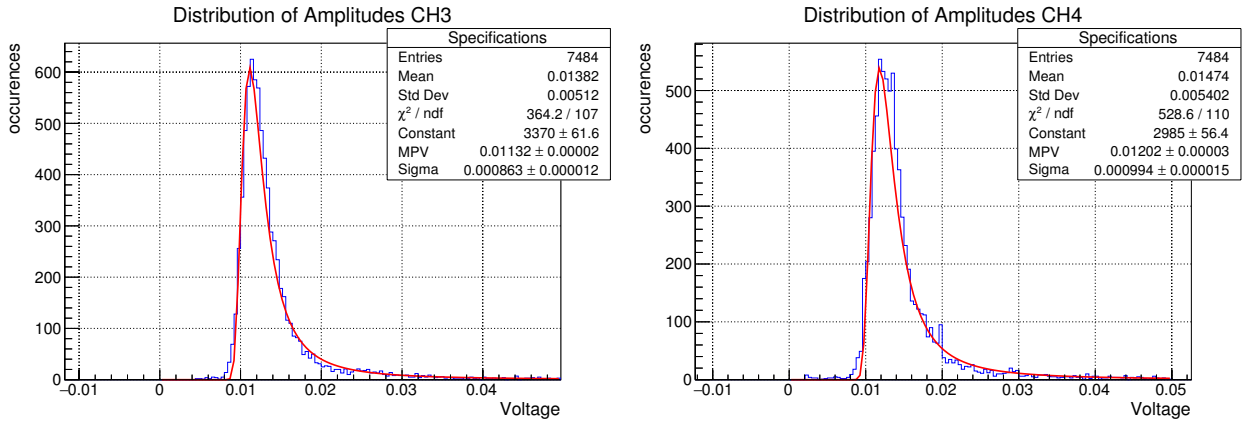

(a) **(b)**

Figure 32: Distribution and Landau fit of amplitudes at 80 MeV protons at 350 V bias voltage for the oscilloscope channel CH3 (a) and CH4 (b).

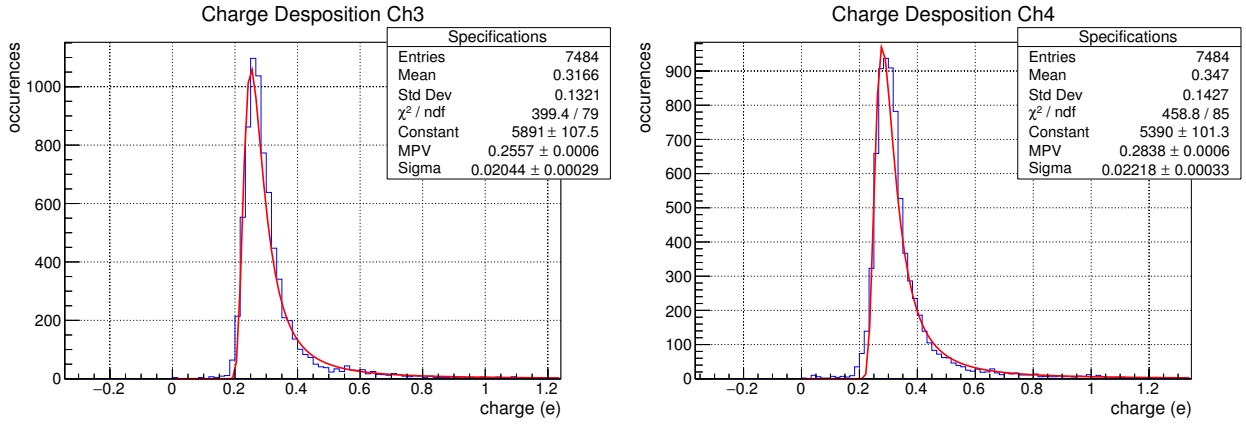

(a) **(b)**

Figure 33: Distribution and Landau fit of charge distribution at 80 MeV protons at 350 V bias voltage for the oscilloscope channel CH3 (a) and CH4 (b).

To obtain the time-of-flight and the time resolution, the histograms of the time differences are created with 3 different settings. Sec. 2.6.3 provides an explanation of the routine how the time difference is obtained from the signals at 30%. The distribution of the rising edge at 30%, 45% and 60% gave different results and when comparing Fig. 34 with Fig. 35, it is obvious that the standard deviation, which refers to the time resolution shows a minimum of 72.60 ps with the 30% approach compared to 75.28 ps (45%) and

79.52 ps at a rising edge of 60%. Due to the appearence of the minimum at 30% in every time difference histogram, the 30% approach was chosen as default for every further calculation.

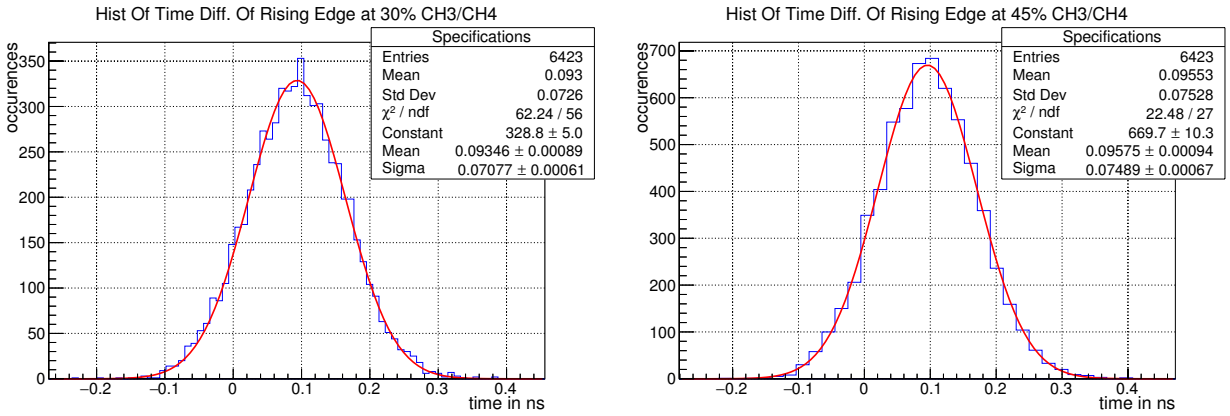

(a) **(b)**

Figure 34: Distribution of the time difference between CH3 and CH4 with rising edge at 30% (a) and rising edge at 45% (b). 80 MeV protons at 350 V bias voltage.

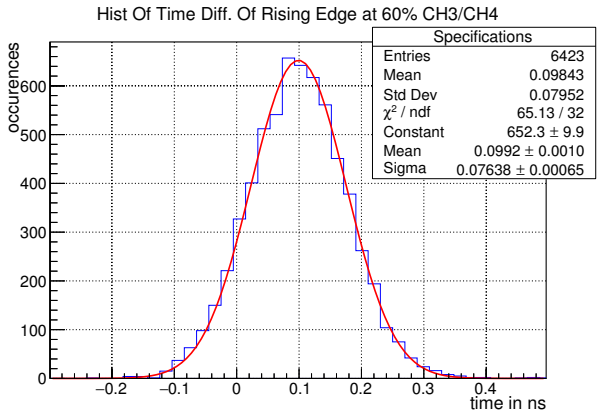

Figure 35: Distribution of the time difference between CH3 and CH4 with rising edge at 60% with 80 MeV protons at 350 V bias voltage.

Finally, the statistical data from the histograms (in the "specifications" box), calculated with functions of the ROOT software, were taken for every beam energy and/or bias voltage settings to draw all the diagrams in Sec. 4. This includes the mean value of the deposited energy (charge), the rise time, time-of-flight, as well as the time resolution. As time resolution, the standard deviation of the histograms with the rising edge at 30% was taken and calculated for each LGAD (see eq. 2.26).

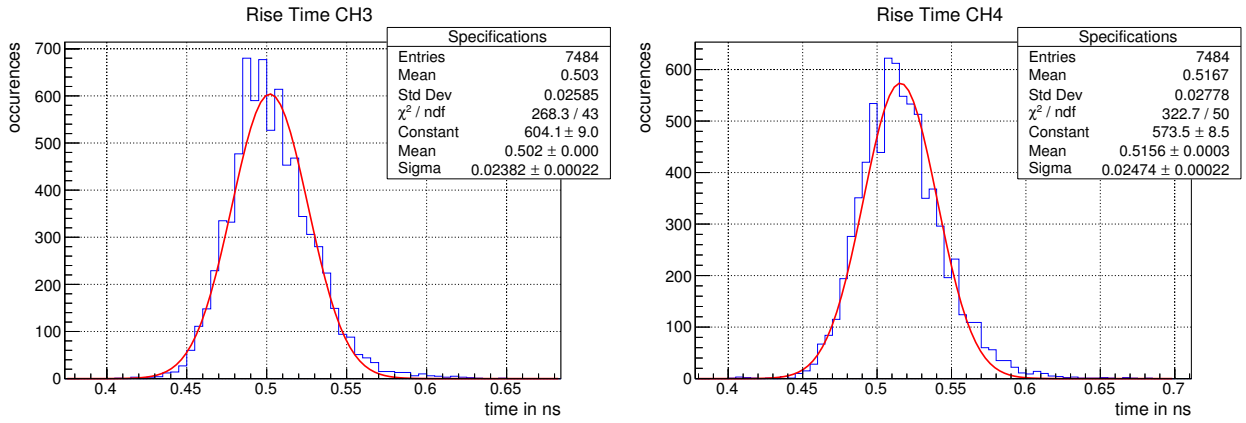

(a) (b)

Figure 36: Distribution of the rise time of the signals at channel 3 (a) and channel 4 (b) recorded with 80 MeV protons at 350 V bias voltage.

The baseline (or offset) and the noise of the signals were determined by the help of analysing the noise amplitudes excluding the detected laser pulses. The noise was put into a histogram (Fig. 37) to get the mean and the standard deviation for calculating the signal to noise ratio that can be obtained by using eq. 3.1. An error calculation was done besides the evaluation of the SNR in the software algorithm via gaussian error propagation.

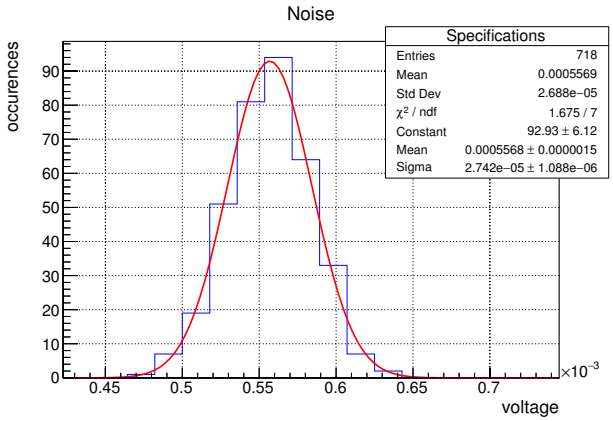

Figure 37: Histogram of the noise measured with the oscilloscope at 8 GHz DSP bandwidth setting.

$$\mathrm{SNR(dB)} = 10\,log_{10}\left(\frac{P_{\mathrm{signal}}}{P_{\mathrm{noise}}}\right) = 10\,log_{10}\left(\frac{A_{\mathrm{signal}}}{A_{\mathrm{noise}}}\right)^2 \tag{3.1}$$

3.7 Geant4 Simulation

Besides the experimental part of the work at MedAustron and the laser at the HEPHY institute, the time-of-flight calorimeter with LGADs was also simulated via a software tool called Geant4. This gives the opportunity to provide a more theoretical approach of the topic by enabling to compare with the experiment and to push the research further. Geant4 (Geometry and tracking) is a C++ based, object oriented toolkit, which uses the Monte Carlo method for simulating particle transport in matter for a predefined experimental setup. Originally developed for high energy physics experiments, it also meets the requirements for ion beam therapy. All the information on Geant4 is taken from [32] [33] [34].

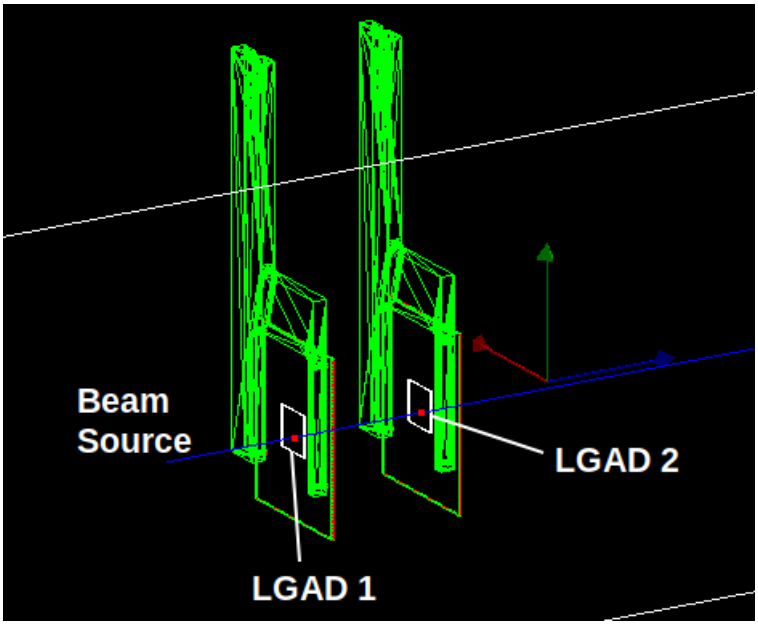

Figure 38: Visualization of the beam, starting at the beam source and the two LGAD boards with the LGAD diodes in Geant4.

Geant4 is based on the C++ environment and uses Monte Carlo methods for many particle physics by solving a mathematical problem, such as the particle transport in matter by setting up a stochastic model using random numbers. When a particle moves through air and a set of detectors e.g. as shown in Fig. 38 or through other types of matter, there is the probability of beig interrupted by different events like scattering or decay. The probability p_i of being affected by an event can be expressed as in eq. 3.2, where n is the number of various events (E_1 to E_n)

$$\sum_{i=1}^{n} p_i = 1 \tag{3.2}$$

The cross section for an event (σ_i), relative to the cross section of all available events (σ_t), defines it's probability

$$p_i = \frac{\sigma_i}{\sigma_\mathrm{t}} \tag{3.3}$$

where the cross section of all available events can be expressed as follows

$$\sigma_{\mathrm{t}} = \sum_{i=1}^{n} \sigma_i \tag{3.4}$$

By the help of a random number ξ, where $0 \leq \xi < 1$ only one of n possible events can be chosen, where ξ is used like in eq. 3.5.

$$p_1 + p_2 + ... + p_{i-1} \leq \xi < p_1 + p_2 + ... + p_i \tag{3.5}$$

Finally, the event E_i, which is the most probable happenig next, can be determined [35] [36].

Geant4 has an object-oriented structure and can be modified for individual needs in the C++ framework. It is built up as a toolkit to create geometrical models and to define elements that record information needed to simulate detector responses. With a physics library containing interaction processes, the behaviour of particles can be studied when interacting with the geometrical objects.

To get all the relevant physical quantities, such as the time- or the energy resolution first for the time-of-flight (ToF), each particle had to be labelled with a time stamp when hitting LGAD 1 and LGAD 2. In Geant4, these time stamps are extracted as the variables *GlobalTime_0* for the LGAD 1 and *GlobalTime_1* for the LGAD 2 as can be seen in Fig. 39 and 40. The time-of-flight is calculated as follows:

$$ToF = Global\,Time\_1 - Global\,Time\_0 \tag{3.6}$$

Due to the interaction of the beam with the detector material (Si, Cu, FR4) and the air, the particle's ToF differ and lead to a Gaussian distribution with mean μ_{ToF} and standard deviation σ_{ToF}. The standard deviation σ_{ToF} can be interpreted as the intrinsic time resolution, but does not hold much information when comparing with the experiment due to the whole readout electronics in a real experiment that is introducing uncertainties. So, for simulating a ToF experiment, the Gaussian distribution needs to be blurred by a custom time-resolution (σ_t) and can be blurred also with a spatial resolution (σ_x , σ_y) referring to the resolution of the detector to get the time- and further the energy resolution. The blurring of the distribution is done via the analysis program written in Python, where a distribution with a mean value of 0 and a custom standard deviation represented by the value of the time resolution is created and added up to the ToF distribution. To the positions, where the particles hit the detector, a distribution with a mean value of 0 and a standard deviation of the spatial resolution in x- or y-direction can also be added up and represents the position accuracy of the sensors.

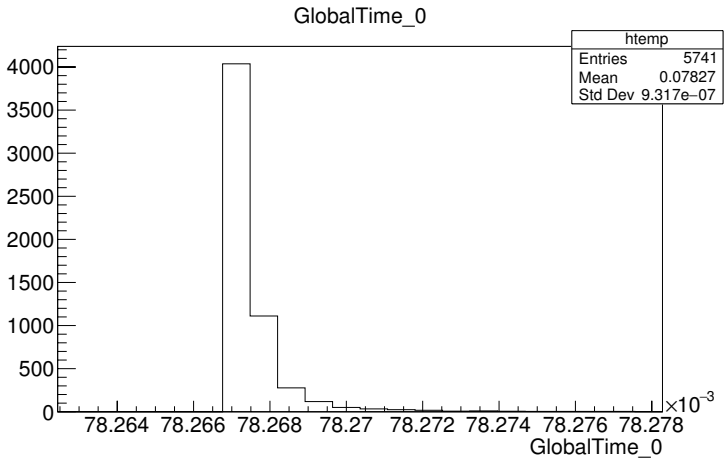

Figure 39: Distribution of the time stamps *Global Time_0* of LGAD 1

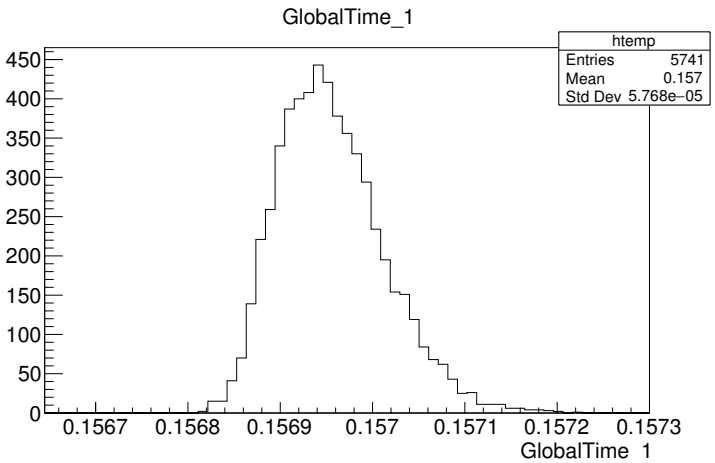

Figure 40: Distribution of the time stamps *Global Time_1* of LGAD 2

4 Results of the MedAustron beam experiment

4.1 Timeline

The patient treatments at MedAustron are performed on week days from 6:00 to 22:00, so only the weekends and night time can be used for non-clinical research. The experiments for this work took place on the following 4 shifts:

- 1^{st} shift: Sunday, 20.10.2019 EB (Early Bird: 6:00 - 14:00)

- 2^{nd} shift: Friday, 25.10.2019 VA (Vampire: 22:00 - 6:00)

- 3^{rd} shift: Saturday, 23.11.2019 EB (Early Bird: 6:00 - 14:00)

- 4^{th} shift: Sunday, 23.02.2020 RO (Royal: 10:00 - 20:00)

Between the 2^{nd} and 3^{rd}, as well as between the 3^{rd} and 4^{th} shift, laser beam measurements with the laser setup at HEPHY were taken.

4.2 Results of the beam experiment

All of the following plots are based on the raw data monitored by the oscilloscope and a detailed process of converting the raw data into these diagrams was introduced in Sec. 2.6.3 and Sec. 3.5. One important physical quantity was the deposited energy (charge) within the sensor for the comparison of the results with the simulation and the theoretical Bethe-Bloch calculations, while the latter were performed by the help of the PSTAR stopping power calculation program [6]. In Fig. 41a, the charge vs. beam energy can be seen at 300 V bias voltage, where the curve was normalized to the theoretical value at 800 MeV. The normalization had to be done, because the experiment was not calibrated, because the focus lied on the analysis of the relationship between the results rather than the absolute values.

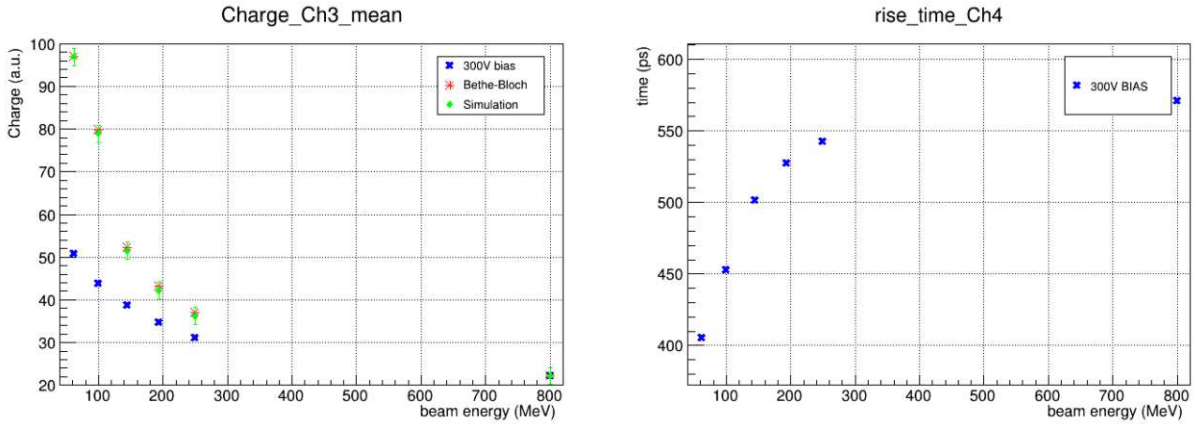

(a) **(b)**

Figure 41: a) Charge vs. beam energy at a bias voltage of 300 V. Normalized to the theoretical value at 800 MeV. b) Rise time t_{rise} of the signal vs. beam energy at 300 V.

The diagram in Fig. 41a shows that the more the beam energies deviate from the normalization point, the higher the divergence of the deposited energy is. This behavior concludes a damping in the readout circuit and is described in detail in Sec. 4.3. Although the results of the simulation will be presented in Sec. 5, they can be seen in Fig. 41a as well. It can be seen that the simulation values agree with the Bethe-Bloch ones within their uncertainties. The diagram in Fig. 41b gives the absolute values of the rise time, which increases with higher energies. The rise time plays a crucial role in terms of the time resolution, especially in the jitter- and time walk term (Sec. 2.6.2). Due to the dependence of the rise time on the bandwidth in the readout circuit and the bandwidth setting of the oscilloscope, a further study is given in Sec. 4.3.

The measurement of the time-of-flight (Fig. 42a) was performed with 300 V bias voltage and the values were normalized to the theoretical ones at 800 MeV. For the sake of completeness, Fig. 42a includes the Bethe-Bloch as well as the simulation results and it can be seen that they agree with each other, while the experimental values deviate from them. Fig. 42b shows the absolute time resolution for one LGAD (Sec. 2.6.2) at 300 V bias voltage with a minimum at 250 MeV of 56.17 ps.

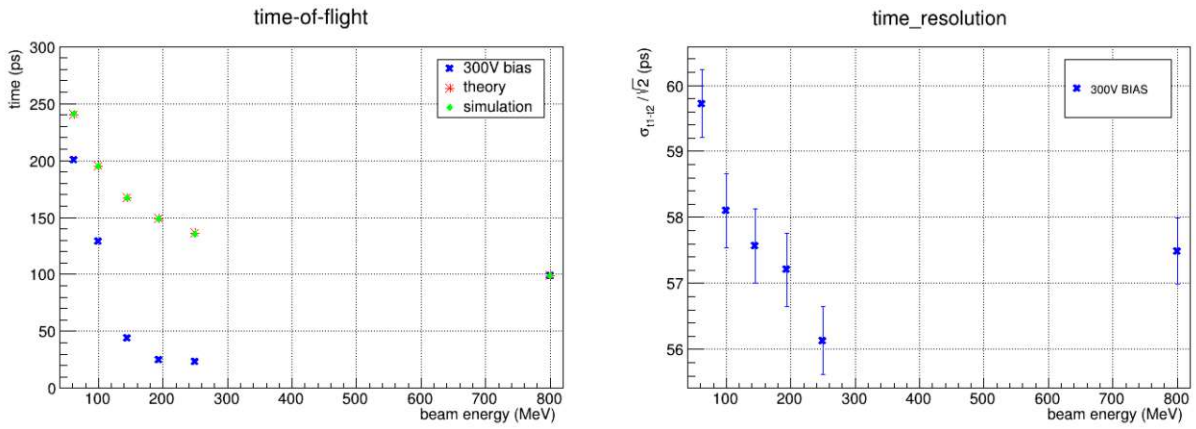

(a) **(b)**

Figure 42: a) Time-of-flight diagram with comparison of the experimental data with a bias voltage of 300 V to the theoretical- and the simulation values at different energies, normalized to the theoretical value at 800 MeV. b) Time resolution vs. beam energy at 300 V bias voltage.

For a deeper understanding of the LGADs and the results given in Fig. 41 and 42, the next section provides results of the laser tests carried out at the HEPHY institute.

4.3 Results of the laser measurements

To obtain a more detailed view of the behavior of the LGADs and the involved devices, measurements at the HEPHY laser setup were taken. While at the MedAustron experiments, 2 LGADs were involved, the laser measurements worked with 1 LGAD at a time. As an example, Fig. 43(a) shows a laser pulse with the 500 MHz bandwidth setting and in Fig. 43(b) the 8 GHz bandwidth setting was used. As explained in Sec. 2.6.3 and Sec. 3.5, the signals from the laser experiments were analysed by the C++ analysis software. The analysed data was put into histograms to finally get the diagrams with the overview of the results.

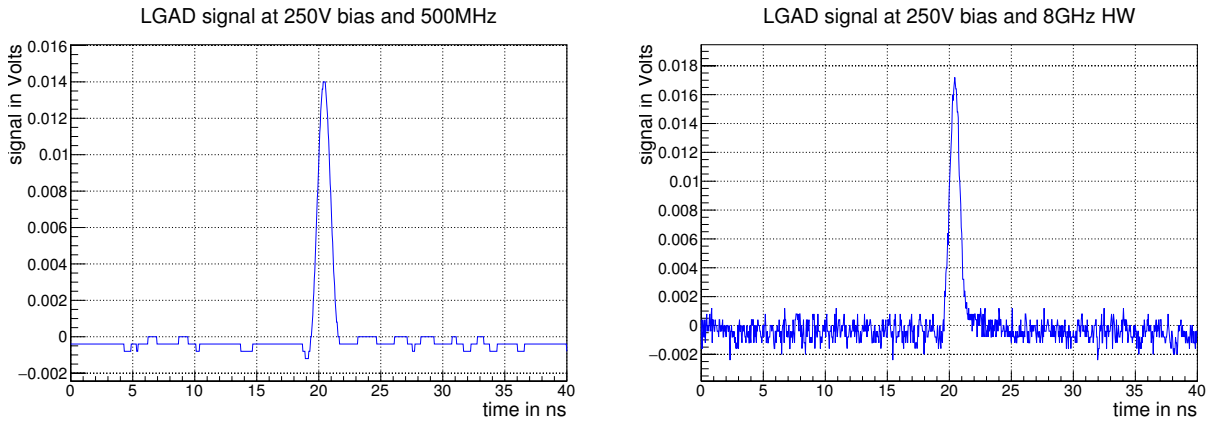

(a) (b)

Figure 43: Laser pulses detected by the LGAD at 250V bias and recorded by the oscilloscope at 500 MHz (a) and 8 GHz HW (b).

In Sec. 3.6, the process to obtain the rise time and the SNR was explained, while in Fig. 44, the results of the bandwidth test is shown.
The noise at 500 MHz is less pronounced than at 8 GHz as can be seen in Fig. 43. Fig. 44b shows that with an increasing of the bandwidth, the SNR improves. A broader bandwidth allows the adding of higher frequency components of the noise to the signal, but also shows a higher peak (Fig. 43). This phenomenon is connected to the SNR decrease with higher bandwidth (Fig. 44b). When examining the difference between the DSP (digital signal processing) and the HW (hardware/analog filters) option at 8 GHz, it can be clearly seen, that the SNR of the DSP setting shows a higher value than the HW setting. The rise time comparison (Fig. 44a) shows that the 500 MHz bandwidth setting give the highest value in rise time. This was expected due to the relation of the bandwidth (f_u) and the rise time (t_r) as shown in eq. 4.1 that was taken from [15]:

$$t_r = \frac{0.35}{f_u} \tag{4.1}$$

Because of the limitation of the bandwidth to 500 MHz, the signal is not able to rise faster than 0.7 ns. In Fig. 44a, the intrinsic rise time of the LGAD can be seen at 500 MHz, while the lower values of the rise time at higher bandwidths indicate a limitation of the bandwidth due to the electronic readout circuit. The individual rise times add in quadrature and are caused mainly by the amplifiers and the interconnection of input capacitance and -resistance. The minimum of the rise time at 2 GHz and the maximum of the SNR at 500 MHz lead to the compromise of choosing 1 GHz bandwidth.

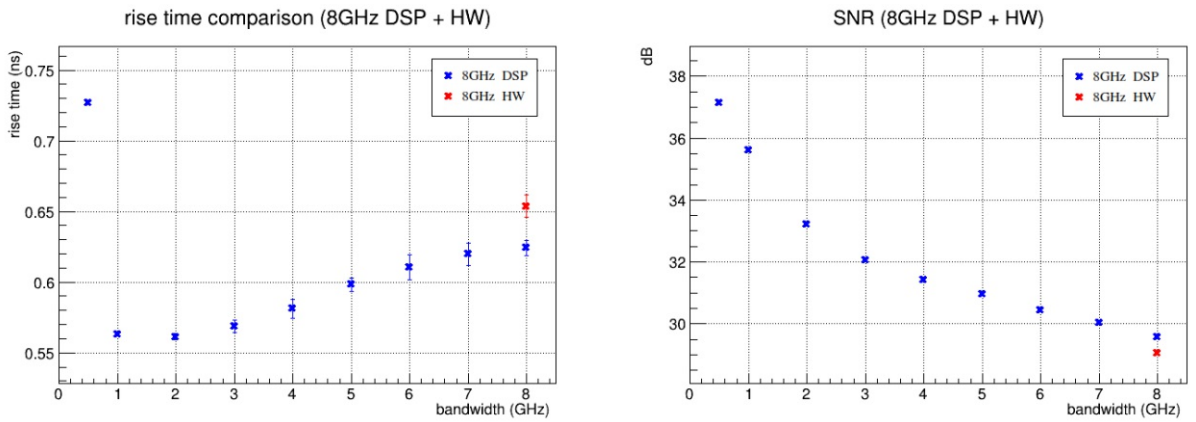

(a) (b)

Figure 44: (a) Bandwidth vs. rise time plot, where the minimum is at 2 GHz. The rise time at 8 GHz is higher when using the HW-setting than the rise time measured with the DSP-setting. (b) SNR in dB vs. bandwidth. It can be seen that, with increasing bandwidth, the SNR decreases. At 8 GHz, the SNR of the DSP- is larger than the HW-setting.

Besides the bandwidth setting on the oscilloscope, the laser intensity and the bias voltage were varied and the energy deposition (charge) was recorded and put into the plots in Fig. 45 and 45b. The results concerning the amplification of the LGAD signal show that on the one hand, the second stage amplifiers (cividecs) saturate in a very early stage of the laser's intensity (Fig. 45), and on the other hand, the intrinsic amplification shows a different gain by an increase of the bias voltage (Fig. 45b). For example at 350 V, LGAD 1 shows a gain of 10.5 and LGAD 2 a gain of 10.9. However, in the experiment, the bias voltage of LGAD 1 and LGAD 2 were set to the same level, because the influence was assumed to be negligible. With this results and the saturation of the amplifiers, the setup at MedAustron was rebuilt and the results will be shown in the next chapter.

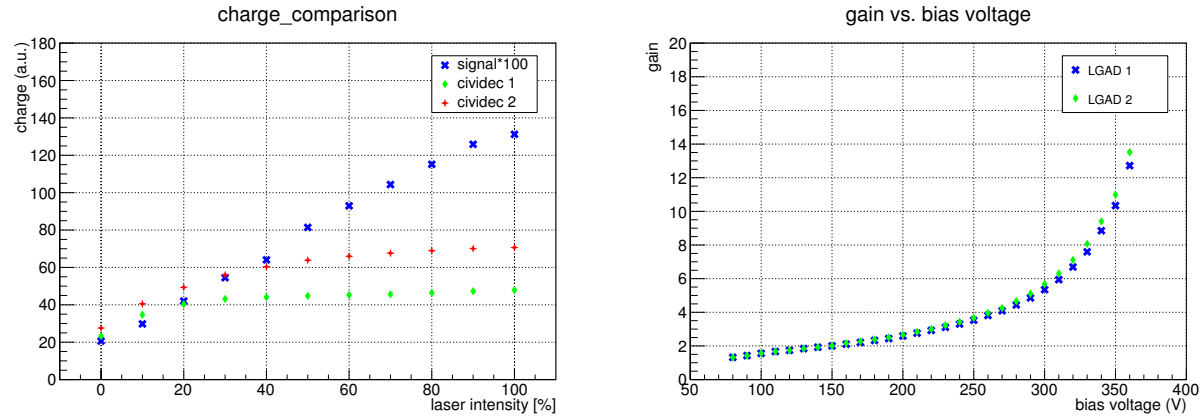

(a) (b)

Figure 45: a) Saturation of the second stage amplifiers (cividec) b) Different strength of amplification of LGAD 1 and 2.

4.4 Continuation of the beam experiment's results

The following results were derived from a different MedAustron experimental setup without the cividec second stage amplifiers (Sec. 3.4.3). This change in the setup was necessary due to the saturation of the used amplifiers as was shown by the laser measurements in Sec. 4.3. Another change was the oscilloscope bandwidth setting to 1 GHz, because according to Fig. 44 in Sec. 4.3, the best recording performance could be achieved with this setting. To affirm the results of the laser measurements concerning the bandwidth setting, the test was also conducted at MedAustron and showed a similar outcome as can be seen in Fig. 46, where the lowest time resolution at 194 MeV and 350 V bias voltage could be achieved at 500 MHz. Due to the rise time at a bandwidth of 500 MHz showed the highest value in the used bandwidth range, the oscilloscope was set to 1 GHz represented by the shortest rise time in Fig. 46b.

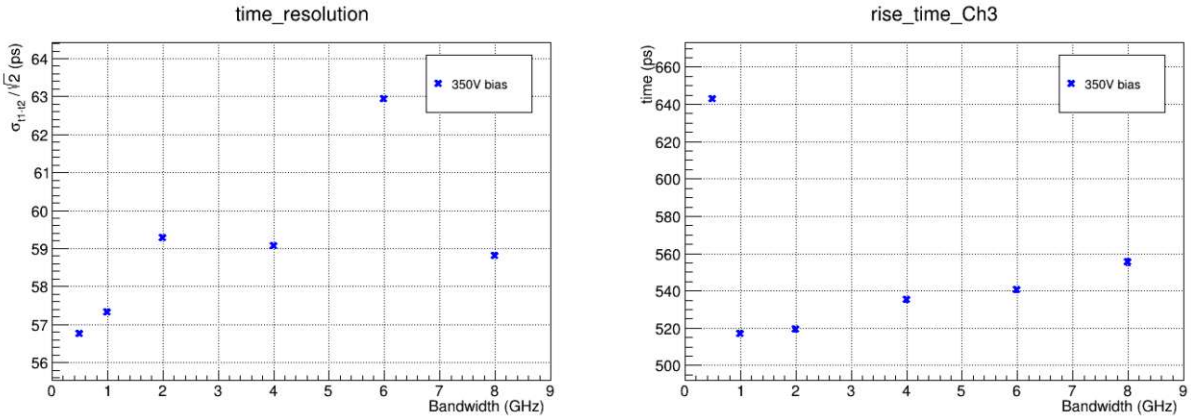

(a) **(b)**

Figure 46: a) Time resolution vs. bandwidth at a fixed bias of 350 V.
b) Rise time vs. bandwidth at a fixed bias of 350 V.

Fig. 47a represents the charge of LGAD 1 at 350 V bias voltage and without the saturating amplifier, it can be seen that the new setup presented more precise results, although the values of the experiment still lack accordance to the theoretical values. The experimental results in Fig. 47a are normalized to the value at 800 MeV and the lower the energy, the greater the deviation to the theoretical values gets. The third data set in Fig. 47a are the results from the simulation and their respective uncertainites, which agree with the Bethe-Bloch values. According to the Bethe-Bloch equation, the charge is increases with a decrease of the beam energy as in Fig. 47a. Combined with the signal formation process described in Sec. 2.6 as well as Ramo's theorem, the values of the rise time are expected to decrease with higher beam energies and bias voltages. Despite the results in Fig. 41b, in which the rise time increases with higher beam energies, due to an unwanted filtering of the frequency spectrum of the signal, the results in Fig. 47b meet the expectations.
Fig. 47b and Fig. 48b give an example on how the bias voltage affects the rise time and the time resolution. With higher bias voltage, the rise time and the time resolution decrease. The time-of-flight results (normalized to the beam energy at 800 MeV) can be seen in Fig. 48a, where the simulations follow the Bethe-Bloch values, but the experimental results deviate from them. In Sec. 5.1, it is explained that the deviation determines from a time-of-flight distance of 2.5 cm, which is too short, introducing the

uncertainty. The time resolution given in Fig. 48b shows that with a beam energy of 80 MeV a minimum value of 52 ps was reached, though the deviation of the values in the low energy region makes it difficult to seperate the results.

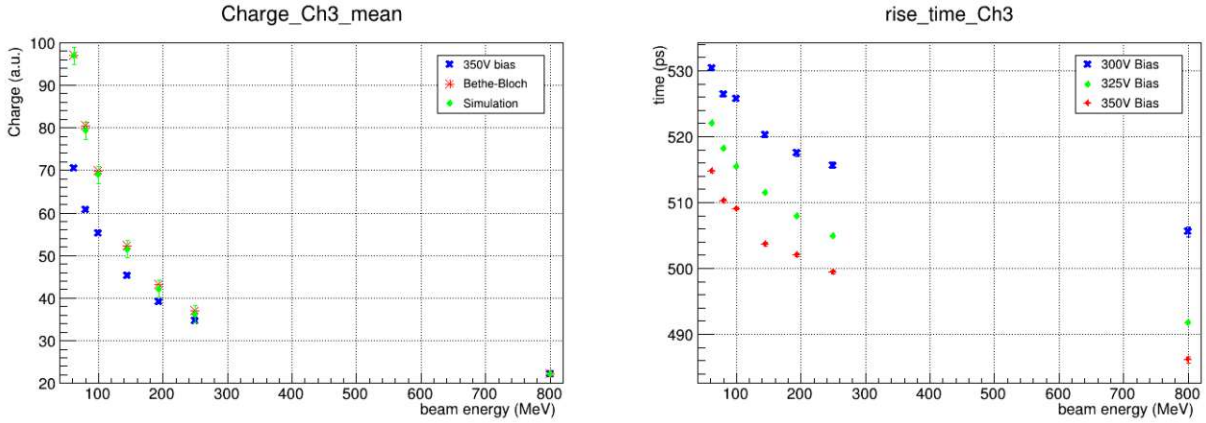

(a) (b)

Figure 47: a) Charge vs. beam energy at a bias voltage of 300V. Normalized to the theoretical value at 800 MeV. b) Rise time t_{rise} at different bias voltages.

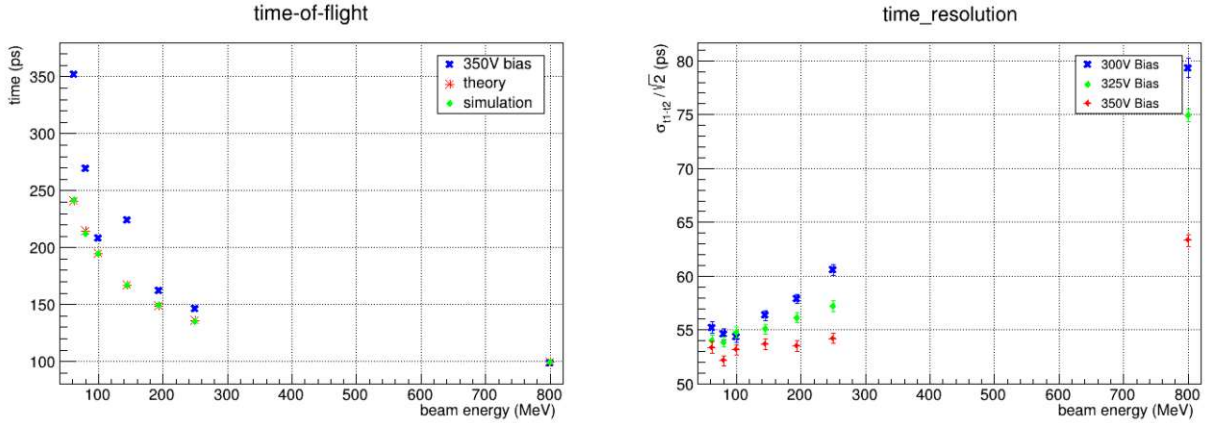

(a) (b)

Figure 48: a) Time-of-flight diagram normalized to the value at 800 MeV. b) Time resolution vs. beam energy at different bias voltages.

Next to the proton beam, also the beam of carbon ions ($^{12}C^{6+}$) was used for the studies. The setup at MedAustron without the cividec amplifiers that was used for the proton beams went into action again for carbon and the results differ significantly from the ones obtained with protons.
In Fig. 49a, a linear-like dependency on the bias voltage can be seen with a minimum at 200 V, while the minimum of the deposited energy depending on the beam energy as shown in Fig. 49b has it's minimum at 400 MeV/n. Comparing Fig. 49b (charge of protons) to Fig. 47a (charge of carbons), it can be seen that also the results of the deposited energy of the carbon beam does not agree with the simulation values and support the thesis of another uncertainty in the readout electronics.

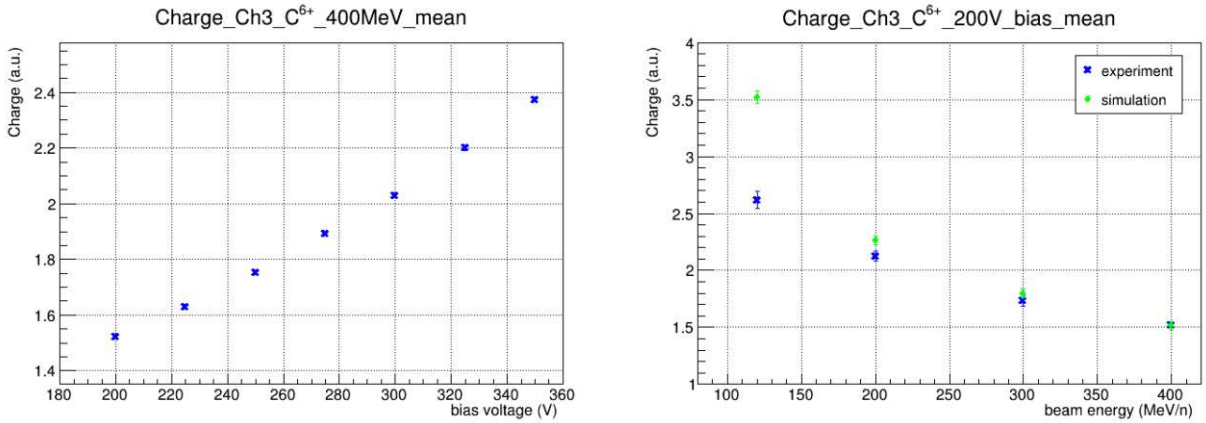

(a) (b)

Figure 49: As normalization point, the value at 400 MeV/n and 200 V bias voltage was chosen for both diagrams, where the basis is the charge value at 400 MeV/n from the simulation. a) Charge vs. bias voltage at a fixed beam energy of 400 MeV/n. b) Charge vs. beam energy at a bias voltage of 200 V for the experiment- and the simulation values.

The results of the rise time depending on the bias voltage are presented in Fig. 50, where the carbon beam energy was fixed to 400 MeV/n and it can be seen, that the rise time gets lower with increasing bias voltages. Fig. 51 shows the difference between the rise time behavior depending on the beam energy at a fixed bias voltage of 200 V (Fig. 51a) and 300 V (Fig. 51b). With 200 V bias voltage, the LGAD operates in the low gain area, while the gain at 300 V is 3 times as high, as can be seen in Fig. 45b. At 200 V bias voltage, the increasing of the rise time from 120 MeV/n to 400 MeV/n is 25 ps, while at 300 V, this took only 5 ps. However, the signal of the LGADs had a high quality even at low gain (200 V bias), so the time resolution is below 44 ps, as can be seen in Fig. 52b. Fig. 52a gives the time resolution versus the bias voltage and in contrast to the proton case, the time resolution of carbons increases with higher bias voltage. The time-of-flight diagrams in Fig. 53a and 53b for carbons are connected with high uncertainties, but this issue will be discussed in detail in Sec. 5.1.

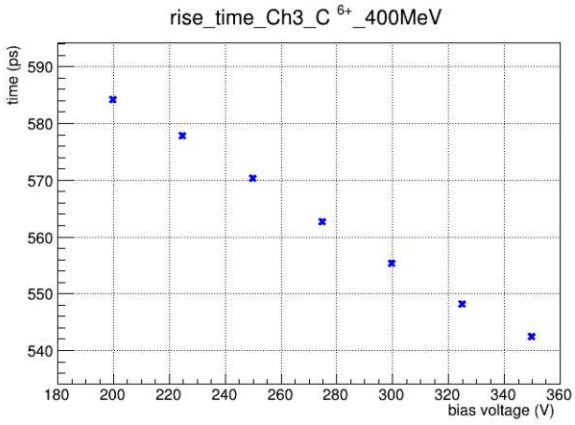

Figure 50: Rise time t_{rise} at diff. bias voltages and fixed beam energy of 400 MeV/n.

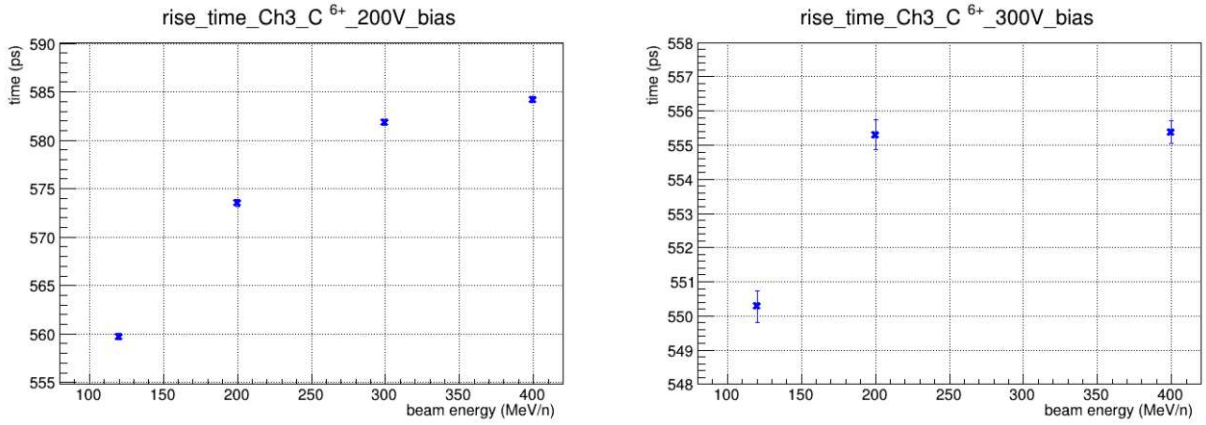

(a) **(b)**

Figure 51: Rise time t_{rise} for carbons at different energies and fixed bias voltage of a) 200 V and b) 300 V (The value at 300 MeV/n was not recorded).

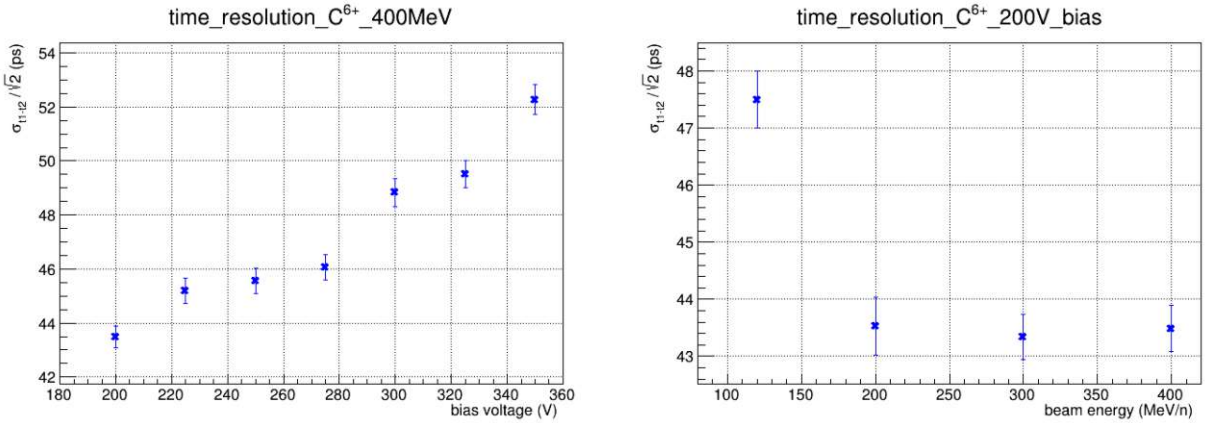

(a) **(b)**

Figure 52: a) Time resolution vs. bias voltage at a fixed beam energy of 400 MeV/n. b) Time resolution vs. beam energy at a fixed bias voltage of 200 V

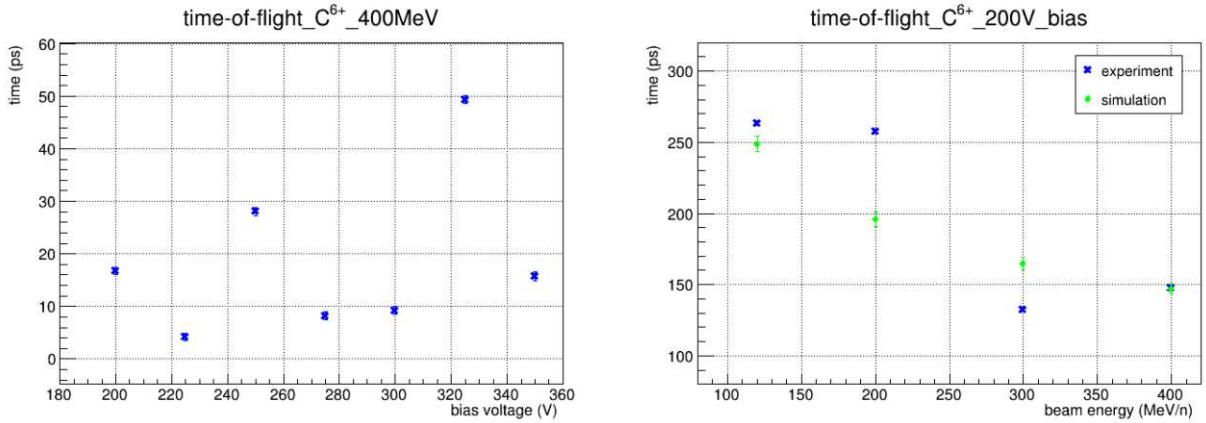

(a) **(b)**

Figure 53: a) Time resolution vs. bias voltage at a fixed beam energy of 400 MeV/n. b) Time resolution vs. beam energy at a fixed bias voltage of 200 V

5 Results of the Simulation with Geant4

5.1 Comparison of Simulation and Experiment

In order to investigate the results of the MedAustron experiments further, the simulation of the ToF-setup was simulated in Geant4 (Fig. 38). The setup consisted of two LGAD boards that were separated by 2.5 cm air and a beam source 1 cm in front of the first LGAD. The LGADs themselves were created with the specifications stated in Sec. 3.3.2 and got hit by protons and carbons with the beam energy and specifications of the particle accelerator at MedAustron (Sec. 3.1).

The simulation's standard deviation of the time distribution is based on the time stamps extracted by Geant4 as was explained in Sec. 3.7 and can be seen in Fig. 39 and Fig. 40. While in the experiment, the term "time resolution" is used for the capability of the ToF setup, describing how precise the time can be measured, in the simulation, the time resolution σ_t is a variable, which can be used to blur the measured arrival time of the individual hits. This blurring simulates the uncertainty of the sensor-to-readout electronics and is used for the simulation to analyse the dominating factors of the standard deviation of the ToF (σ_{ToF}) when changing specific parameters. The standard deviation of the ToF in the simulation without blurring with a time resolution and the setting of the spatial resolution (σ_x, σ_y) being 0 µm only contains the difference of the ToF due to scattering of the particles at the detector material and a resulting deviation of the straight line flight path (Sec. 5.2). This is the main difference when comparing to the experiment, where the time resolution is mainly characterised by the signal creation in the detector and the readout electronics.

In this section, where the simulation is compared to the experiment, the simulation's standard deviation of the time stamps was not blurred with a custom time resolution ($\sigma_t = 0$ps) or with a spatial resolution ($\sigma_x = \sigma_y = 0$µm). This is because the absolute time resolution values were not the focus in the first comparison but the change of the values with the primary energy. For comparison, a normalization point is required for the experiment's diagrams, chosen to be the simulation's value at 100 MeV for protons and 200 MeV/n for $^{12}C^{6+}$ carbon ions. The results can be viewed in Fig. 54 for protons and in Fig. 55 for $^{12}C^{6+}$ carbon ions, where the ToF standard deviation is presented relative to the respective mean ToF μ_{ToF}.

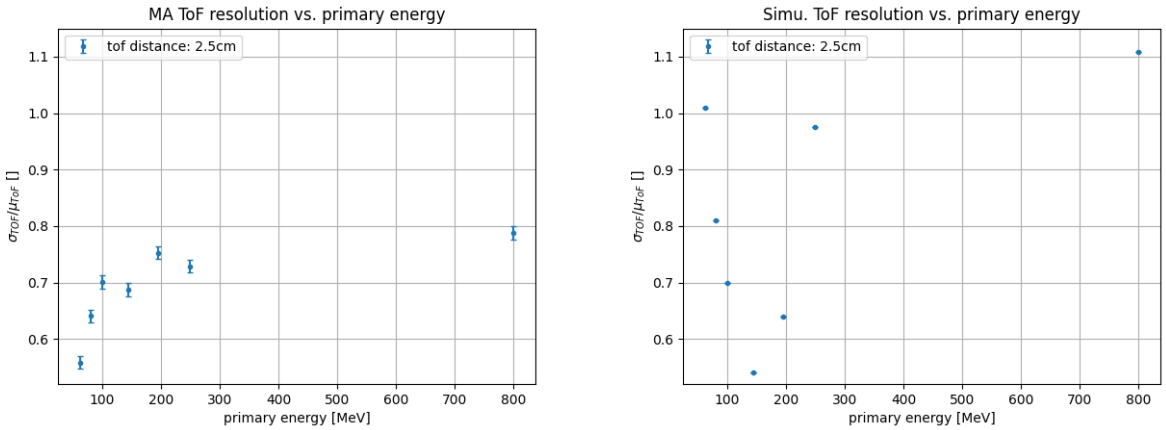

(a) (b)

Figure 54: ToF resolution (ToF standard deviation) of a) MA proton experiment and b) simulation with protons. The diagram of the MA proton experiment in a) is normalized to the simulation value at 100 MeV for comparison purpose.

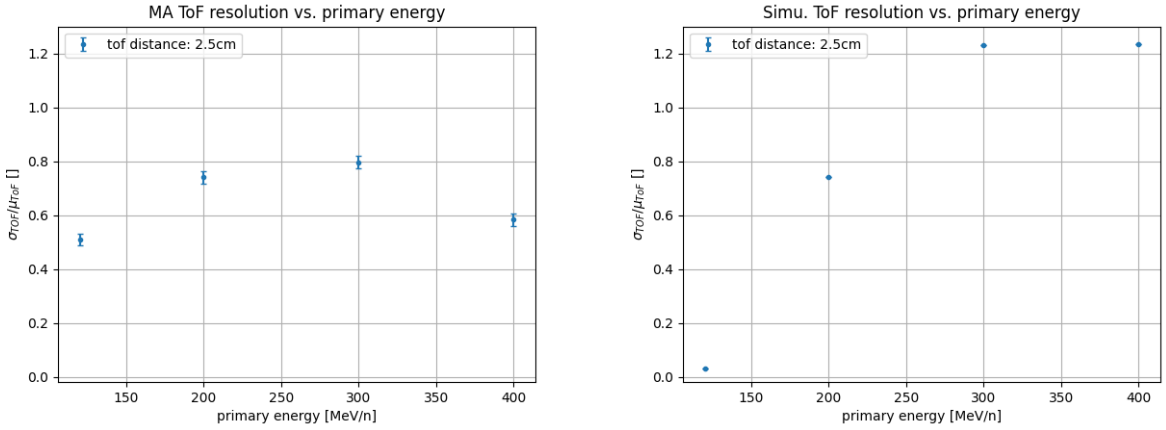

(a) (b)

Figure 55: ToF resolution (ToF standard deviation) of a) MA carbon experiment and b) simulation with carbon. The diagram of the MA carbon experiment in a) is normalized to the simulation value at 200 MeV/n for comparison purpose.

Neither the results of protons nor the ones with carbons give a good opportunity for comparing the experiment with the simulation, because the results seemed to be randomly arranged, which suggests that the uncertainty of the time resolution in the experiment and the standard deviation of the time stamps of the simulation is too high.
A more detailed study of the simulation revealed, that the longer the time-of-flight distance, the lower is the relative uncertainty of the measured ToF of the particles and ergo the standard deviation of the ToF distribution as can be seen in Fig. 56.

With a ToF distance of only 2.5 cm, the relative uncertainty is too high for a successful time-of-flight experiment. The results when using a ToF distance being 25 cm or more are better than the ones with a shorter distance.
The drawback of simulations with ToF distances $\geq$ 25 cm and the LGADs used at the experiment with their active area being just 1 mm^2 is that only a very small fraction of the primary particles reach the second LGAD. This relation leads to the diminishing of the spot size of the beam from 8×8 mm to 2×2 mm and an upscaling of the LGADs from 1 mm^2 to 1 m^2. For completeness sake, the mean time-of-flight for ToF-distances of 2.5 cm to 100 cm are shown in Fig. 57.

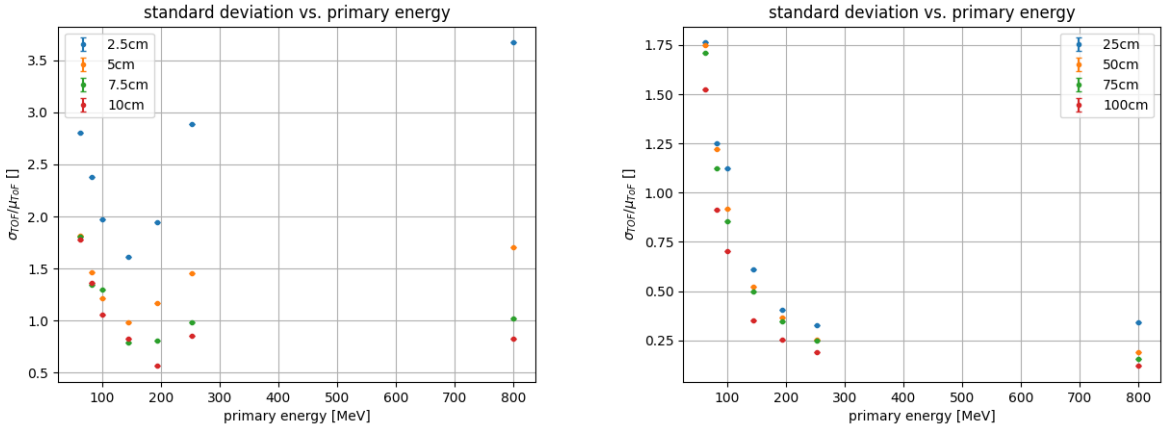

(a) (b)

Figure 56: a) ToF standard deviation for ToF distances from 2.5 cm to 10 cm for protons. b) ToF standard deviation for longer ToF distances from 25 cm to 100 cm for protons. The lower standard deviation for longer ToF distances can be seen.

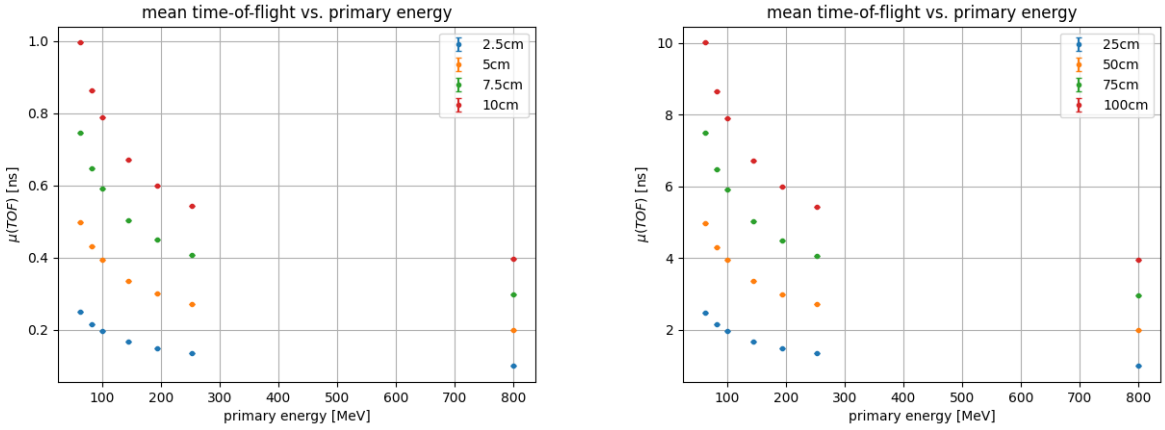

(a) (b)

Figure 57: a) Mean ToF for distances from 2.5 cm to 10 cm for protons. b) Mean ToF for longer ToF distances from 25 cm to 100 cm for protons.

5.2 Simulation of an optimised ToF setup

The comparison of simulation and experiment was difficult because of the high uncertainties introduced by a too short ToF distance. This distance had to be 2.5 cm in the MedAustron experiment to provide particle hits on both LGADs with their 1 mm² sensitive area. In the simulation, the parameters of the whole setup could be chosen individually and the optimum settings could be figured out. The analysis in this chapter include the influence on the time- and energy standard deviation and the mean energy uncertainty, due to the material budget, the beam spot size, the LGAD size, ToF distance, number of planes and the spatial resolution, as well as the difference of the particle species.

Unless otherwise stated, the simulations in this section were executed with the following settings:

- world material: air
- beam source: 1 cm in front of LGAD 1
- beam spot size: 2×2 mm and 8×8 mm
- primary particles: 1 Mio.
- LGAD area: $1\,\text{m} \times 1\,\text{m}$
- ToF distance: 1 m
- time resolution: σ_t = variable (*e.g.* : 0, 30 ps)
- spatial resolution: $\sigma_x = \sigma_y = 0 - 100\,\mu\text{m}$

5.2.1 Physical background and procedures of the simulations

In this chapter, the ToF distance was set to 1.0 m, because the standard deviation of the ToF gets significantly higher with lower flight distance (Fig. 56b) and 1 m is a distance that could be assembled in a real experiment without being oversized to the experimental facilities. By setting the time resolution to 0 ps per detector plane, the isolated effect of the scattering of the particles, when varying the material budget, could be studied (Sec. 5.2.2). To obtain the results of the combined effects of scattering and the intrinsic time resolution of the detectors, the distributions of the particle's arrival time was blurred with time resolutions of 30 ps, 50 ps and 100 ps (Sec. 5.2.3 and Sec. 5.2.4). Similarly, the spatial resolution was set to 0 µm in order to obtain the deviation of the straight line flight path with infinite precision. In Sec. 5.2.9 the impacts of higher values of the spatial resolution are studied. A schematic overview of the simulation is shown in Fig. 58, where two possible flight paths as an example are shown. When using 100k or more primary particles in the simulation, a distribution of the particle hits in x- and y-direction on the detector area can be obtained (Fig. 59) and lead to another statistical distribution of the real flight path length with the mean path length and its standard deviation as shown in Fig. 60. For detecting the scattered particles, the area of the LGADs were increased to 1 m × 1 m, where $> 98\,\%$ of the hits could be recorded with the second LGAD and the rest were declared as statistical outliers.

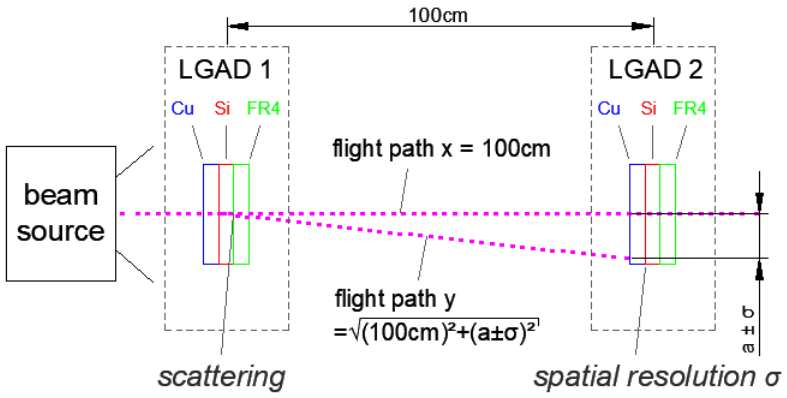

Figure 58: Schematic view of the simulation setup and two possible flight paths (x, y) due to scattering. The spatial resolution is a measure of the precision of the particle's hitting point on the detector plane.

A sensor consists of different materials and the material budget describes the individual material's thickness. This thickness is given in units of the material's specific radiation length X0, where X0 is the average distance over which the energy of an intruding particle is reduced by $1/e$ due to the interaction with matter [37]. In the case of the LGADs in the experiment, which consist mainly of silicon (Si), copper (Cu) and FR4 (epoxy-resin glass-fabric composite) the radiation lengths, as extracted from [38] and [39] are:

$$\mathrm{X0(Si)} = 9.37\,\mathrm{cm};\quad \mathrm{X0(Cu)} = 1.44\,\mathrm{cm};\quad \mathrm{X0(FR4)} = 16.76\,\mathrm{cm} \tag{5.1}$$

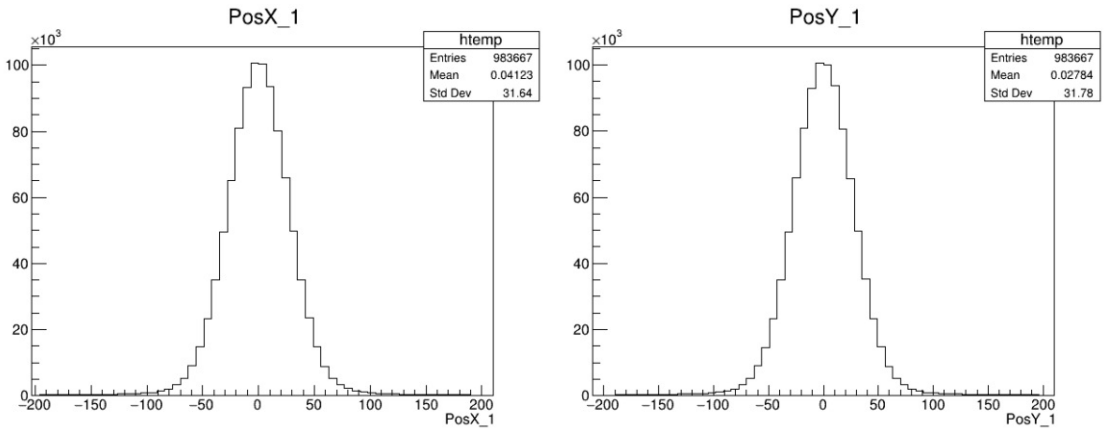

(a) (b)

Figure 59: Distribution of the particle hits on the detector area in a) x-direction and b) y-direction. The distribution was recorded with 100 MeV protons, which undergo scattering on 1.51 % X0 equivalent material thickness.

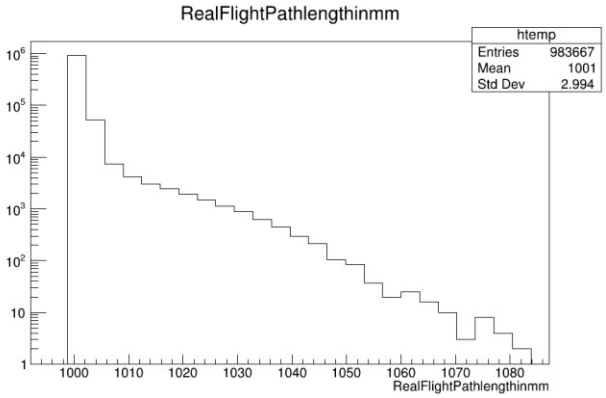

Figure 60: Distribution of the flight paths for 100 MeV protons due to scattering in the first detector with an equivalent material thickness of 1.51 % X0.

For the time- and energy standard deviation plots at different material budgets, the thickness for FR4 remained the same at all runs (FR4 thickness: 0.1 mm = 0.0568 % X0) and was chosen to such a small value to keep the influence of the scattering to a minimum. Also, the Si thickness was set to a fixed thickness of 50 µm (0.0534 % X0) based on the specification of the real LGAD (Sec. 3.3.2). The Cu thickness was used as the variable in the material budget analysis and is given in units of the radiation length X0.

The energy loss of the particles when traversing through matter needs to be considered as well. The following histograms show the distribution of the particle's energies after their interaction with the detector material. For comparison purpose, protons with beam energies of 100 MeV and 800 MeV were chosen, as well as three different custom time resolutions σ_t: 0 ps, 30 ps, 100 ps. The thickness of the detector was set to a fixed value of 0.7 % X0. In Fig. 61 the difference of the energy loss between 100 MeV (in the range of 1 %) and 800 MeV (in the range of 0.05 %) can be seen. When blurred with a time resolution σ_t of 30 ps (Fig. 62) and 100 ps (Fig. 63), the results show a broadening of the distribution for both beam energies.

It can be concluded that with higher time resolution, the broader the distribution gets. The broadening of the energy distribution of 800 MeV protons is more pronounced when applying a time resolution blurring, compared to 100 MeV protons. This is because of the higher velocity of 800 MeV protons and the subsequently higher relative uncertainty in time measurement, from which the energy measurement is derived.
Based on the data of these histograms the plots concerning the mean energy uncertainty ΔE and the energy standard deviation $\sigma(\Delta E)$ were created.

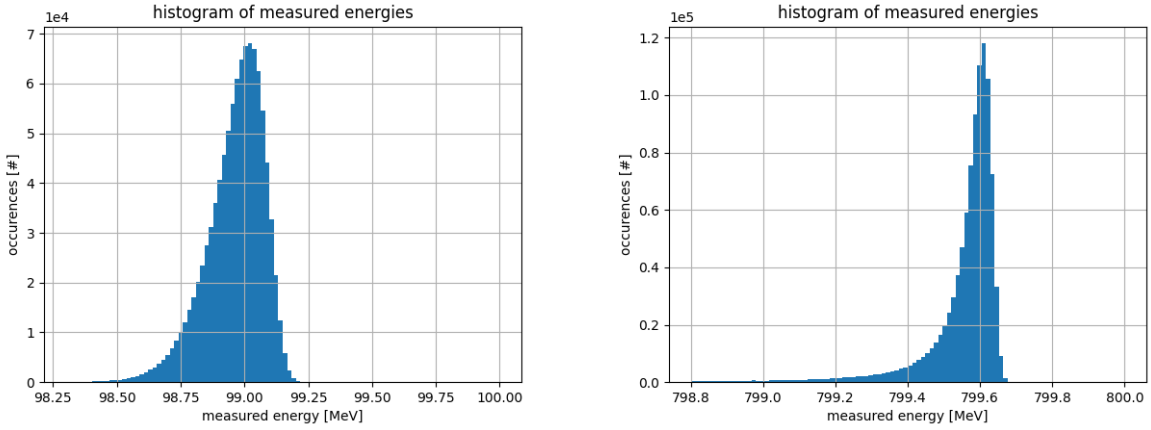

(a) (b)

Figure 61: Histogram of the measured energies with a time resolution of 0 ps and a beam energy of a) 100 MeV and b) 800 MeV.

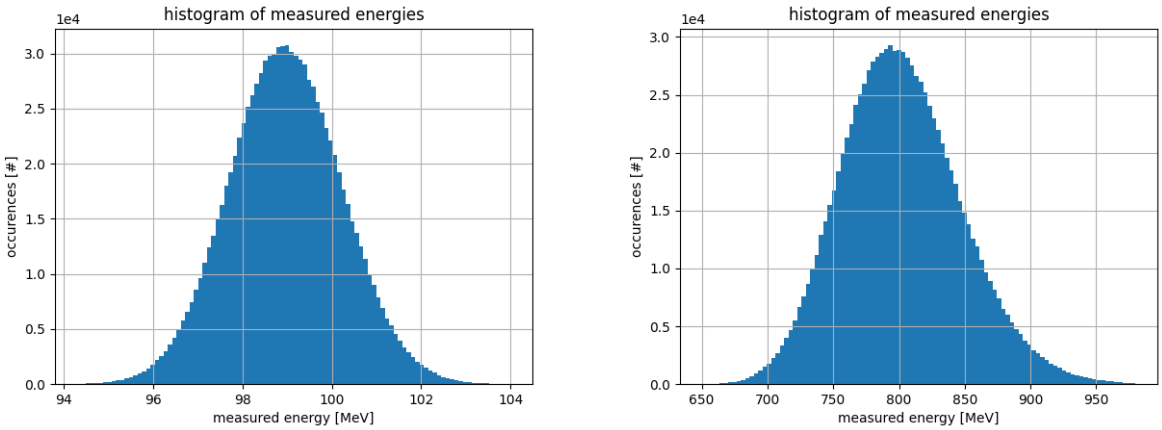

(a) (b)

Figure 62: Histogram of the measured energies with a time resolution of 30 ps and a beam energy of a) 100 MeV and b) 800 MeV.

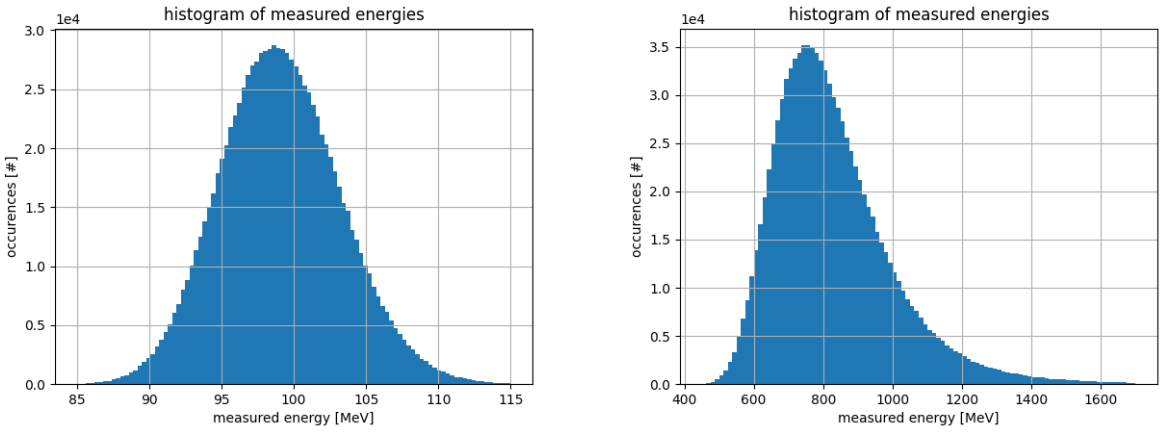

(a) (b)

Figure 63: Histogram of the measured energies with a time resolution of 100 ps and a beam energy of a) 100 MeV and b) 800 MeV.

For the standard deviations σ_t, σ_E and $\sigma(\Delta E)$ an additional uncertainty calculation was done via the Python's analysis program, where a function for a Gauss fit of the ToF- and energy distributions was written to obtain the fit parameters and their uncertainties. Fig. 64 shows an energy distribution with a fitted Gauss function for a simulation with 400 MeV protons, 3.54 % X0 material budget and 30 ps time resolution. In this example, the obtained relative energy resolution was calculated to be 3.14 % and the uncertainty in the standard deviation's fit parameter 0.0014 % with consideration of gaussian uncertainty propagation. As can be seen in Fig. 61, 62 and 63 the histograms show a convolution of a Landau- and a Gauss distribution, due to the asymmetrical energy deposition in thin absorbers (Sec. 2.3) on the one, and the Gaussian blurring of the distribution for the custom time resolution of the detectors on the other side. In Fig. 61 the influence of the Landau distribution can be recognised, where the distribution of the measured energies is mirrored vertically to the distribution of the absorbed energies in the detector as was visualized in Sec. 3.6. This is because in the histograms here, not the absorbed energy is shown, but the initial kinetic energy of the particles minus the absorbed energy in the detector.

Due to the non-linear relation between the ToF and the measured energy of the particles, the asymmetry of the energy distributions moves from the lower energy side to the higher energy side of the histograms when the values of the time resolution increase. For 100 ps and 800 MeV, as it is the case in Fig. 63b, this results in a shifting of the distribution towards the right hand side. Despite the convolution of a Landau- and a Gauss distribution of the measured energies, as a first approximation a Gaussian fit-function is valid because the uncertainties of the standard deviation's fit parameters are not larger than 0.002 % based on the standard deviation and have a negligible influence on the results. However, the values of these uncertainties are visualized as uncertainty bars in the standard deviation plots in the following sections.

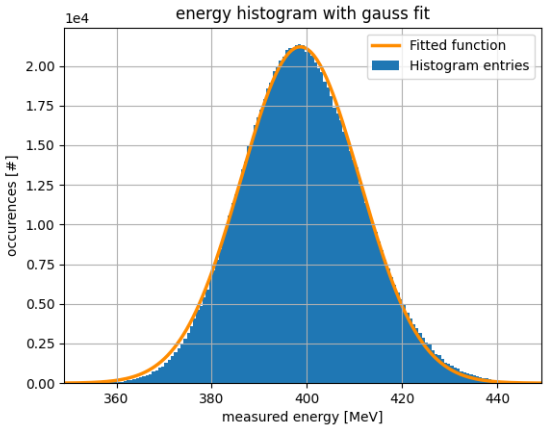

Figure 64: Gauss fit of the measured set of energies as simulated with 400 MeV protons, 3.54 % X0 material budget and 30 ps time resolution.

5.2.2 Material budget with protons and 0 ps time resolution

The results in Fig. 65a show the standard deviation of the time-of-flight $\sigma(ToF)$ due to the scattering of the beam and its deviation from the straight line flight path as a function of the beam energy at different material budgets. In Fig. 65a the maximum of the standard deviation can be seen at 60 ps with 100 MeV protons and a material budget of 34.9 % X0 that represents a thickness of Cu of 5 mm. The Cu layer of the real LGAD is 105 µm thick (0.7 % X0) and gives an intrinsic standard deviation of 9 ps for 100 MeV protons. At energies $>$ 200 MeV, the standard deviation drops rapidly.

Besides the deviation of the time-of-flight due to scattering, the decrease of the particle's energy, when interacting with the detector's material, are considered. The beam energies (e.g. in Fig. 65a) are the initial particle's energies E_{init} before interacting with the detector material and are governed by deviations when hitting material due to loss of a part of their energy when being scattered. These deviations in energy increase with higher material budget (Fig. 66b) and have to be known, when using it in the calculations. The measured energy of the particles in the ToF experiment follow a distribution (Fig. 61, 62, 63) with a mean energy $\mu(E)$ and a standard deviation $\sigma(E)$. The plot in Fig. 65b shows the standard deviation $\sigma(E)$ normalized to the beam energy E_{init} and can be interpreted as the precision of the energy measurement.

It can be seen that the different material budgets have the greatest influence on the particle beam at 100 MeV, while at energies $>$ 100 MeV and material budgets $<$ 5 % X0 the deviation from the mean energy is $<$ 0.2 %. The accuracy of the energy measurement can be seen in Fig. 66a, where the deviation ΔE from the beam energy to the measured mean energy $\mu(E)$, normalized to E_{init} is drawn. The mean energy uncertainty ΔE is derived from the distribution of the energy differences between E_{init} and the measured energies that is connected to an energy standard deviation $\sigma\left(\Delta E\right)$ (Fig. 66b).

Based on the information given in Fig. 65b, it can be concluded that the standard deviation for measuring the mean energy $\mu(E)$ for an beam energy of 100 MeV and 35 % X0 as an example, is 1.7 %. The accuracy for this measurement is 18 % as can be seen in Fig. 66a and this value can be obtained with a precision of 0.85 % (Fig. 66b). Relative to

the accuracy, the measurement result in this example is precise, but lacks in accuracy. In short, with a higher beam energy and a lower material budget, an increasing of precision $\sigma(E)$ and accuracy ΔE can be obtained, as well as a more precise determination $\sigma\left(\Delta E\right)$ of the accuracy ΔE. Due to the higher energy loss with increasing material budget and the findings of the mean energy uncertainty ΔE, the standard deviations σ(ToF) and $\sigma(E)$ can be readjusted according to the measured energies instead of the initial particle's energies E_{init}. Despite this correction, the energy standard deviation $\sigma\left(\Delta E\right)$ still accounts for uncorrectable uncertainties.

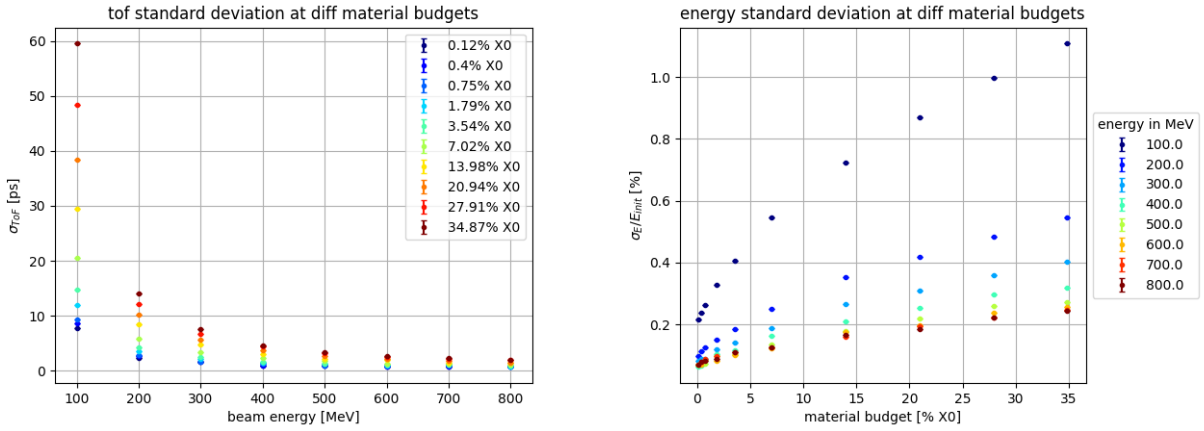

(a) **(b)**

Figure 65: a) ToF standard deviation (σ_{ToF}) and b) Energy standard deviation $\sigma(E)$ normalized to the beam energy E_{init} at different energies and material budgets for protons.

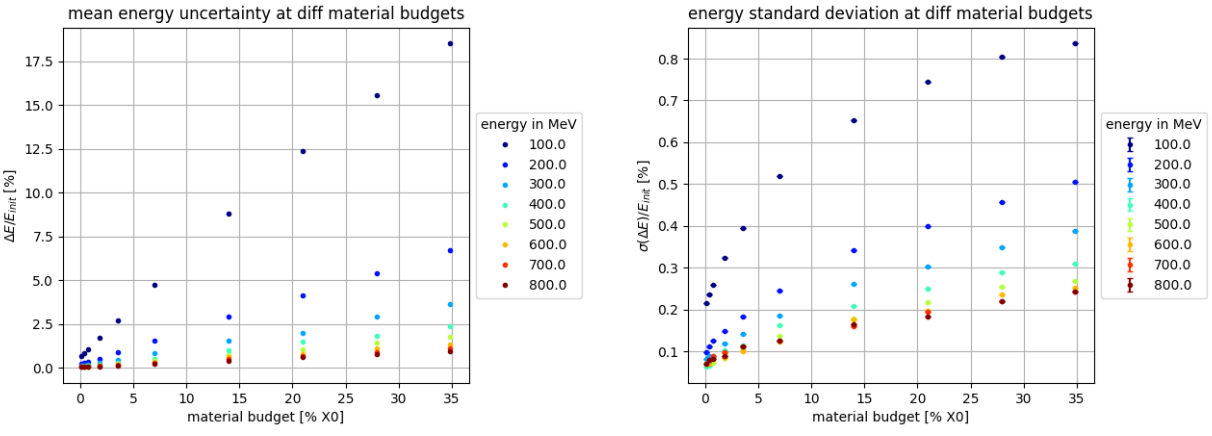

(a) **(b)**

Figure 66: a) Mean energy uncertainty ΔE for protons. b) Energy standard deviation $\sigma\left(\Delta E\right)$ for protons. Both plots are normalized to the beam energy E_{init}.

5.2.3 Material budget with protons and 30 ps time resolution

To obtain the value of the material budget on which the intrinsic time resolution of the scattering dominates over the custom time resolution, a blurring of the ToF distribution was made. The custom time resolution σ_t represents the capability of the electronic readout circuit's time resolution and the time resolution of the sensor in the simulation. It was assumed that a time resolution of 30 ps per detector plane can be achieved in a real experiment as was stated in [18].

In analogy to Sec. 5.2.2 for 0 ps, here, the standard deviation for a time resolution of 30 ps is shown in Fig. 67a. The $\sigma\left(ToF\right)$ is a combination of the intrinsic standard deviation of the scattering and the time resolution σ_t of 30 ps per plane. Further, an offset of 42 ps can be obtained, which is a product of the uncertainty propagation and the resulting factor of $\sqrt{2}$. As can be seen in Fig. 67a, the influence of the standard deviation on the energies ≤ 200 MeV are most affected while at 100 MeV the material budgets $> 3.5\,\%$ X0 show large deviations up to 73 ps.

The results of the energy standard deviation in Fig. 67b show that the effect of the custom time resolution (σ_t) of 30 ps per plane is more pronounced on particles with higher energy, because of their higher velocity and therefore a larger flight distance in the same period of time. Despite the results in Fig. 65b, the energy standard deviation for particles with higher energy is higher than for particles with lower energy in Fig. 67b. The time resolution σ_t also reveals the effect that with higher material budget the deposited energy within the material is higher and therefore the relative uncertainty is decreasing. As can be seen in Fig. 67b, this is not true for particles with 100 MeV, where the scattering still dominates the energy standard deviation.

The comparison of Fig. 66a and Fig. 68a shows that the blurring of the time resolution σ_t of 30 ps barely has an influence of the energy difference ΔE for particles with low energies. The dominance of the blurring of the time resolution can be seen in the results of the particles with higher energies, where the increase of ΔE with increasing material budget is suppressed. Although, the results show a higher value when compared to Fig. 66a because of the influence of the custom time resolution σ_t on the measuring of the mean ToF μ_{ToF}. Similar to Fig. 67b, the effect of an improvement of the relative energy standard deviation $\sigma\left(\Delta E\right)$, due to the decrease of the relative uncertainty with higher material budget can be seen in Fig. 68. Two effects contribute to the results at lower particle's energies: At lower material budgets, the effect of an increase of $\sigma\left(\Delta E\right)$, due to the increase of the scattering of the particles with higher material budget dominates. At material budgets $> 5\,\%$ X0 the influence of the increasing of the energy loss (higher ΔE) and a resulting decreasing of the relative energy standard deviation $\sigma\left(\Delta E\right)$ can be observed.

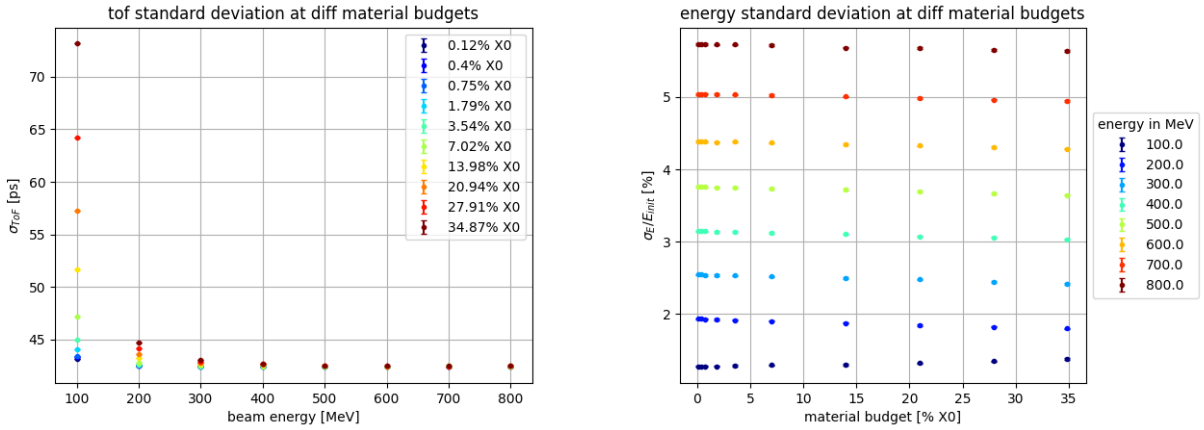

(a) (b)

Figure 67: a) ToF standard deviation $\sigma(ToF)$ at different energies and material budgets for protons. b) Energy standard deviation $\sigma(E)$ normalized to the beam energy E_{init} for protons.

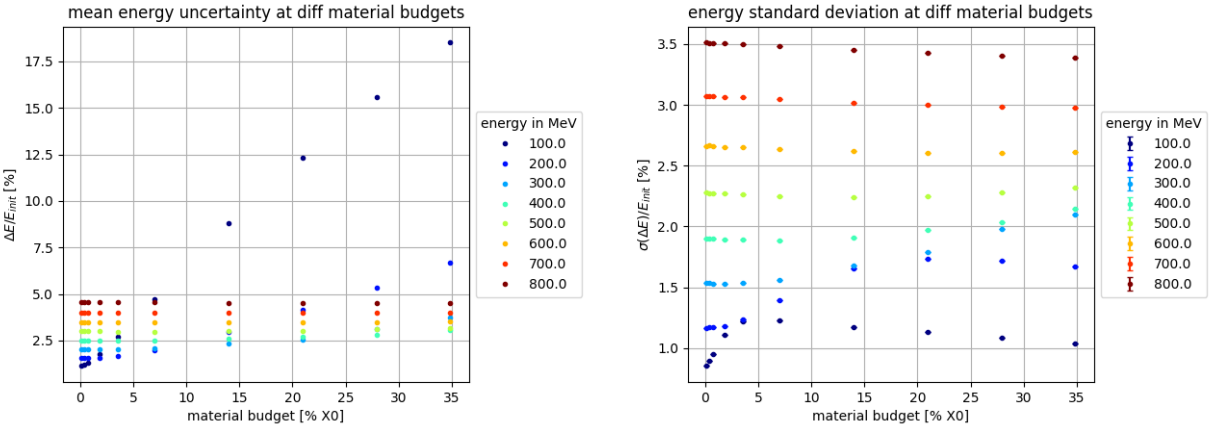

(a) (b)

Figure 68: a) Mean energy uncertainty ΔE for protons. b) Energy standard deviation $\sigma(\Delta E)$ for protons. Both plots are normalized to the beam energy E_{init}.

5.2.4 Material budget with protons, 50 ps and 100 ps time resolution

In this section, the time resolution was set to 50 ps and 100 ps, where the standard deviation of the ToF and the standard deviation of the energy collectively increase. When comparing Fig. 65a, Fig. 67a, Fig. 69a and Fig. 71a, it can be seen that the offset in terms of the custom time resolution reaches a higher level beyond the value of the time resolution that was set. For example, the offset in Fig. 69a is not just the 50 ps time resolution but rather 71 ps. This is because of the uncertainty propagation when dealing with 2 detector planes, each blurred with a time resolution σ_t, and the subsequent uncertainty propagation factor of $\sqrt{2}$. In Fig. 71a the 100 ps time resolution of both planes therefore raises the offset of the ToF standard deviation to values between 140 ps and 142 ps. Also, the range of the highest standard deviation value to the lowest decreases with higher time resolution.

The energy standard deviations in Fig. 69b, Fig. 71b slightly decreases with higher material budget, giving the intention that with higher material budget, the precision of the measured energy increases. In Fig. 70a and Fig. 72a the difference between the beam energy E_{init} and the measured mean energy $\mu(E)$ can be seen with the result that particles with lower energy loose more energy in thicker materials than particles with higher energies, where the difference is situated on a same level. The values of the energy standard deviation $\sigma\,(\Delta E)$ in Fig. 70b and Fig. 72b present a worsening of the precision with increasing custom time resolution σ_t.

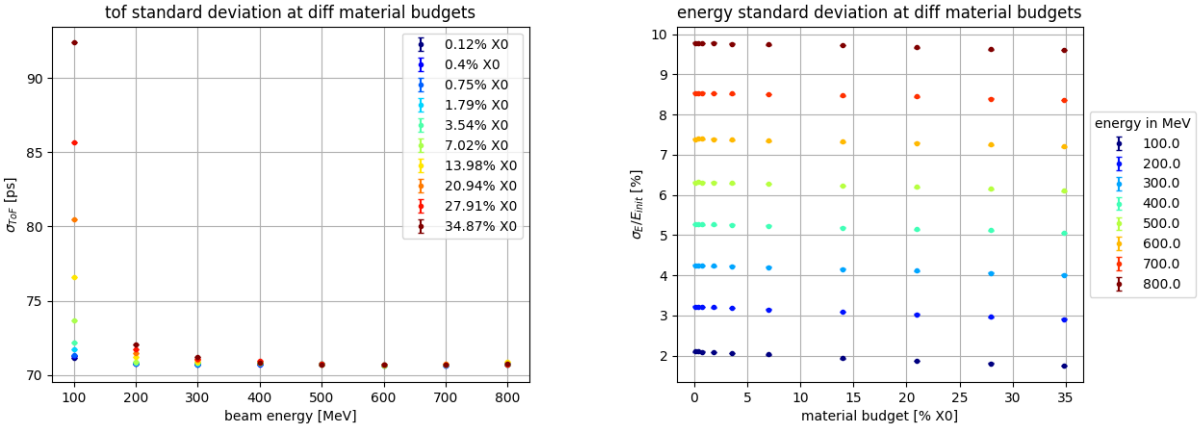

(a) (b)

Figure 69: a) ToF standard deviation $\sigma(ToF)$ at different energies and material budgets for protons. b) Energy standard deviation $\sigma(E)$ normalized to the mean energy $\mu(E)$ at different energies and material budgets. Both plots with 50 ps time resolution.

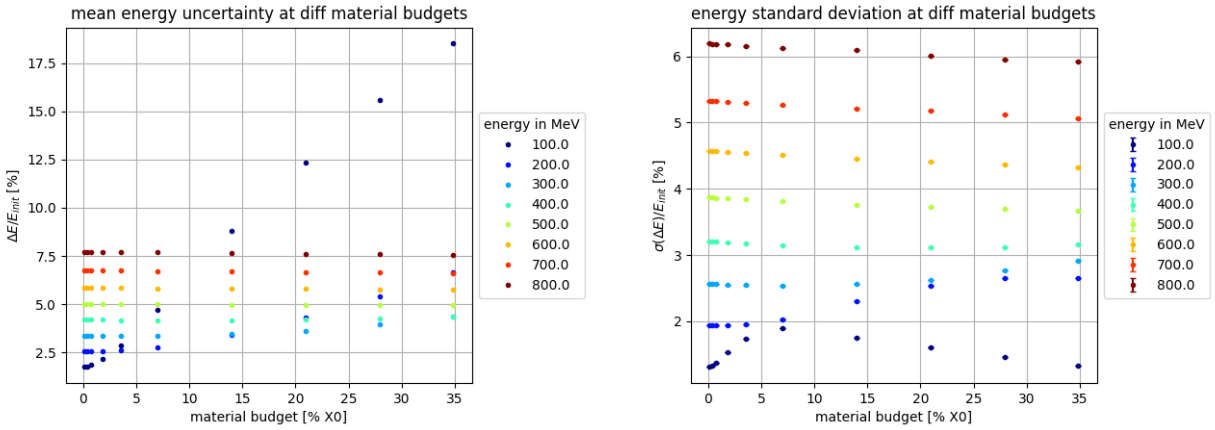

(a) **(b)**

Figure 70: a) Mean energy uncertainty ΔE for protons. b) Energy standard deviation $\sigma(\Delta E)$ for protons. Both plots are normalized to the beam energy E_{init} and with 50 ps time resolution.

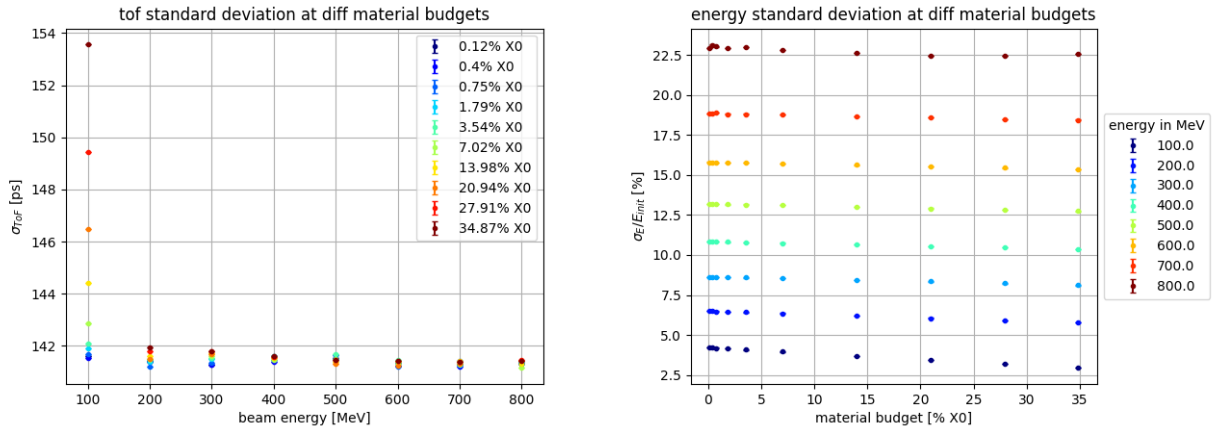

(a) **(b)**

Figure 71: a) ToF standard deviation $\sigma(ToF)$ at different energies and material budgets for protons. b) Energy standard deviation $\sigma(E)$ normalized to the mean energy $\mu(E)$ at different energies and material budgets. Both plots with 100 ps time resolution.

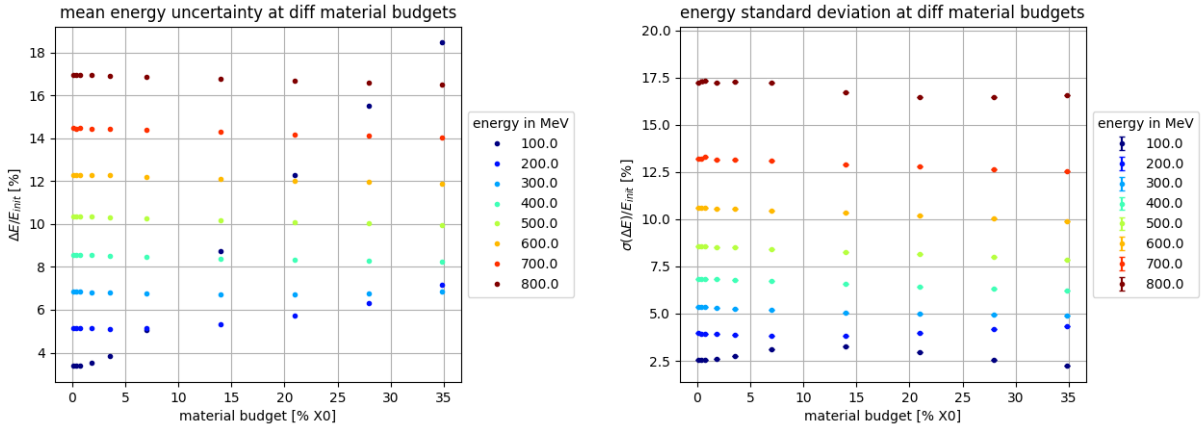

(a) **(b)**

Figure 72: a) Mean energy uncertainty ΔE for protons. b) Energy standard deviation $\sigma(\Delta E)$ for protons. Both plots are normalized to the beam energy E_{init} and with 100 ps time resolution.

5.2.5 Material budget with $^{12}C^{6+}$ carbon ions, 0 ps time resolution

Compared to the rest mass of protons ($\sim 938\,\text{MeV}$), the rest mass of $^{12}C^{6+}$ carbon ions with $\sim 11.175\,\text{GeV}$ is significantly higher. Thus, the deviation of the time-of-flight due to scattering is expected to be lower as with protons, according to Highland's formula [40]. This expectation is met and can be seen in Fig. 73a, where at 83.3 MeV/n and 7.02 % X0, the standard deviation takes a value of 10.6 ps (0.113 %). In comparison, the proton's values for 100 MeV and 7.02 % X0 can be obtained to be 20.1 ps. The energy standard deviation for 83.3 MeV/n and 7.02 % X0 is at 0.19 % (Fig. 73b) and the mean energy uncertainty ΔE is with 17.1 % (Fig. 74a) larger, compared to the ΔE of 4.9 % for protons (Fig. 66a). The energy standard deviation $\sigma(E)$ and the standard deviation of the energy difference $\sigma(\Delta E)$ are significantly lower for carbons and it can be concluded that the precision of determinating the energy of $^{12}C^{6+}$ is higher than with protons.

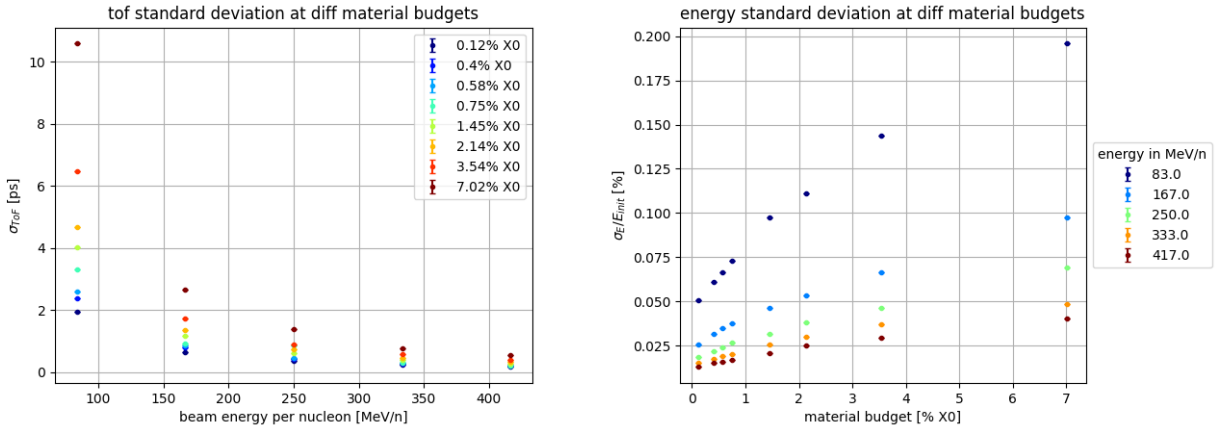

(a) (b)

Figure 73: a) ToF standard deviation $\sigma(ToF)$ for carbon. b) Energy standard deviation $\sigma(E)$ normalized to the beam energy E_{init} for carbon.

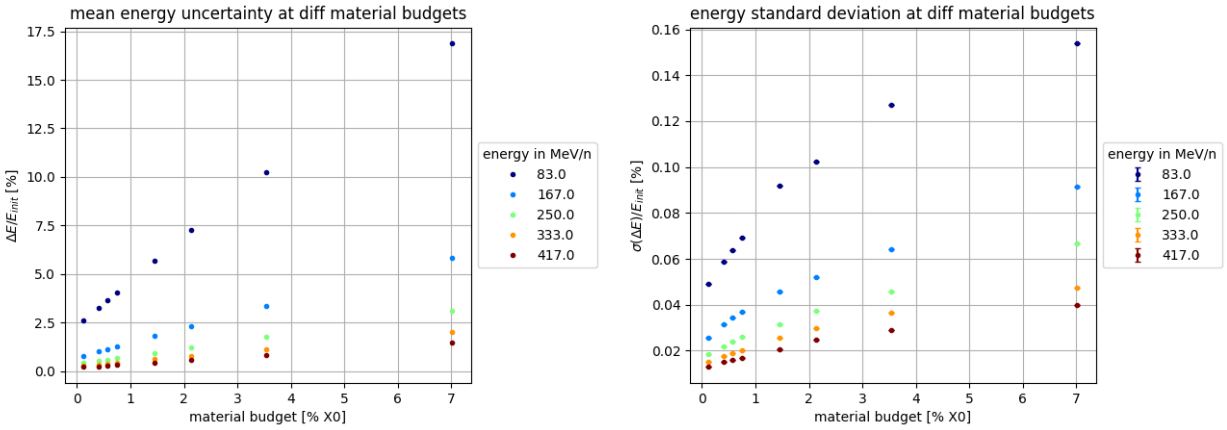

(a) (b)

Figure 74: a) Mean energy uncertainty ΔE for carbon. b) Energy standard deviation $\sigma(\Delta E)$ for carbon. Both plots normalized to the beam energy E_{init}.

5.2.6 Material budget with $^{12}C^{6+}$ carbon ions, 30 ps time resolution

For the ToF- and the energy plots in Fig. 75 and Fig. 76, the time resolution was blurred with 30 ps. The plots for carbons and protons are similar, when taken into account that the comparison is based on the energy per nucleon. The results for the energy difference's standard deviation $\sigma(\Delta E)$ in Fig. 76b show that with 83.3 MeV/n carbons, $\sigma(\Delta E)$ decreases and the results of 167.0 MeV/n carbons increase at lower material budget, but after a maximum at 3.54 % X0 takes a lower value at 7.02 % X0. For the 417.0 MeV/n-case the behaviour is inverted to that of 167.0 MeV/n, while the differences in the values are much smaller.

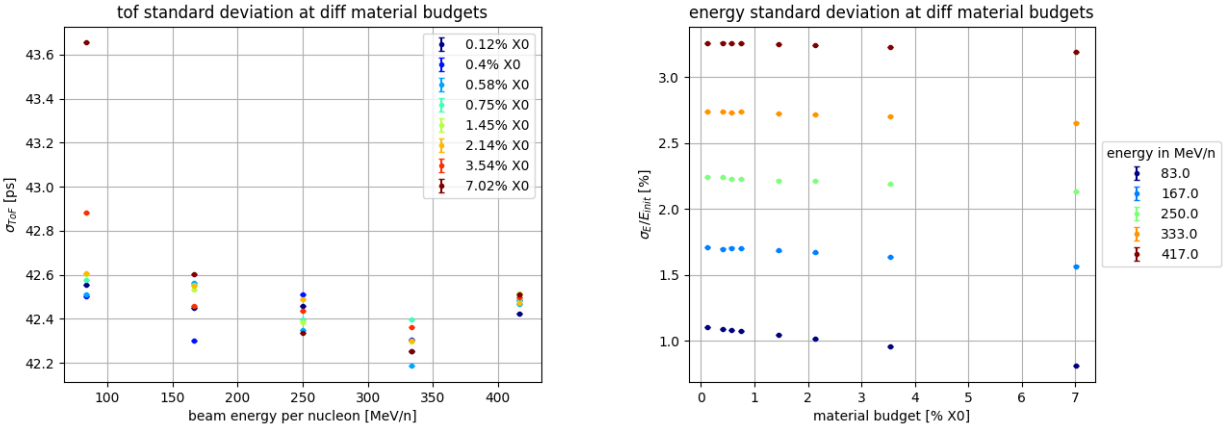

(a) (b)

Figure 75: a) ToF standard deviation $\sigma(ToF)$ at different energies and material budgets for carbon. b) Energy standard deviation $\sigma(E)$ normalized to the beam energy E_{init} at different energies and material budgets for carbon.

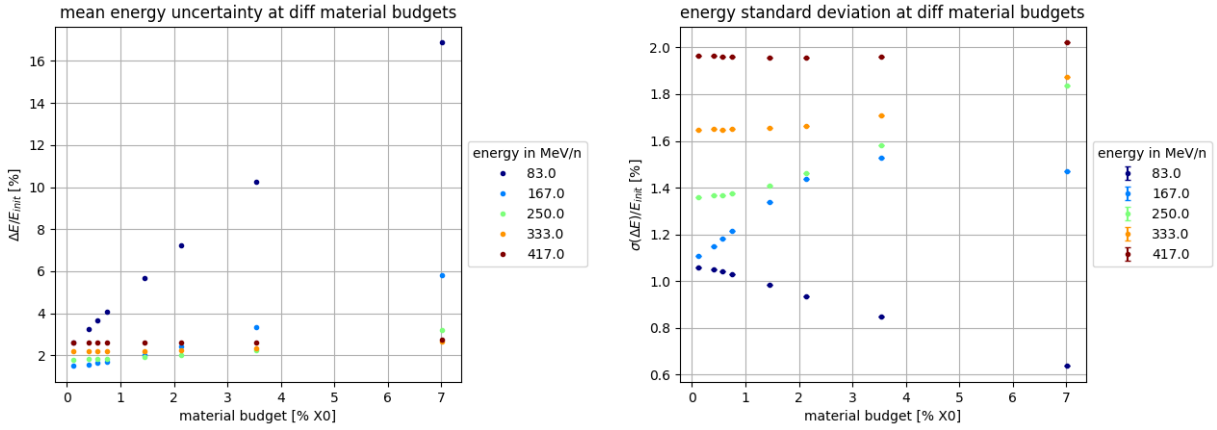

(a) (b)

Figure 76: a) Mean energy uncertainty ΔE for carbon. b) Energy standard deviation $\sigma(\Delta E)$ for carbon. Both plots are normalized to the beam energy E_{init}.

5.2.7 Material budget with helium ions, 0 ps time resolution

The alpha particle's rest mass with $\sim 3.727\,\mathrm{GeV}$ is four times higher than the proton's, but also three times smaller than the carbon ion. When comparing the result's plots of Fig. 77 with protons (Fig. 65), it can be seen that the ToF standard deviation as well as the energy standard deviation show lower values and therefore give better results. Despite these findings, $^{12}C^{6+}$ carbon ions show a slightly better performance in terms of ToF- and energy standard deviation as can be obtained from Fig. 77 and Fig. 73. While the mean energy uncertainty ΔE in Fig. 78a is similar to the values of protons (Fig. 66a), both, the energy standard deviation $\sigma(E)$ (Fig. 77b) and the standard deviation of the mean energy uncertainty $\sigma(\Delta E)$ (Fig. 78b) show better results, only passed by the performance of $^{12}C^{6+}$ carbon ions (Fig. 73b and Fig. 74b).

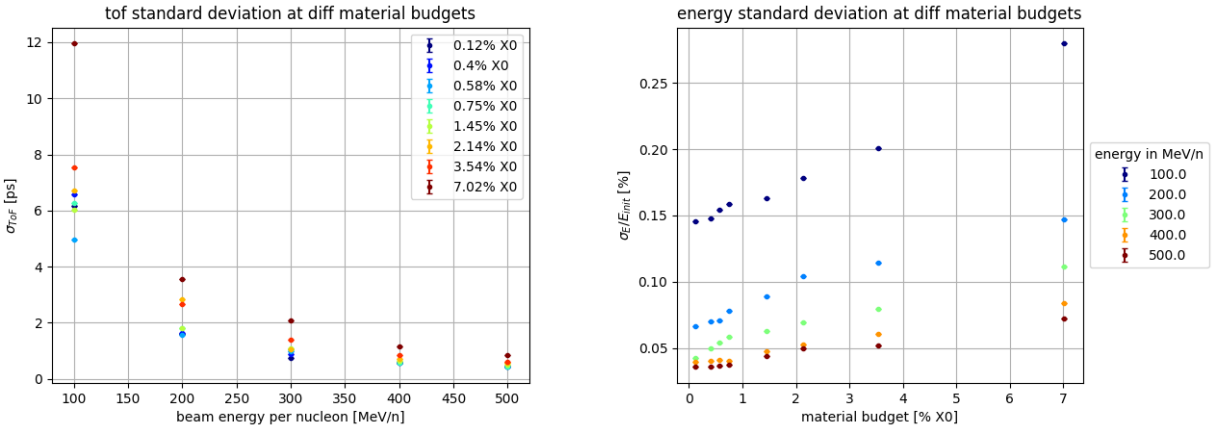

(a) (b)

Figure 77: a) ToF standard deviation $\sigma(ToF)$ for helium ions. b) Energy standard deviation $\sigma(E)$ normalized to the beam energy E_{init} for helium ions.

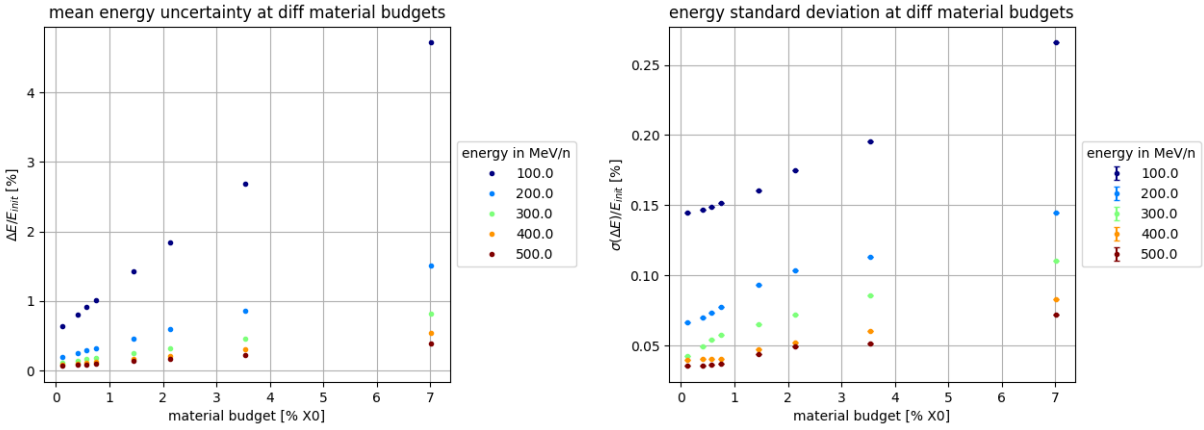

(a) (b)

Figure 78: a) Mean energy uncertainty ΔE for helium ions. b) Energy standard deviation $\sigma(\Delta E)$ for helium ions. Both plots are normalized to the beam energy E_{init}.

5.2.8 Material budget with helium ions, 30 ps time resolution

The ToF- and the energy standard deviation of helium ions at 30 ps time resolution are similar to the results obtained by $^{12}C^{6+}$ carbon ions, as can be seen in Fig. 79. The results of the mean energy uncertainty ΔE shown in Fig. 80a are identical to the ones obtained with protons (Fig. 68a), but especially the results of lower particle's energies differ from the $^{12}C^{6+}$ carbon ions. In Fig. 80b the precision of the energy difference distribution $\sigma(\Delta E)$ is presented and similar to Fig. 76b the 100 MeV/n results show an increase until a maximum at 3.54 % X0 and a slight decrease afterwards. The $\sigma(\Delta E)$ for 200 MeV/n increases steadily with increasing material budget and with higher energy the results become decreasing with higher material budget.

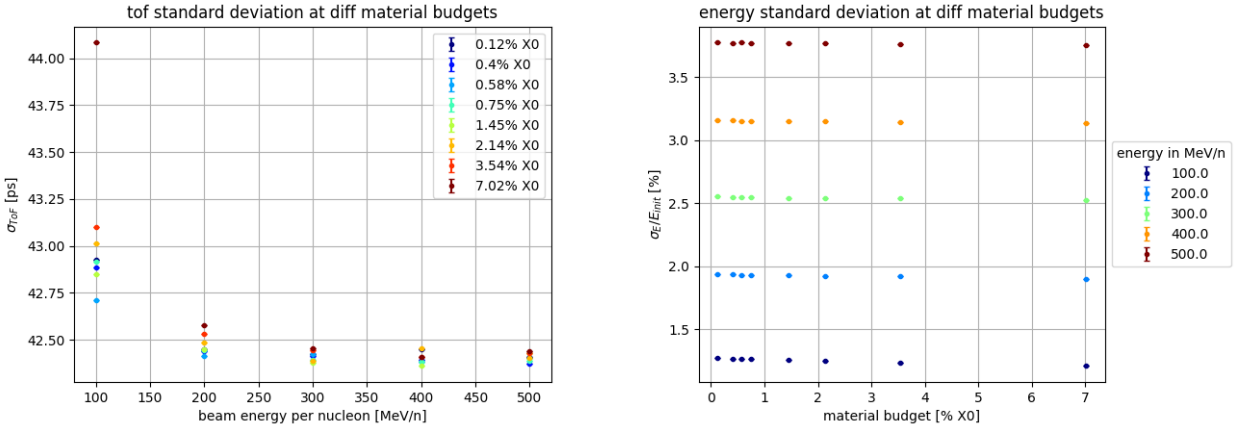

(a) **(b)**

Figure 79: a) ToF standard deviation $\sigma(ToF)$ for helium ions. b) Energy standard deviation $\sigma(E)$ normalized to the beam energy E_{init} for helium ions.

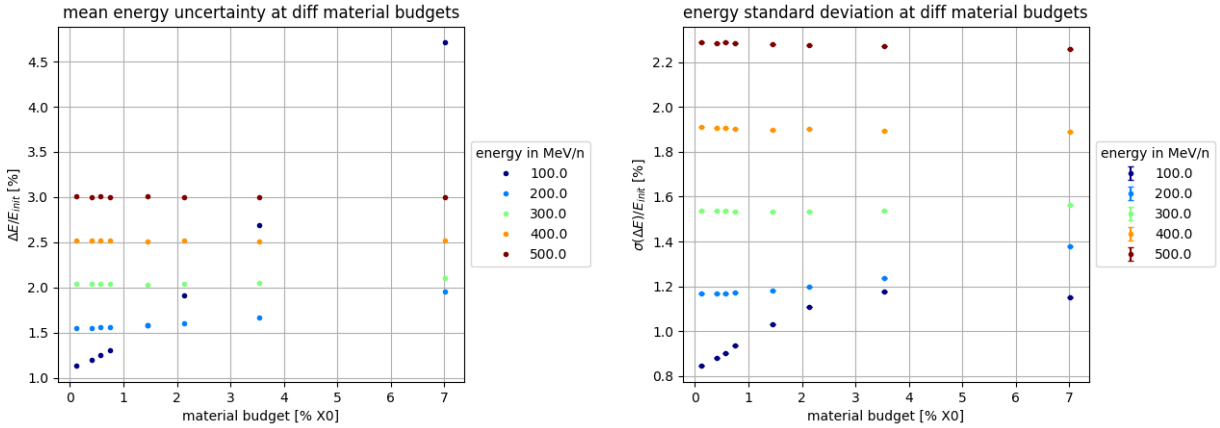

(a) **(b)**

Figure 80: a) Mean energy uncertainty ΔE for helium ions. b) Energy standard deviation $\sigma(\Delta E)$ for helium ions. Both plots are normalized to the beam energy E_{init}.

5.2.9 Spatial resolution

In the previous section, the assumption was made that the flight path of the particles could be determined with optional precision. In reality, the detectors does not show a detection efficiency of 100 % on their sensitive area and also have to be arranged in an array where dead areas are inevitable, leaving particles undetected. This situation is concerned in the simulation with the variables named σ_x and σ_y and refer to the spatial resolution in x- and y-direction on the detector's surface. In the analysis program written in Python, where the data from the simulations are analyzed, the particle hits on the detectors are blurred with a Gauss distribution, where the spatial resolution is its standard deviation. These hits are the basis for the calculation of the tracks of the particles and their pathlength to obtain the velocity and furthermore, the energy of the particles (Sec. 2.2).

The following results present the standard deviation of the energy and the energy uncertainties depending on the spatial resolution at different material budgets and to focus on the effects of the spatial resolution only, the time resolution σ_t was set to 0 ps. Fig. 81 and Fig. 82 shows a wide range of spatial resolutions, where the energy standard deviation $\sigma(E)$ and the mean uncertainty $\Delta(E)$ remain on a similar level, though in Fig. 81, the energy standard deviation seems to improve at spatial resolutions > 10 mm. This effect of an apparent increase on the accuracy with 100 MeV protons originates from an increase of the time-of-flight due to the energy loss and also the time-of-flight distance increases because of the higher spatial resolution.

When using Eq. 2.15 for evaluating the velocity, the uncertainty decreases due to the introduced uncertainties in the time and distance. Compared to Fig. 82b, where 800 MeV protons were used, it can be seen that the energy uncertainties increase and the energy resolution departs from the other values at a spatial resolution > 10 mm. This is also valid for the energy standard deviation $\sigma(\Delta E)$ in Fig. 83, showing how precise the energy uncertainty can be obtained.

Fig. 84 and Fig. 85 show the energy standard deviation and the energy uncertainty diagrams at a ToF distance of 10 cm and present a deterioration of the resolution and uncertainty at spatial resolutions > 2 mm. Though, according to Fig. 56a, the time resolution of a ToF distance of 10 cm show intrinsic uncertainties, it can be clearly seen in Fig. 84, Fig. 85 and Fig. 86 that there is a deviation on the values at > 2 mm spatial resolution.

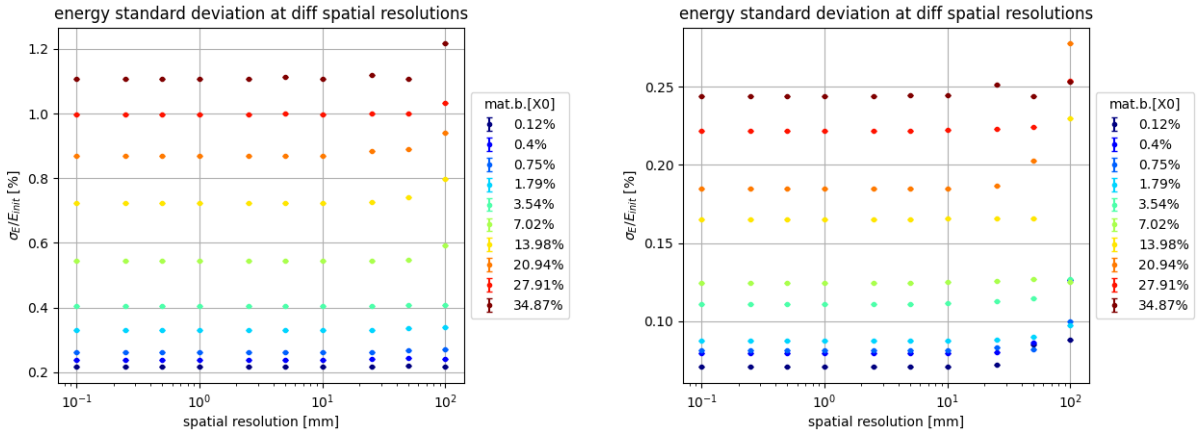

(a) **(b)**

Figure 81: Energy standard deviation $\sigma(E)$ at different spatial resolutions, normalization to the beam energy E_{init} with a ToF distance of 1 m and 1 Mio. protons. a) 100 MeV b) 800 MeV.

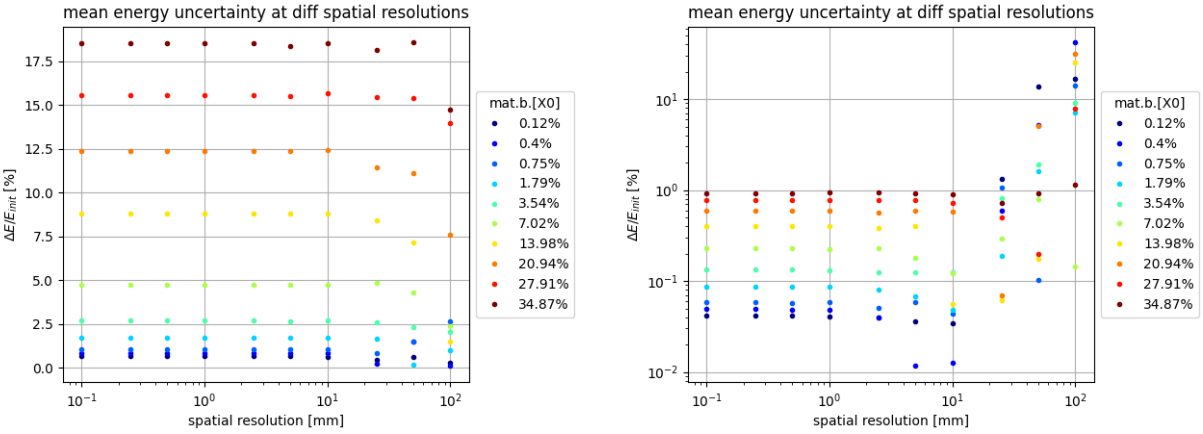

(a) **(b)**

Figure 82: Mean energy uncertainty ΔE at different spatial resolutions, normalization to the beam energy E_{init} with a ToF distance of 1 m and 1 Mio. protons. a) 100 MeV b) 800 MeV.

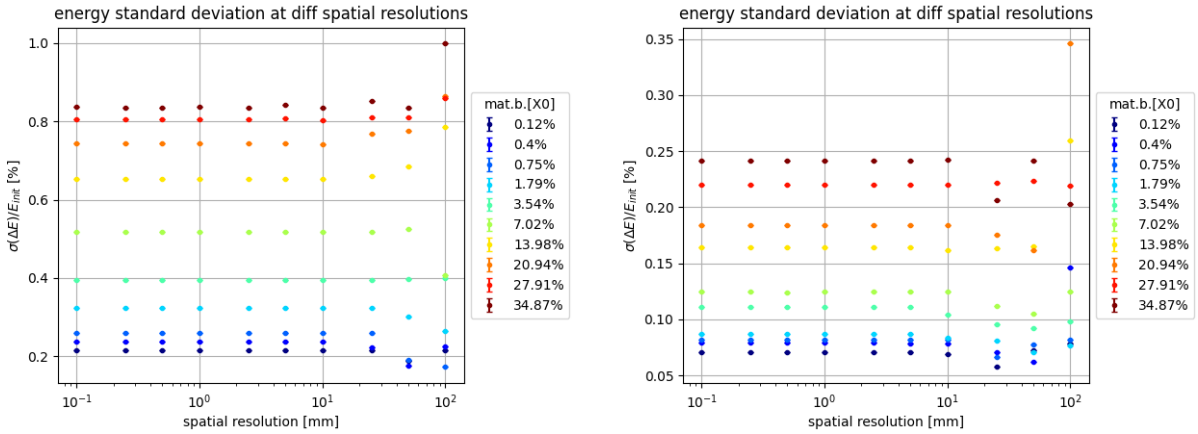

(a) **(b)**

Figure 83: Energy standard deviation $\sigma\,(\Delta E)$ at different spatial resolutions, normalization to the beam energy E_{init} with a ToF distance of 1 m and 1 Mio. protons. a) 100 MeV b) 800 MeV.

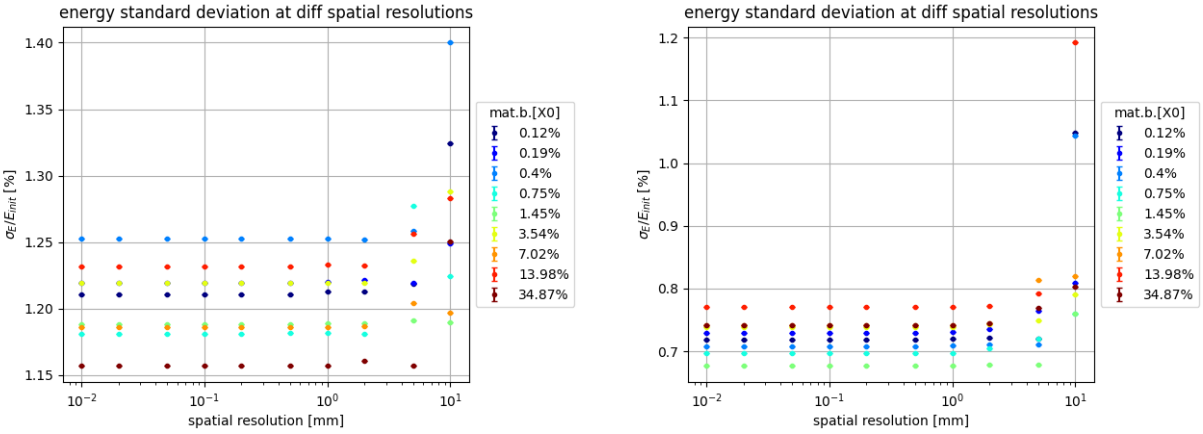

(a) **(b)**

Figure 84: Energy standard deviation $\sigma(E)$ at different spatial resolutions, normalization to the beam energy E_{init} with a ToF distance of 10 cm and 1 Mio. protons. a) 100 MeV b) 800 MeV.

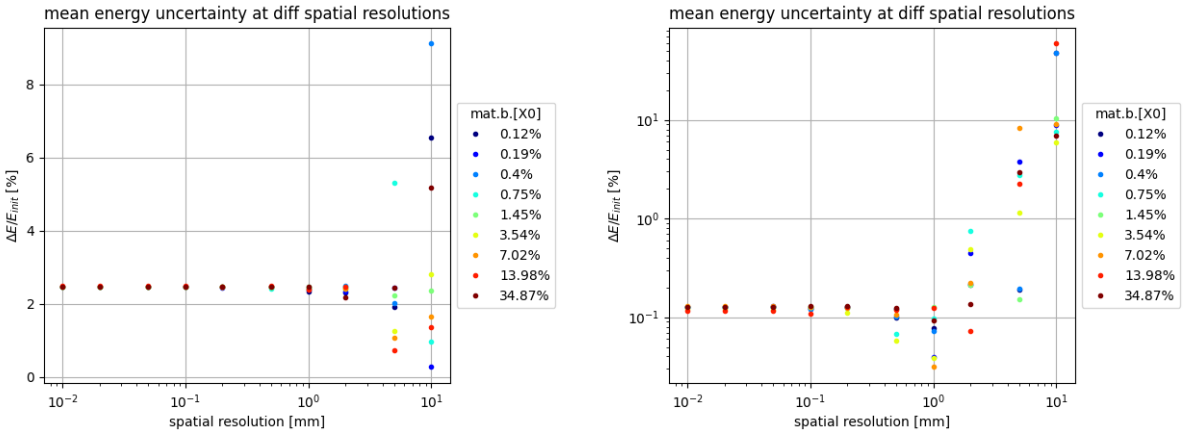

(a) **(b)**

Figure 85: Mean energy uncertainty ΔE at different spatial resolutions, normalization to the beam energy E_{init} with a ToF distance of 10 cm and 1 Mio. protons. a) 100 MeV b) 800 MeV.

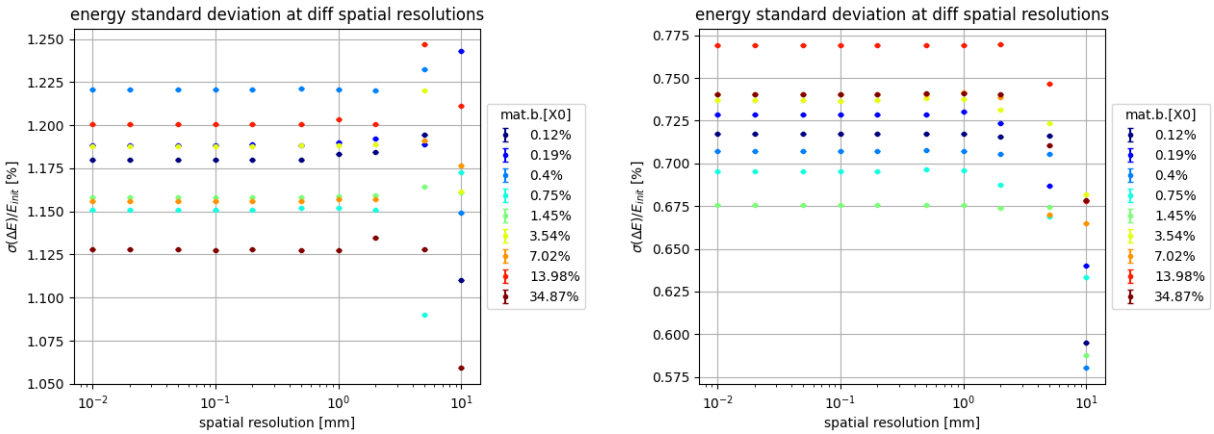

(a) **(b)**

Figure 86: Energy standard deviation $\sigma(\Delta E)$ at different spatial resolutions, normalization to the beam energy E_{init} with a ToF distance of 10 cm and 1 Mio. protons. a) 100 MeV b) 800 MeV.

5.2.10 LGAD size and beam spot size

Due to scattering of the beam when hitting the first LGAD, the detection of particles depend on the size of the second LGAD and the initial beam spot size. Therefore, the sensitive area of the second LGAD in the setup was varied and the number of detected particles was recorded. The ToF distance was left unchanged to 1 m and the material budget setting of the LGADs corresponded to the specifications of their physical pendants (Sec. 3.3.2). In order to study the isolated effect of the scattering and the beam broadening, the time- as well as the spatial resolution was set to 0 ps. Also, the initial beam spotsize was set to 2×2 mm and 8×8 mm, giving another parameter for an increase of the particle distribution at the second LGAD. It is assumed that the active area is covered by pixel detectors with a detection effiency of 100% and a spatial resolution of 0 µm. The values written in the legend in the following plots are the side length of a square pad detector.

The beam spot size in Fig. 87a has the dimension of 2×2 mm and the percentage of the protons detected deviates the most for energies ≤ 150 MeV, while at beam energies ≥ 200 MeV, $> 80\%$ of the particles were detected with an LGAD of size 20 mm. Fig. 87b shows a difference to that behavior, because the beam spot size is with 8×8 mm bigger than the previous one. Here, the deviation of the detected particles spreads over a wide range of energies and LGAD sizes. For the detection of $> 80\%$ of the protons, referenced in the previous example an LGAD size of at least 35 mm is needed for energies ≥ 200 MeV.

With a detector size of 25 mm, the number of detected $^{12}C^{6+}$ carbon ions is $> 80\%$ over the whole energy range in Fig. 88a with a spot size of 2×2 mm. The requirement for detecting $> 80\%$ of the $^{12}C^{6+}$ carbon ions, with a spot size of 8×8 mm in the whole range of energies in Fig. 88b is significantly higher with 35 mm than with the 2×2 mm beam spotsize. This can be explained with the higher rest mass of the $^{12}C^{6+}$ carbon ions (~ 11.175 GeV) compared to the rest mass of protons (~ 938 MeV) and the lower possibility to undergo scattering interactions or rather the finding, that the scattering angle is not as high as with protons. This is also true for helium ions as can be seen in Fig. 89, where the rest mass for an alpha particle is ~ 3.727 GeV. For scattered alpha particles, the detection efficiency is situated between the proton's and carbon ion's efficiencies.

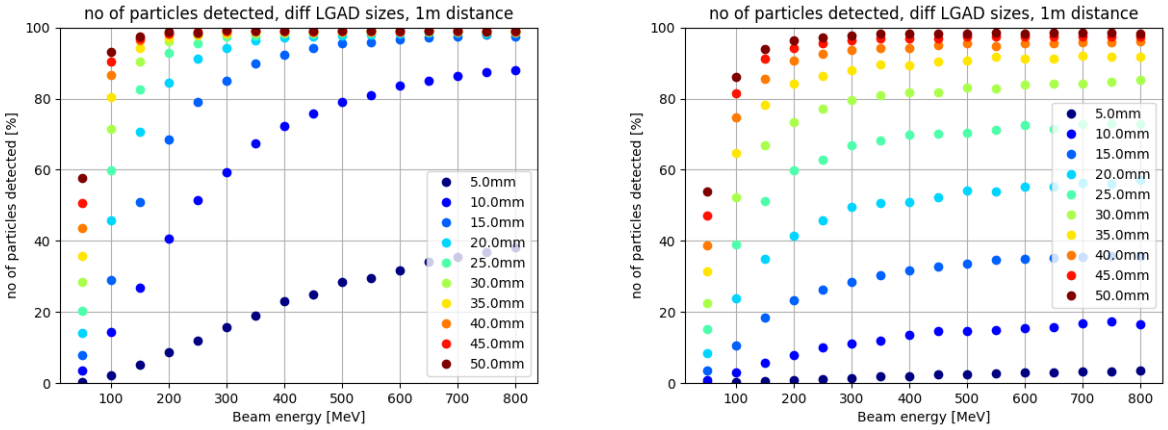

(a) **(b)**

Figure 87: a) Percentage of protons detected at different LGAD sizes and a beam spotsize of a) $2 \times 2\,\text{mm}$ and b) $8 \times 8\,\text{mm}$

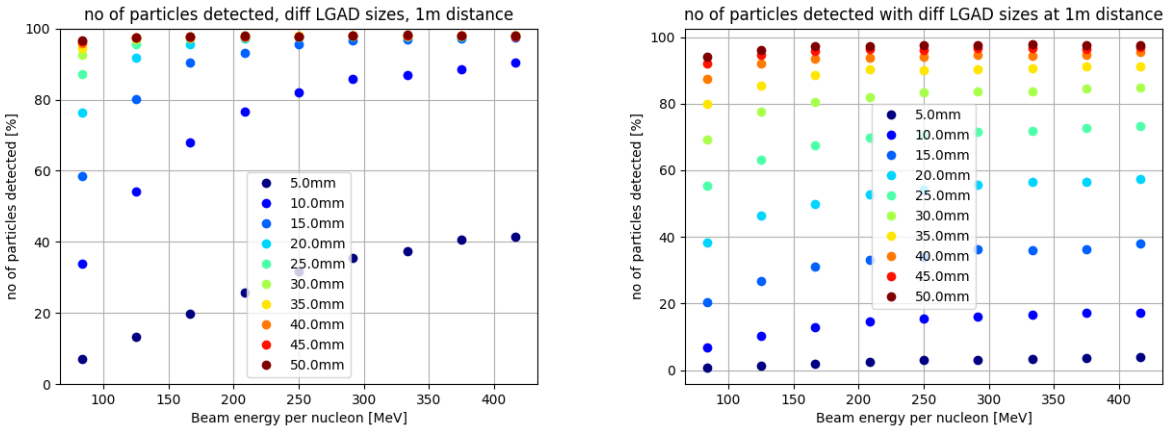

(a) **(b)**

Figure 88: a) Percentage of $^{12}C^{6+}$ carbon ions detected at different LGAD sizes and a beam spotsize of a) $2 \times 2\,\text{mm}$ and b) $8 \times 8\,\text{mm}$

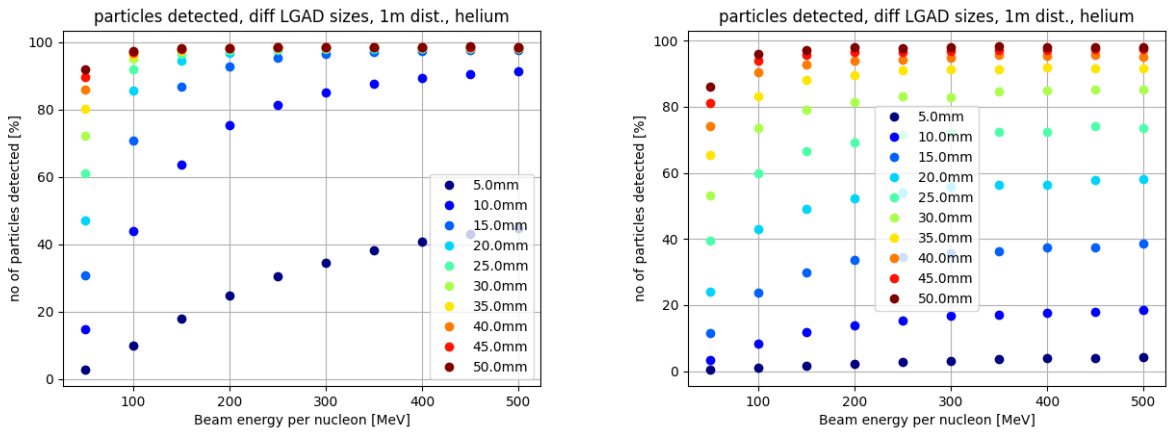

(a) **(b)**

Figure 89: Percentage of helium ions detected at different LGAD sizes and a beam spotsize of a) $2 \times 2\,\text{mm}$ and b) $8 \times 8\,\text{mm}$

5.2.11 ToF setup with 2x2 planes

Due to the quadratical add up of the standard deviations of the time-of-flight, an improvement of factor $\sqrt{2}$ in time resolution could theoretically be achieved when 4 LGAD planes instead of 2 are used in the ToF-setup. Another improvement of using the 2×2 - setup is an increase in the detection efficiency due to 2 detector layers. In this section, the results of a simulation setup with 4 planes is presented, where in Fig. 90, an overview can be seen. The sensitive area of the detectors is $1\,\mathrm{m} \times 1\,\mathrm{m}$ and the distance between a detector pair is 2 mm. The distance of 2 mm was chosen to exclude an introduction of uncertainties in time measurement between the detectors of a pair that would appear with longer distances, where the two time stamps would not be integrated in the formula in an equivalent manner. Therefore, the equation Eq. 5.2 can be used without the need for complex iterative methods and error propagation calculations. Another reason for the chosen 2 mm is the prevention of a volume overlap that might occur in the material budget simulations, where the thickness of the Cu layer is varied. For example, the effective distance between the detector pairs is 1.75 mm at a material budget of 0.1 % X0 and 0.85 mm for 7.0 % X0. In any case, the ToF distance is constantly at 1 m, where the two projection areas are situated exactly between the two detector pairs. In the Python analysis program, a straight line fit is made out of the four points that were recorded, when a particle hits the detectors.

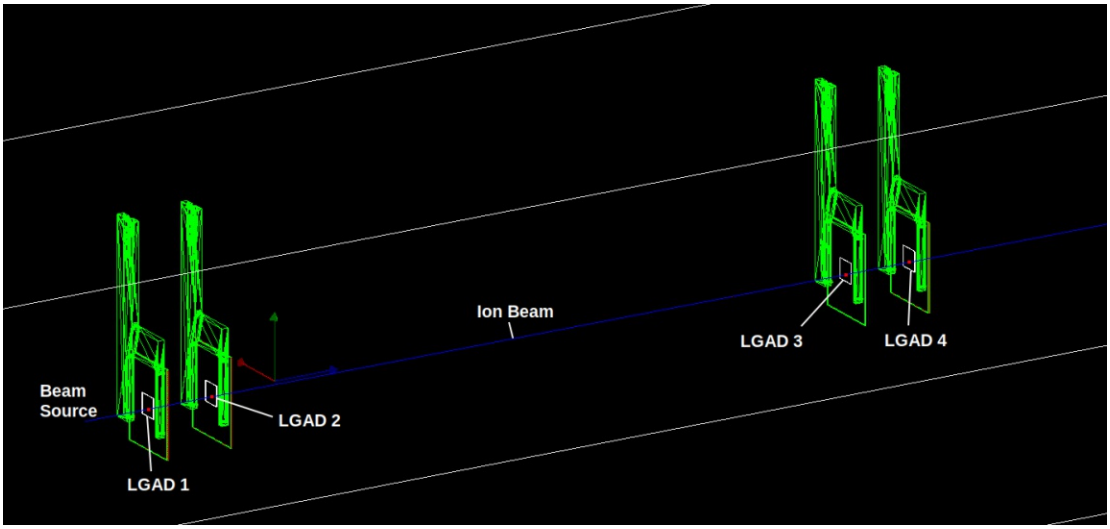

Figure 90: Visualization of the ToF setup with the 2×2 LGAD planes in Geant4. LGAD 1 and 2 as well as LGAD 3 and 4 are < 2 mm apart. Distance between LGAD 1 and 3: 100 cm. Note: the figure is not drawn to scale, the exact specifications appear in the text.

With 4 planes, the time-of-flight is calculated as follows:

$$ToF = \frac{1}{2}\left[(t_3 + t_4) - (t_1 + t_2)\right] \tag{5.2}$$

The ToF again yields to a Gaussian distribution with mean μ and std. dev. σ and can also be blurred with σ_t and spatial resolution σ_x, σ_y as described in Sec. 3.7.

5.2.12 Material Budget with 2x2 planes and protons

The results of the 2×2 - plane setup are characterised by the theoretical improvement of the standard deviation of the ToF and the scattering, which has a higher effect than with the 2×1 - setup, due to the higher material budget. When comparing Fig. 91a with the results of the 2×1 - setup (Fig. 65a), it can be concluded that the scattering effects dominate over the $\sqrt{2}$ - improvement. This scheme can also be seen in Fig. 91b, where the trend of the results is similar to the one shown in Fig. 65b, but with higher values over the whole energy- and material budget range, due to the distinct effect of scattering with 4 planes. This effect also led to an increase of the mean energy uncertainty (Fig. 92a) and the associated standard deviation (Fig. 92b) compared to the 2×1 - setup.

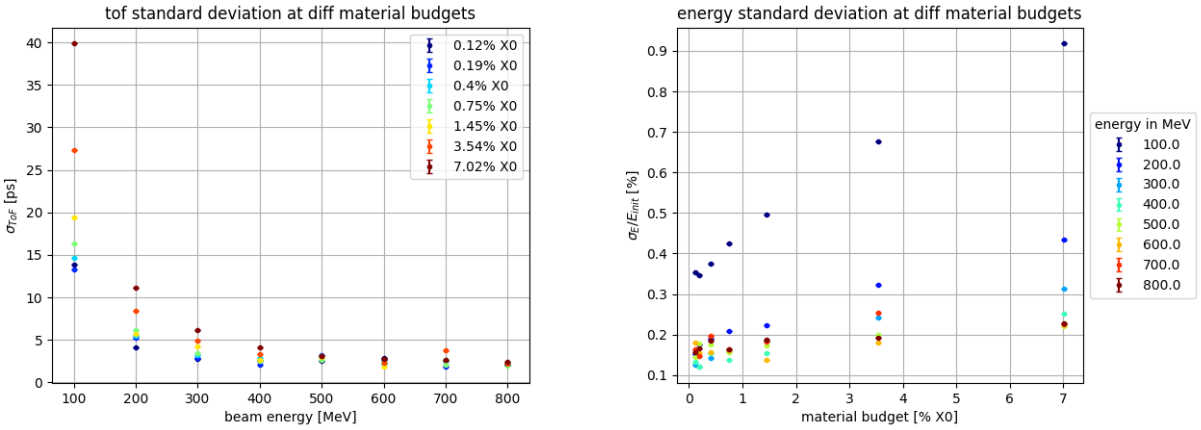

(a) (b)

Figure 91: a) ToF standard deviation $\sigma(ToF)$ at different energies and material budgets for protons. b) Energy standard deviation $\sigma(E)$ normalized to the beam energy E_{init} at different energies and material budgets for protons.

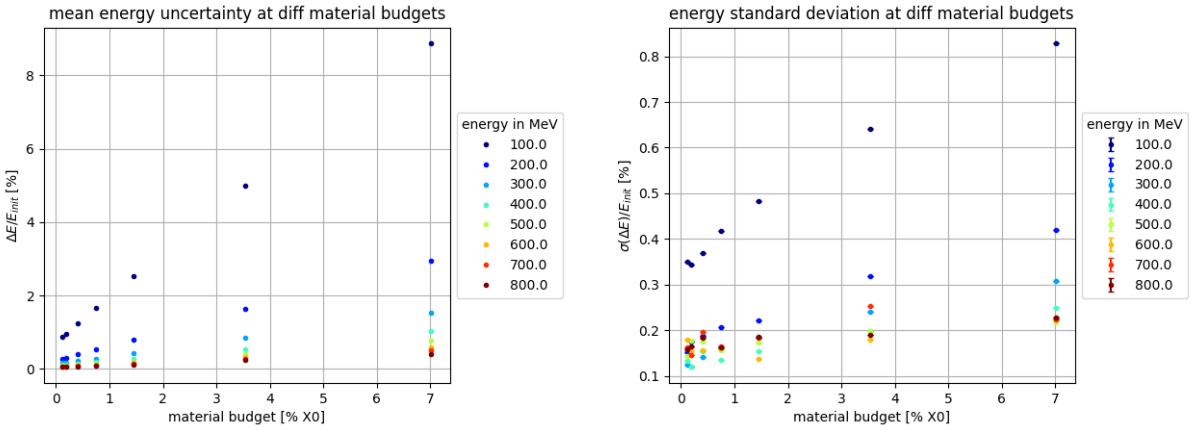

(a) (b)

Figure 92: a) Mean energy uncertainty ΔE for protons. b) Energy standard deviation $\sigma(\Delta E)$ for protons. Both plots are normalized to the beam energy E_{init}.

5.2.13 Material Budget with 2x2 planes, protons and 30 ps time resolution

When comparing Fig. 93a with Fig. 67a, it can be concluded that the scattering effects still dominate in an energy range of ≤ 200 MeV. At energies > 200 MeV, it can be seen that only the "propagation of uncertainty"- effect is visible, because the values of the 2×2 - setup with ~ 30 ps are smaller by the factor $\sqrt{2}$ compared to the 2×1 - setup with ~ 42.5 ps. The factor $\sqrt{2}$ can also be recognised in Fig. 93b and Fig. 94, except the values of the 100 MeV and 200 MeV particles deviate from that dependence because of the higher scattering compared to the 2×1 - setup.

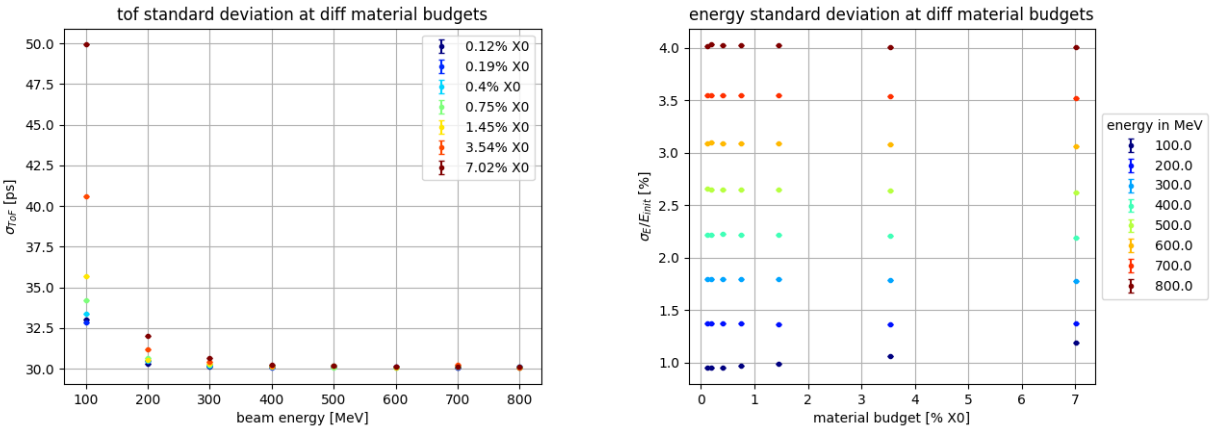

(a) (b)

Figure 93: a) ToF standard deviation $\sigma(ToF)$ at different energies and material budgets for protons. b) Energy standard deviation $\sigma(E)$ normalized to the beam energy E_{init} at different energies and material budgets for protons.

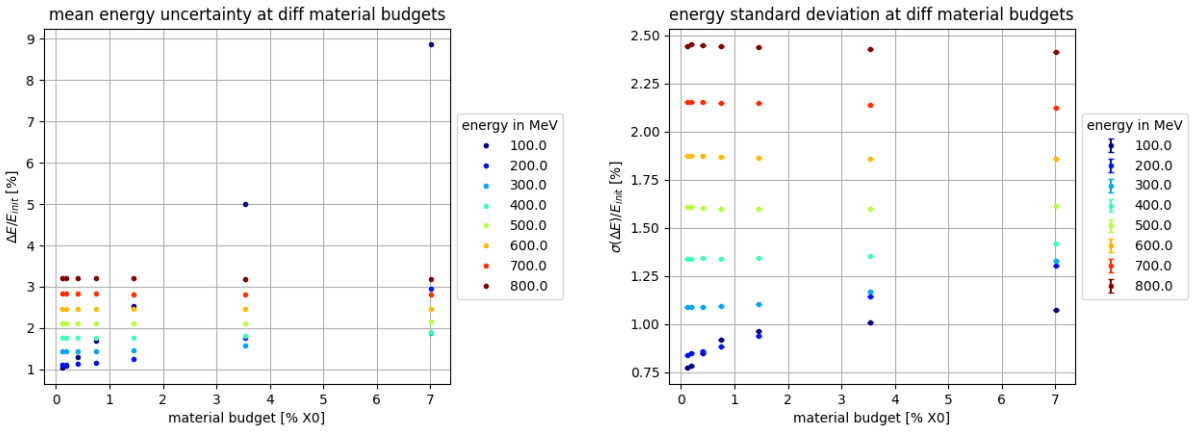

(a) (b)

Figure 94: a) Mean energy uncertainty ΔE for protons. b) Energy standard deviation $\sigma(\Delta E)$ for protons. Both plots are normalized to the beam energy E_{init}.

5.2.14 Material budget with 2x2 planes, $^{12}C^{6+}$ carbon ions and 0 ps time resolution

Fig. 95 and Fig. 96 present the standard deviation of the ToF $\sigma(ToF)$ and the energy $\sigma(E)$, as well as the mean energy uncertainty ΔE and the associated standard deviation $\sigma(\Delta E)$ for $^{12}C^{6+}$ carbon ions in the 2×2 - planes setup with 0 ps time resolution. Compared to the results of the 2×1 - planes setup, the scattering effects are visible as the dominant factor in the values, because the values of the results are significantly higher for all of the 4 plots.

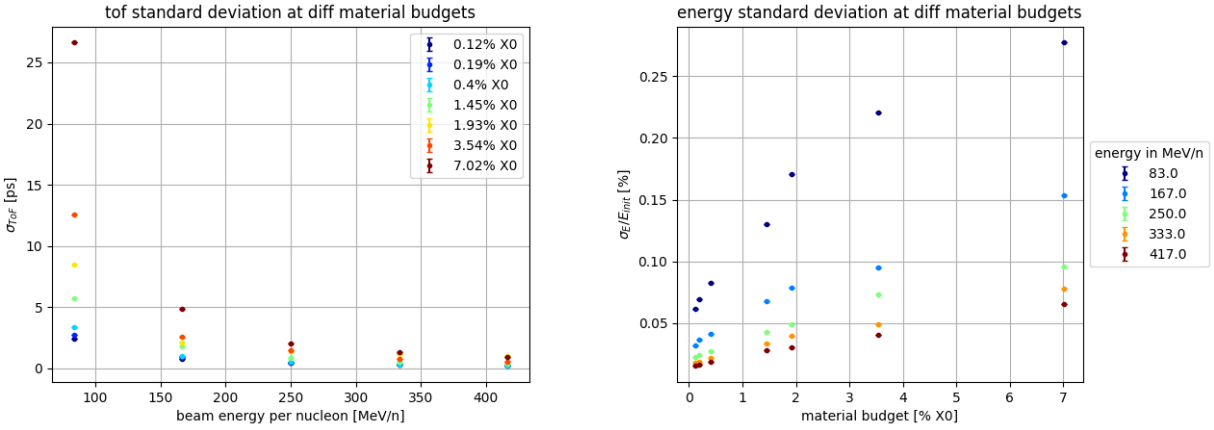

(a) (b)

Figure 95: a) ToF standard deviation $\sigma(ToF)$ at different energies and material budgets for carbon. b) Energy standard deviation $\sigma(E)$ normalized to the beam energy E_{init} at different energies and material budgets for carbon.

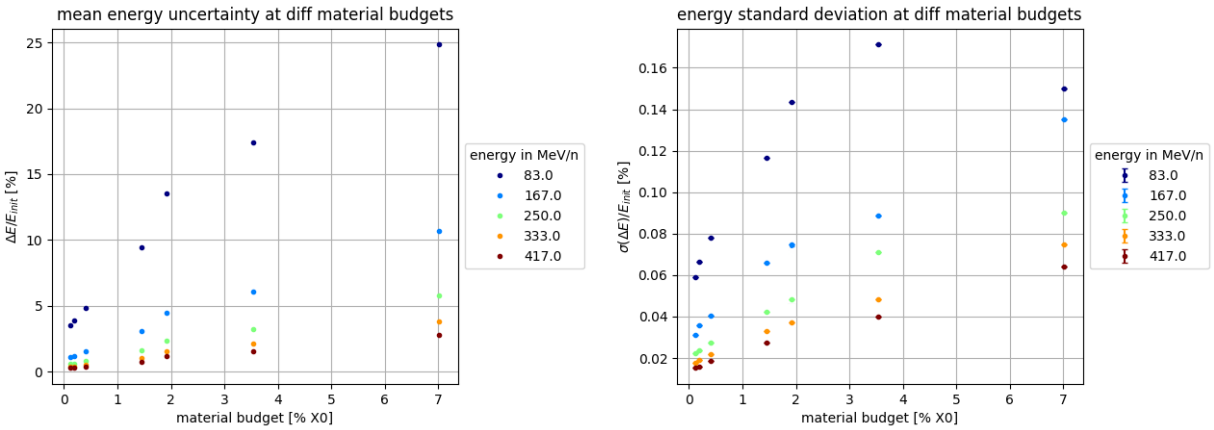

(a) (b)

Figure 96: a) Energy standard deviation $\sigma(E)$ at different energies and material budgets for carbon. b) Mean energy uncertainty ΔE for carbon. Both plots are normalized to the beam energy E_{init}.

5.2.15 Material budget with 2x2 planes, $^{12}C^{6+}$ carbon ions and 30 ps time resolution

As expected from the previous 2×2 - planes simulations, the results presented in Fig. 97a and Fig. 97b, where $^{12}C^{6+}$ carbon ions were used at a 30 ps time resolution, are increased by the factor $\sqrt{2}$ compared to the 2×1 - setup. In Fig. 98a, it can be seen that the mean energy uncertainty ΔE shows higher values than in the 2×1 - setup, but they can be obtained more precisely, because the standard deviation $\sigma(\Delta E)$ has significantly improved when using 4 planes (Fig. 98b).

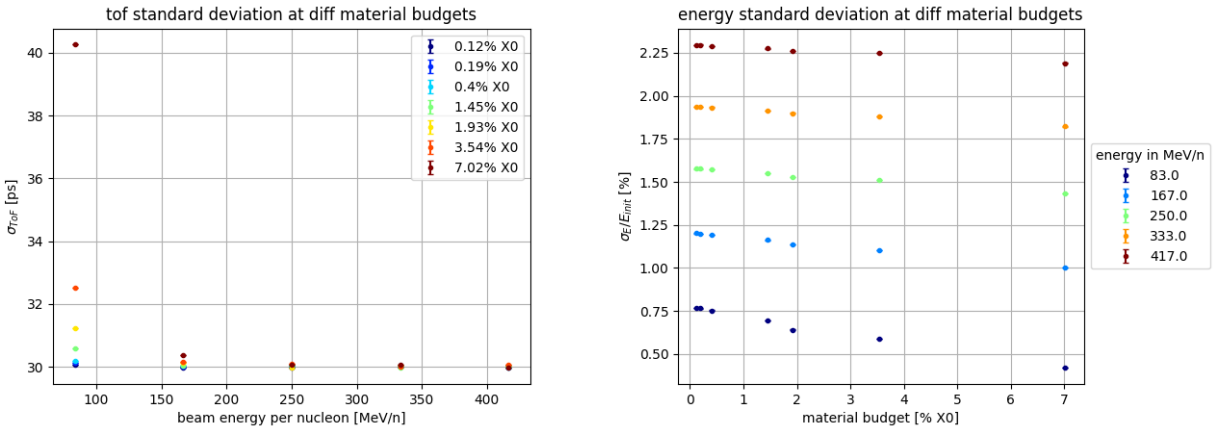

(a) (b)

Figure 97: a) ToF standard deviation $\sigma(ToF)$ at different energies and material budgets for carbon. b) Energy standard deviation $\sigma(E)$ normalized to the beam energy E_{init} at different energies and material budgets for carbon.

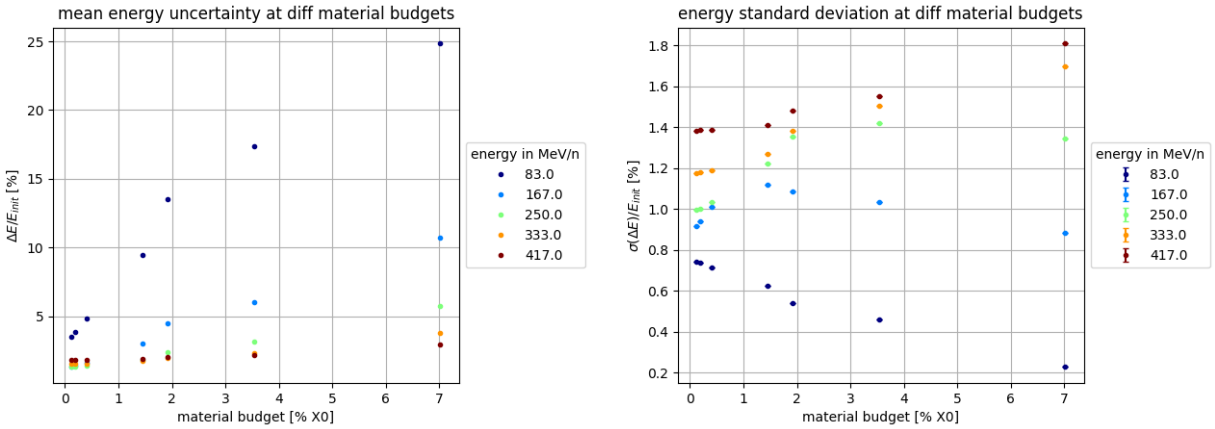

(a) (b)

Figure 98: a) Mean energy uncertainty ΔE for carbon. b) Energy standard deviation $\sigma(\Delta E)$ for carbon. Both plots are normalized to the beam energy E_{init}.

5.2.16 Material budget with 2x2 planes, helium ions, 0 ps time resolution

Also, the simulation with helium ions (alpha particles) draws a similar picture of what was expected and already discussed in the proton and carbon ion case: The scattering dominates in all of the observed results when using the 0 ps time resolution as can be seen in the higher values in Fig. 99 and Fig. 100, when compared to the 2×1 - setup.

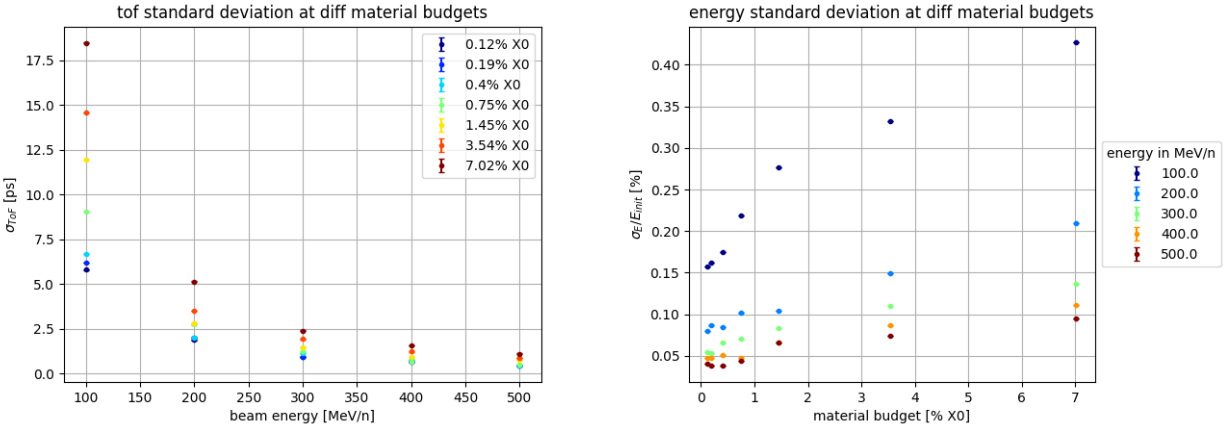

(a) **(b)**

Figure 99: a) ToF standard deviation $\sigma(ToF)$ at different energies and material budgets for helium ions. b) Energy standard deviation $\sigma(E)$ normalized to the beam energy E_{init} at different energies and material budgets for helium ions.

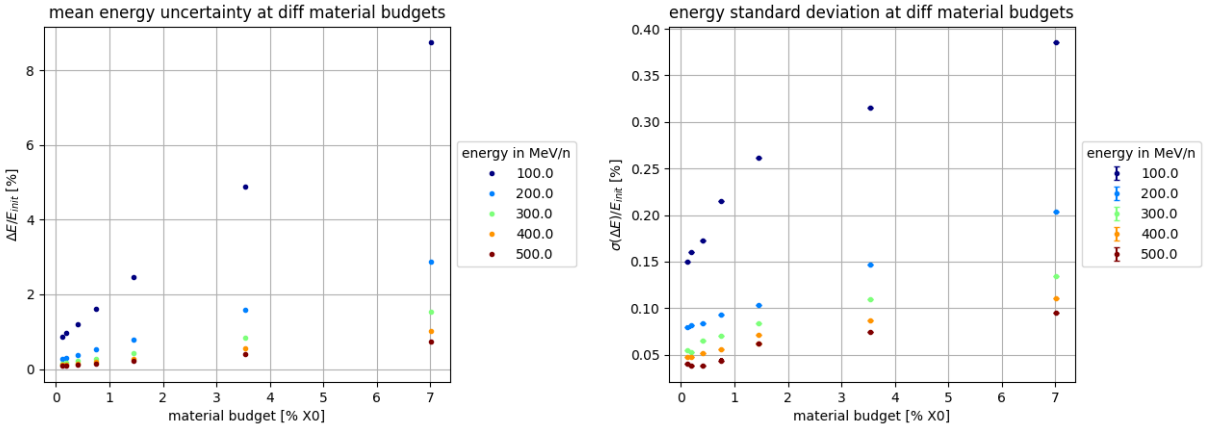

(a) **(b)**

Figure 100: a) Mean energy uncertainty ΔE for helium ions. b) Energy standard deviation $\sigma(\Delta E)$ for helium ions. Both plots are normalized to the beam energy E_{init}.

5.2.17 Material budget with 2x2 planes, helium ions, 30 ps time resolution

In the 30 ps time resolution case, the results in Fig. 101a and Fig. 101b show the expected $\sqrt{2}$ improvement to the results obtained by the setup with only 2 planes. The mean energy uncertainty ΔE, as can be seen in Fig. 102a, presents on the one side the dominating influence of the scattering at low energies and on the other side the $\sqrt{2}$-improvement at high energies when compared to the 2×1 - setup. For the standard deviation of the energy uncertainty $\sigma(\Delta E)$, the $\sqrt{2}$-improvement is visible, while at 100 MeV the results show an increase in their value until an intermediate maximum at 1.45 % X0 and a decreasing afterwards. This behaviour could be observed before at the 2×1 - setup (Fig. 80b).

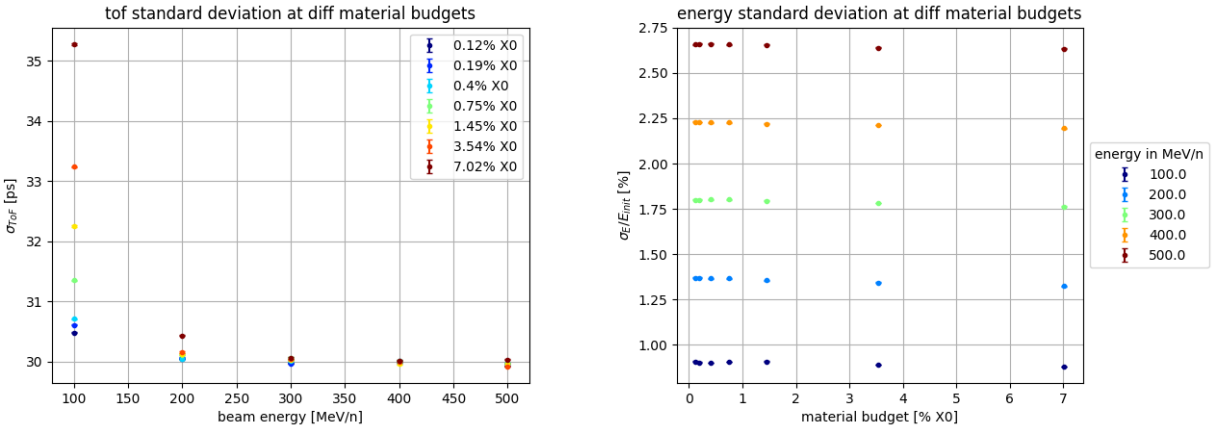

(a) (b)

Figure 101: a) ToF standard deviation $\sigma(ToF)$ at different energies and material budgets for helium ions. b) Energy standard deviation $\sigma(E)$ normalized to the beam energy E_{init} at different energies and material budgets for helium ions.

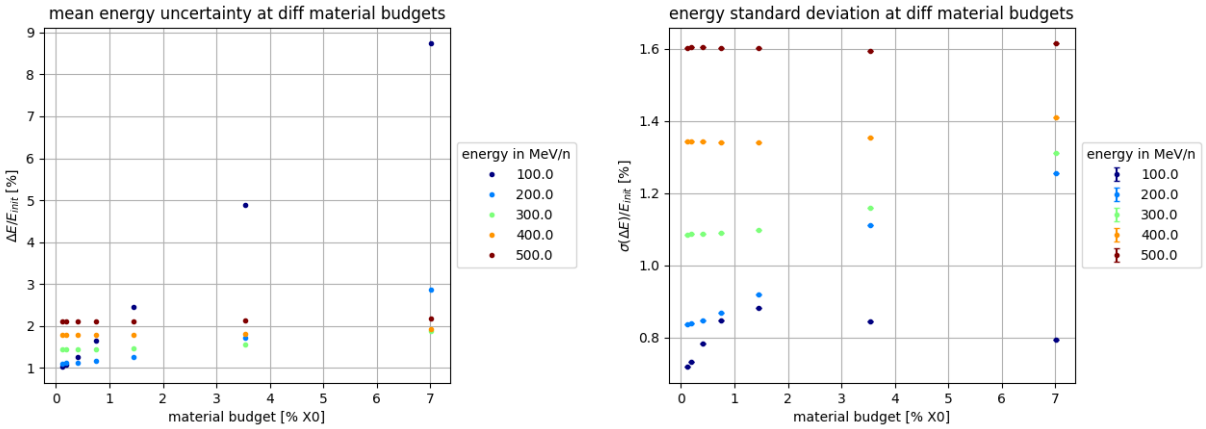

(a) (b)

Figure 102: a) Mean energy uncertainty ΔE for helium ions. b) Energy standard deviation $\sigma(\Delta E)$ for helium ions. Both plots are normalized to the beam energy E_{init}.

5.3 Comparison of protons, $^{12}C^{6+}$ carbon ions and alpha particles

To compare the results of protons, $^{12}C^{6+}$ carbon ions and alpha particles, a simulation of a realistic ToF setup was done with the following specifications:

- world material: air
- beam source: 1 cm in front of LGAD 1
- beam spot size: 2×2 mm
- primary particles: 1 Mio.
- number of LGADs: 2×2
- LGAD area: $1\,\text{m} \times 1\,\text{m}$
- ToF distance: 1 m
- time resolution: $\sigma_t = 30\,\text{ps}$
- spatial resolution: $\sigma_x = \sigma_y = 100\,\mu\text{m}$
- material budget: 0.4 % X0

Fig. 103a presents the results on the ToF standard deviation σ_{ToF}, where the most significant deviation can be seen in the low energy region. While the standard deviation for protons reaches a value of $\sigma_{ToF} = 33.4\,\text{ps}$ at 100 MeV, the alpha particles occupy a much lower value and the $^{12}C^{6+}$ carbon ions can be obtained at $\sigma_{ToF} = 30.3\,\text{ps}$ for 83 MeV/n. In Fig. 103b, it can be seen that the energy standard deviation for all three particle types has a linear dependency on the beam energy and does not differ between protons, $^{12}C^{6+}$ carbon ions and alpha particles. In the low energy region of Fig. 104a and Fig. 104b the effects of scattering and its influnce on the mean energy uncertainty ΔE and the respective energy standard deviation $\sigma(\Delta E)$, as well as the differences of the particle types can be seen. Because of the high rest mass of $\sim 11.175\,\text{GeV}$ for $^{12}C^{6+}$ carbon ions compared to the rest mass of protons ($\sim 938\,\text{MeV}$) the effect of scattering at low energies is more pronounced and therefore gives higher values for ΔE and $\sigma(\Delta E)$. The alpha particles, though having a rest mass of $\sim 3.727\,\text{GeV}$, show similar results compared to protons, while the standard deviation $\sigma(\Delta E)$ is slightly lower for energies $< 300\,\text{MeV/n}$.

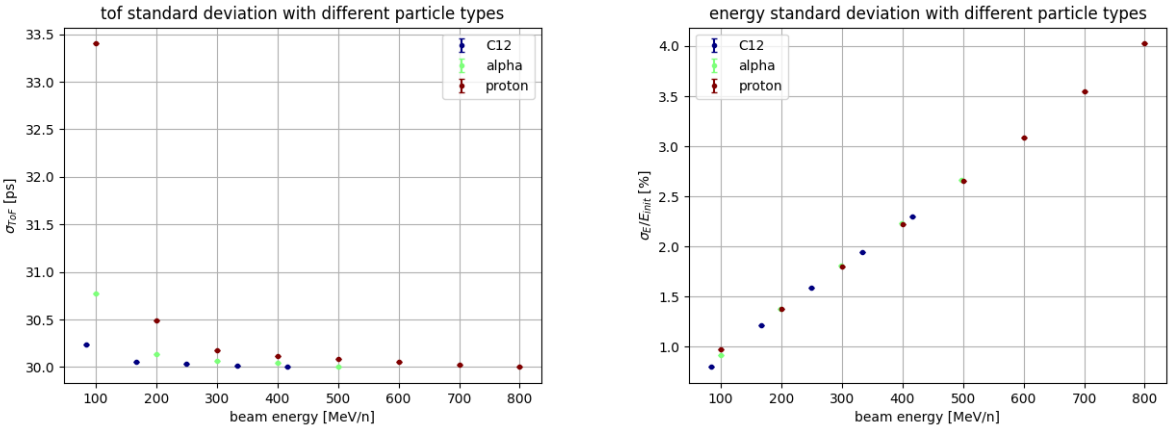

(a) **(b)**

Figure 103: Comparison of protons, alpha particles (helium ions) and $^{12}C^{6+}$ carbon ions. a) ToF standard deviation $\sigma(ToF)$ at different energies per nucleon. b) Energy standard deviation $\sigma(E)$ normalized to the beam energy E_{init} at different energies per nucleon.

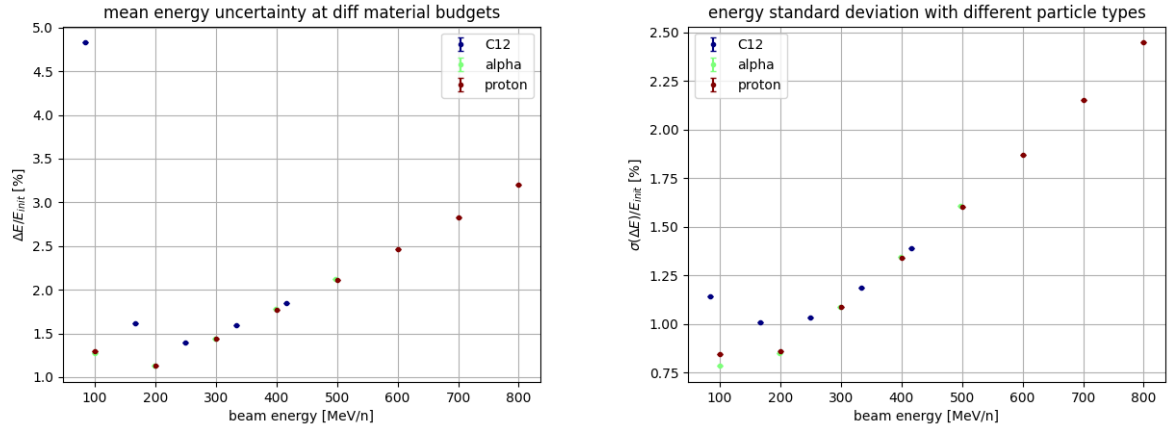

(a) **(b)**

Figure 104: Comparison of protons, alpha particles (helium ions) and $^{12}C^{6+}$ carbon ions. a) Mean energy uncertainty ΔE and b) Energy standard deviation $\sigma(\Delta E)$. Both plots are normalized to the beam energy E_{init}.

6 Summary and conclusion

Based on two low gain avalanche detectors (LGAD), a time-of-flight calorimeter to obtain the residual energy in a proton computed tomography experiment was studied. In order to resolve the energy differences of the residual beam, the time resolution of the LGADs and the time-of-flight resolution had to be found. The first approach was to set up an experiment at the MedAustron proton therapy center, where the two detectors were situated on a rack with a distance of 2.5 cm apart from each other centered in beam direction to provide hits on the sensitive parts of the sensors. In the first two shifts of the experiment, the signals of the LGADs, when being hit by protons or $^{12}C^{6+}$ carbon ions, were additionally amplified by second stage amplifiers (cividec) and recorded by the oscilloscope. The produced data was then analyzed offline by the help of a software algorithm written in C++ with the help of the Root Data Analysis Framework. To interpret the results, first, a study on the deposited energy inside the detectors was compared to the theoretical values of the Bethe-Bloch equation via the PSTAR database as well as the results from the simulation and showed a difference in the results. These deviations lead to further necessary experiments at the HEPHY institute, where the proton beam was exchanged by a laser pulse to understand the behaviour of the LGAD and its readout circuit better. It could be shown that the second stage amplifier was not able to amplify the whole bandwidth of amplitudes of the signals and caused damping, so that the main deviation between theory and experiment could be explained. Further results of the laser tests showed that the on board amplification of the LGADs revealed differences in their strength and due to the quantification of these differences can be avoided in future experiments by choosing a different bias voltage. Besides these findings, the bandwidth settings of the oscilloscope were analyzed with the result that the best option for recording the signals is at 1 GHz. While the time resolution of the first two MedAustron shifts has not been better than 56.17 ps, the new settings from the laser test lead to a time resolution of 52 ps per LGAD in the third shift, where a bias voltage of 350 V generally presented better results. The minimum of the rise time of the signal was measured at 800 MeV with a value of 486 ps. The results of the laser tests presented in the project work ("Optimization of a laser setup for characterizing Low Gain Avalanche Silicon Detectors") showed the sufficiency of a rise time of 500 ps for providing an excellent time resolution.
Besides the irradiation with protons, also $^{12}C^{6+}$ carbon ions were used at MedAustron and despite a higher rise time of 543 ps, the time resolution reached minimum values between 43 ps and 44 ps for each LGAD. It was also shown that with a lower bias voltage of 200 V, a better time resolution could be achieved. While in the fourth shift the best choice of the oscilloscope bandwidth of 1 GHz could be confirmed, an even higher bias voltage of 360 V is the most suitable for providing time resolutions in the range of 55 ps, but could not be set to a higher level due to unstable behaviour when reaching the breakthrough voltage range.
In all the experiments at MedAustron, the time-of-flight was not steady and lead to values with high deviation. This could be explained afterwards by running the simulations of the identical setup with Geant4, where the ToF distance of 2.5 cm has proved to be too small and introduced significant uncertainties.
This led to the new strategy of finding an ideal ToF setup by the help of the simulation, where parameters could easily be changed and the effects could be shown. As was obtained in Sec. 5.1, a ToF distance of 1 m was chosen, because the relative time uncer-

tainty gets significantly higher with lower flight distance and 1 m is a distance that could easily be assembled in a real experiment without being oversized to the experimental facilities. The number of detected particles depends on the initial beam's spotsize and the size of the sensitive area of the LGADs due to scattering on the first detector. Other parameters are the beam energy and the type of particles, where protons show the lowest percentage of detection, because of the lower mass compared to $^{12}C^{6+}$ carbon ions and helium ions (alpha particles). For all three particle types and the two beam spotsizes (2×2 mm and 8×8 mm), an LGAD size of 40 mm covers $> 90\%$ of detection efficiency with beam energies ≥ 200 MeV and $> 80\%$ at < 200 MeV. An exception are protons and alpha particles at lower energies(< 100 MeV) and 8×8 mm beam spotsize, giving only $> 40\%$ of detection efficiency with a sensitive area of 40×40 mm, because of the high scattering angle.
The spatial resolution of an LGAD detector for an optimised ToF setup has to be ≤ 10 mm for a ToF distance of 1 m. As explained in detail in Sec. 5.2.9, the influence of the spatial resolution on the energy standard deviation and energy uncertainty is tiny for values under ≤ 10 mm, but give high deviating results when this dimension is exceeded. This applies for protons, $^{12}C^{6+}$ carbon ions and alpha particles as well as for the whole used range of material budgets reaching from $0.1\,\% - 34.9\,\%$X0.
Due to an increasing material budget of the detector, the scattering angle of the particles penetrating it increases too. This effect is a major factor for uncertainties in time- and energy standard deviation. The two LGADs, that were used in the real experiments, have a material budget of 0.7 %X0, but in the simulation, values from 0.1 %X0 to 34.7 %X0 were studied. To reach a ToF standard deviation of ≤ 10 ps, a material budget < 1.0 %X0 is needed for proton beams, while $^{12}C^{6+}$ carbon ions and alpha particles are much less influenced by the material budget than protons. ToF standard deviation values ≤ 10 ps can be reached with material budgets of up to 3.54 %X0 for carbons and helium ions. The mean energy uncertainty defines the accuracy of the energy, while the energy standard deviation is the precision of the measurement in the simulation. For an energy standard deviation of 1.0 %, a material budget of 14.0 %X0 is sufficient, but the mean energy uncertainty is at 10.0 % for protons. A lower energy uncertainty of 1.0 % with a standard deviation of 0.3 % can be achieved with a material budget of 1.0 %X0.
A time resolution of 30 ps dominates the time- and energy standard deviation, except for lower beam energies (< 200 MeV) and high material budgets, where the scattering still is the major factor for an increase in the standard deviation. The performance of alpha particles is superior to protons, resulting in a ToF standard deviation of ≤ 12 ps and an energy standard deviation of < 0.3 % for material budgets < 7.02 %X0. The mean energy uncertainty with 1.0 % is at a material budget of < 1.0 %X0 at the same level as with protons. The performance of $^{12}C^{6+}$ carbon ions is similar to alpha particles, except for the mean energy uncetainty being at 5.0 % at a material budget of < 1.0 %X0.
An increase of the precision by the factor $\sqrt{2}$ can be achieved with a ToF setup including 2×2 - detector planes, but only by considering a time resolution of ≥ 30 ps, where the scattering effects do not dominate the standard deviations. At a time resolution of 0 ps, the performance is worse with the 2×2 - setup, due to the higher material budget and the resulting incresase of the scattering angle of the particles.
Sec. 5.3 gives an overview of an ideal yet realistic scenario of a ToF-measurement where the energy resolution in Fig. 103b can be used to compare it with results from recent publications [41]. In the stated reference, the energy resolution is 1.0 % for 200 MeV protons, measured with a calorimeter built up by plastic scintillators. In Fig. 103b a

value of 1.4 % can be obtained for 200 MeV protons. In conclusion it can be said that although the energy resolution of the ToF-setup is still higher than the value of the one achieved with the traditional calorimeter, the ToF-measurements with ultra fast silicon detectors can be considered a serious alternative. Especially if the trend of developing more precise and powerful semiconductor detectors will continue.

7 Appendix

7.1 Oscilloscope Datasheet

An extract of the datasheet of the TEKTRONIX-DSA70804B oscilloscope is given on the next 4 pages with information about the vertical-, time base- and the acquisition system, as well as about the time resolution and the trigger modes.

Characteristics

Vertical System

DPO/DSA Models	70404B	70604B	70804B	71254B	71604B	72004B
Bandwidth (user selectable DSP enhance)	4 GHz	6 GHz	8 GHz	12.5 GHz	16 GHz	20 GHz
Hardware Analog Bandwidth (-3 dB)	4 GHz	6 GHz	8 GHz	12.5 GHz	16 GHz (typical)	16 GHz (typical)
Input Channels	4	4	4	4	4	4
Rise Time 10% to 90% (typical)	98 ps	65 ps	49 ps	32 ps	24.5 ps	19 ps
Rise Time 20% to 80% (typical)	68 ps	45 ps	34 ps	22 ps	17 ps	14 ps
Vertical Noise (% of full scale) (typical)*16	0.28%	0.32%	0.35%	0.38%	0.43%	0.77%
Bandwidth Limits	Depending on instrument model: 19 GHz, 18 GHz, 17 GHz, 16 GHz, 15 GHz, 14 GHz, 13 GHz, 12 GHz, 11 GHz, 10 GHz, 9 GHz, 8 GHz, 7 GHz, 6 GHz, 5 GHz, 4 GHz, 3 GHz, 2 GHz, 1 GHz, or 500 MHz					
Channel-to-channel Isolation (Any Two Channels at Equal Vertical Scale Settings)	≥120:1 (for input frequency 0 to 10 GHz) ≥80:1 (for input frequency >10 GHz to 12 GHz. ≥50:1 (for input frequency >12 GHz to 15 GHz) ≥25:1 (for input frequency >15 GHz)					
DC Gain Accuracy	±2% (of reading)					
Delay between any two channels (typical)	≤100 ps for any two channels with equal V/div and coupling settings ≤50 ps with BW enhance enabled (BW+)					
Effective Number of Bits (typical)	5.4 bits*14					
Input Coupling	DC (50 Ω), GND					
Input Impedance	50 Ω ±2%, 1 MΩ with TCA-1MEG adapter					
Input Sensitivity 18 GHz and below 20 GHz and 19 GHz	 10 mV/div to 500 mV/div (100 mV to 5 V full scale) 20 to 500 mV/div (200 mV to 5 V full scale)					
Max Input Voltage, 50 Ω	<5.0 V_{RMS} for ≥100 mV/div; also determined by TekConnect accessory 1.0 V_{RMS} for <100 mV/div					
Offset Accuracy	10 mV/div – 99.5 mV/div. ±(0.35% (offset value-position) + 1.5 mV + 1% of full scale) 100 mV/div – 500 mV/div. ±(0.35% (offset value-position) + 7.5 mV + 1% of full scale)					
Offset Range	10 mV/div: ±450 mV 20 mV/div: ±400 mV 50 mV/div: ±250 mV 100 mV/div: ±2.0 V 200 mV/div: ±1.5 V 500 mV/div: ±0.0 V					
Passband Flatness (20, 50, 100, 250 mV/div) (typical)	±0.5 dB to 50% of nominal bandwidth at 25 °C					
Position Range	±5 div					
Vertical Resolution	8 bit (11 bit with averaging)					

*14 50 mV/div, bandwidth filter on, max bandwidth up to 13 GHz, max sample rate

*16 50 mV/div, bandwidth filter on

Time Base System

DPO/DSA Models	70404B	70604B	70804B	71254B	71604B	72004B
Time Base Range	20 ps/div to 1000 s/div			10 ps/div to 1000 s/div		
Time Resolution (in ET/IT mode)	200 fs			100 fs		
Channel-to-channel Deskew	Range ±75 ns					
Delta Time Measurement Accuracy RMS Over <100 ns duration; single shot; with signal rise time = 1.2X scope rise time	1.61 ps	1.29 ps	1.14 ps	940 fs	900 fs	1.02 ps
Jitter Noise Floor (typical) (With BW+ bandwidth enhance enabled)	450 fs	450 fs	450 fs	300 fs	300 fs	400 fs
Time Base Accuracy	±1.5 ppm initial accuracy, aging <1 ppm per year					
Time Base Delay Time Range	-5.0 ks to 1.0 ks					
Trigger Jitter (RMS)	1 ps_{RMS} (typical) with enhanced triggering OFF <100 fs_{RMS} with enhanced triggering ON					

Acquisition System

DPO/DSA Models	70404B / 70604B / 70804B	71254B / 71604B / 72004B
Sample Rates		
Real-time mode 1, 2, 3, or 4 channel (max)	25 GS/s	50 GS/s
ET/IT Mode (max)	5 TS/s	10 TS/s
Maximum Record Length per Channel		
With Standard Configuration	10 M on all four channels (DPO70000B Series only) 20 M on all four channels (DSA70000B Series only)	
With Record Length Opt. 2XL	20 M on all four channels (DPO70000B Series only)	
With Record Length Opt. 5XL	50 M on all four channels	
With Record Length Opt. 10XL	100 M on all four channels	
With Record Length Opt. 20XL	N/A	250 M on all four channels

Maximum Duration at Highest Real-Time Resolution

DPO/DSA Models	70404B / 70604B / 70804B	71254B / 71604B / 72004B
Resolution	40 ps (25 GS/s)	20 ps (50 GS/s)
Max Duration with Standard Memory	0.4 ms DPO70000B Series; 0.8 ms for DSA70000B Series	0.2 ms DPO70000B Series; 0.4 ms for DSA70000B Series
Max Duration with Opt. 2XL	0.8 ms (DPO70000B Series only)	0.4 ms (DPO70000B Series only)
Max Duration with Opt. 5XL	2.0 ms	1.0 ms
Max Duration with Opt. 10XL	4.0 ms	2.0 ms
Max Duration with Opt. 20XL	N/A	5.0 ms

Acquisition Modes

Mode	Description
Averaging	From 2 to 10,000 waveforms included in average
Envelope	From 1 to 2×10^9 waveforms included in min-max envelope
FastAcq Acquisition Mode	FastAcq optimizes the instrument for analysis of dynamic signals and capture of infrequent events
Maximum FastAcq Waveform Capture Rate	>300,000 wfms/s on all 4 channels simultaneously
FastFrame™ Acquisition	Acquisition memory divided into segments; maximum trigger rate >310,000 waveforms per second. Time of arrival recorded with each event. Frame finder tool helps to visually identify transients.
Hi-Res	Real-time boxcar averaging reduces random noise and increases resolution
Peak Detect	Captures narrow glitches at all real-time sampling rates: 1 ns at ≤125 MS/s; 1/sample rate at ≥250 MS/s
Roll Mode	Up to 10 MS/s with a maximum record length of 40 MS
Sample	Acquire sampled values
Waveform Database	Accumulate waveform database providing three-dimensional array of amplitude, time, and counts

Pinpoint® Trigger System

	DPO Models 70404B / 70604B / 70804B / 71254B / 71604B / 72004B	DSA Models 70404B / 70604B / 70804B / 71254B / 71604B / 72004B
Sensitivity		
Internal DC Coupled	4% of full scale from DC to 50 MHz 10% of full scale at 4 GHz 20% of full scale at 8 GHz 50% of full scale at 11 GHz	
External (Auxiliary Input) 50 Ω	250 mV from DC to 50 MHz, increasing to 350 mV at 1.0 GHz.	
Trigger Characteristics		
A Event and Delayed B Event Trigger Types	Edge, Glitch, Runt, Width, Transition Time, Time-out, Pattern, State, Setup/Hold, Window—all except Edge, Pattern, and State can be Logic State qualified by up to two channels	
Main Trigger Modes	Auto, Normal, and Single	
Trigger Sequences	Main, Delayed by Time, Delayed by Events, Reset by Time, Reset by State, Reset by Transition. All sequences can include separate horizontal delay after the trigger event to position the acquisition window in time.	
Clock Recovery System	**Requires Opt. PTH or Opt. MTH**	**Standard**
Clock Recovery Phase Locked Loop Bandwidth	Fixed at FBaud/1600	
Clock Recovery Frequency Range	1.5 MBaud to 3.125 GBaud	
	Requires Opt. PTU	**Requires Opt. STU**
8b10b Max Baud Rate	5 GBaud	
Communications-related Triggers	**Requires Opt. MTH**	**Standard**
	Support for AMI, HDB3, BnZS, CMI, MLT3 and NRZ encoded communications signals. Select among isolated positive or negative one, zero pulse form or eye patterns as applicable to the standard.	
Serial Pattern Trigger	**Requires Opt. PTH**	**Standard**
	Up to 64 bit serial word recognizer, bits specified in binary (high, low, don't care) or hex format. Trigger on NRZ-encoded data up to 1.25 GBaud.	
	Trigger on 8b/10b-encoded data from 1.25 to 3.125 GBaud (40 bits)	
	Requires Opt. PTU	**Requires Opt. STU**
	Trigger on 8b/10b-encoded data up to 5 GBaud (40 bits)	
AUX Trigger	TekConnect interface: ±5 V	
Clock Recovery Jitter (RMS)	<0.25% bit period + 2 ps_{RMS} for PRBS data patterns <0.25% bit period + 1.5 ps_{RMS} for repeating "0011" data pattern	
Enhanced Triggering	User-selectable; enhanced triggering corrects the difference in timing between the trigger path and the acquired data path (supports all Pinpoint trigger types on both A- and B-Events except pattern trigger); Not available in FastAcq.	
Line	Fixed at 0 V	
Minimum Signal Amplitude needed for Clock Recovery	1 div_{p-p} up to 1.25 Gbaud 1.5 div_{p-p} above 1.25 Gbaud	
Tracking/Acquisition Range	±2% of requested baud	
Trigger Coupling	DC, AC (attenuates <100 Hz), HF Rej (attenuates >20 kHz), LF Rej (attenuates <200 kHz), Noise Reject (reduces sensitivity)	
Trigger Holdoff Range	250 ns min to 12 s max	
Trigger Level Range Internal	±120% of full scale from center of screen	

Trigger Modes

Mode	Description
Comm	Standard feature on the DSA70000B, provided as part of Opt. MTH on the DPO70000B Series. Support for AMI, HDB3, BnZS, CMI, MLT3 and NRZ encoded signals.
Edge	Positive or negative slope on any channel or front panel auxiliary input. Coupling includes DC, AC, noise reject, HF reject, and LF reject.
Glitch	Trigger on or reject glitches of positive, negative, or either polarity. Minimum glitch width is down to 150 ps (typical) with rearm time of 300 ps
Pattern	Trigger when pattern goes false or stays true for specified period of time. Pattern (AND, OR, NAND, NOR) specified for four input channels defined as high, low, or don't care.
Runt	Trigger on a pulse that crosses one threshold but fails to cross a second threshold before crossing the first again. Event can be time- or logic-qualified.
Serial Pattern	Trigger on NRZ-encoded data up to 3.125 Gbaud (5 Gbaud with Opt. PTU or Opt. STU); above 1.25 Gbaud requires 8b/10b encoded data. Extended with pattern lock triggering to capture repeated acquisitions of long serial test patterns up to 6.25 Gbps.
Setup/Hold	Trigger on violations of both setup time and hold time between clock and data present on any two input channels.
State	Any logical pattern of channels (1, 2, 3) clocked by edge on channel 4. Trigger on rising or falling clock edge.
Time-out	Trigger on an event which remains high, low, or either, for a specified time period. Selectable from 300 ps.
Transition	Trigger on pulse edge rates that are faster or slower than specified. Slope may be positive, negative, or either.
Trigger Delay by Events	1 to 2 G events
Trigger Delay by Time	3.2 ns to 3 Ms
Width	Trigger on width of positive or negative pulse either within or out of selectable time limits (down to 150 ps).
Window	Trigger on an event that enters or exits a window defined by two user-adjustable thresholds. Event can be time- or logic-qualified.

Search and Mark Events

Event	Description
Basic	Mark any events and document waveforms. Search positive, negative slopes or both on any channels. Event table summarizes all found events. All events are time stamped in reference to trigger position. Users can choose to stop acquisitions when an event is found.
Advanced	Search glitches or runts, as well as transition rate, pulse width, setup and hold, time-out, window violations, or find any logic or state pattern on any number of channels. Search DDR read or write bursts with Opt. DDRA.

Waveform Measurements

Measurement	Description
Automatic Measurements	53, of which 8 can be displayed on screen at any one time; measurement statistics, user-definable reference levels, measurement within gates isolating the specific occurrence within an acquisition to take measurements on.
Amplitude Related	Amplitude, High, Low, Maximum, Minimum, Peak-to-Peak, Mean, Cycle Mean, RMS, Cycle RMS, Positive Overshoot, Negative Overshoot
Combination	Area, Cycle Area, Phase, Burst Width
Eye-pattern Related	Extinction Ratio (absolute, %, dB), Eye Height, Eye Width, Eye Top, Eye Base, Crossing %, Jitter (p-p, RMS, 6sigma), Noise (p-p, RMS), Signal/Noise Ratio, Cycle Distortion, Q-Factor
Histogram Related	Waveform Count, Hits in Box, Peak Hits, Median, Maximum, Minimum, Peak-to-Peak, Mean (μ), Standard Deviation (sigma), μ+1sigma, μ+2sigma, μ+3sigma
Time Related	Rise Time, Fall Time, Positive Width, Negative Width, Positive Duty Cycle, Negative Duty Cycle, Period, Frequency, Delay

Waveform Processing/Math

Processing Type	Description
Algebraic Expressions	Define extensive algebraic expressions including Waveforms, Scalars, User-adjustable Variables and Results of Parametric Measurements e.g. (Integral (CH.1–Mean(CH.1))×1.414×VAR1)
Arithmetic	Add, Subtract, Multiply, Divide Waveforms and Scalars
Filtering Functions	User-definable filters. Users specify a file containing the coefficients of the filter. Several example filter files are provided.
Frequency Domain Functions	Spectral Magnitude and Phase, Real and Imaginary Spectra
Mask Function	A function that generates a Waveform Database pixmap from a sample waveform. Sample count can be defined.
Math Functions	Average, Invert, Integrate, Differentiate, Square Root, Exponential, Log_{10}, Log_{e}, Abs, Ceiling, Floor, Min, Max, Sin, Cos, Tan, ASin, ACos, ATan, Sinh, Cosh, Tanh
Relational	Boolean result of comparison >, <, ≥, ≤, ==, !=
Vertical Units	Magnitude: Linear, dB, dBm
	Phase: Degrees, radians, group delay
	IRE and mV units
Waveform Definition	As an arbitrary math expression
Window Functions	Rectangular, Hamming, Hanning, Kaiser-Bessel, Blackman-Harris, Gaussian, Flattop2, Tek Exponential

Display Characteristics

Characteristic	Description
Color Palettes	Normal, Green, Gray, Temperature, Spectral, and User-defined
Display Format	YT, XY
Display Resolution	XGA 1024 horizontal × 768 vertical pixels
Display Size	Diagonal: 307.3 mm (12.1 in.)
Display Type	Liquid crystal active-matrix color display
Horizontal Divisions	10
Vertical Divisions	10
Waveform Styles	Vectors, Dots, Variable Persistence, Infinite Persistence

7.2 Amplifier Datasheet

An overview of the technical specifications of the cividec amplifier is given below.

C2-HV Broadband Amplifier, 2 GHz, 40 dB

This **40 dB Broadband Amplifier** is a low-noise current amplifier with an analog bandwidth of 2 GHz. Its speed is optimized for use as a front-end amplifier for diamond detectors. A Bias-Tee is integrated for the supply of the detector.

Parameters:	
Type:	Current amplifier
Analog bandwidth:	1 MHz – 2 GHz
Gain:	40 dB
Input coupling:	AC coupled (1 nF @ 1 kV)
Input impedance:	50 Ω
Input protection:	IEC61000-4-2 (±8 kV, 2 A for 1 µs)
Input polarity:	Bipolar
Output polarity:	Non-inverting, bipolar
Linear output voltage range:	±1 V
Output impedance:	50 Ω
Equivalent input current noise (rms):	0.4 µA

Power supplies:	
Supply voltage:	+12 V
Current consumption:	100 mA

Housing:	
Box size:	85 mm × 55 mm × 15 mm
Box material:	Aluminium with extra RF shielding
Signal input and output connectors:	SMA female
12 V power connector:	Lemo ERA.0S.302.CLL
Detector bias voltage connector:	Lemo ERA.00.250.NTL

7.3 LGAD Board Electrical Layout

The electrical layout scheme is shown on the next 2 pages including the information about the electrical devices and the connections. Additionally, the layout of the first stage amplifier can be seen on page 2 of the layout.

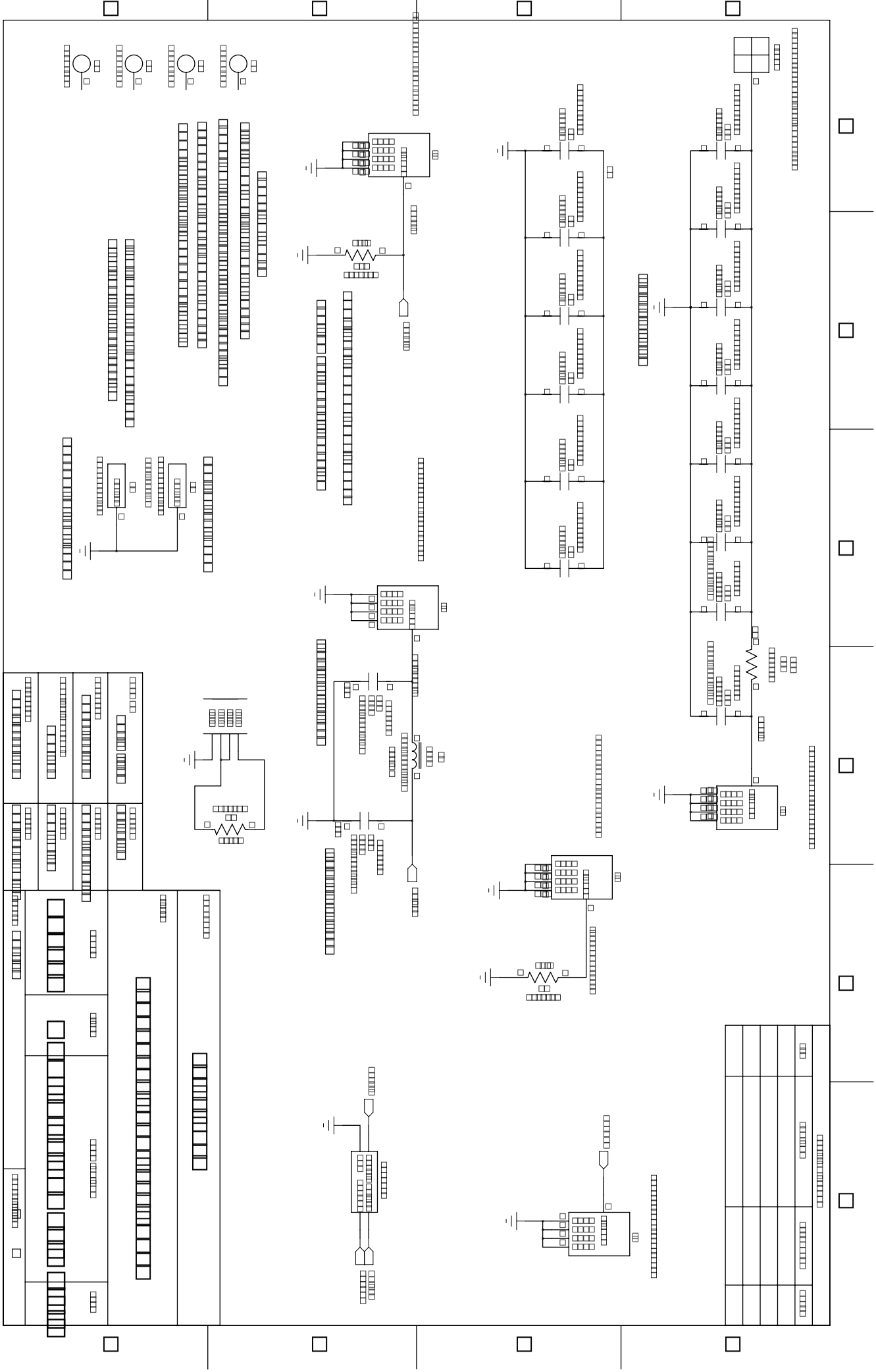

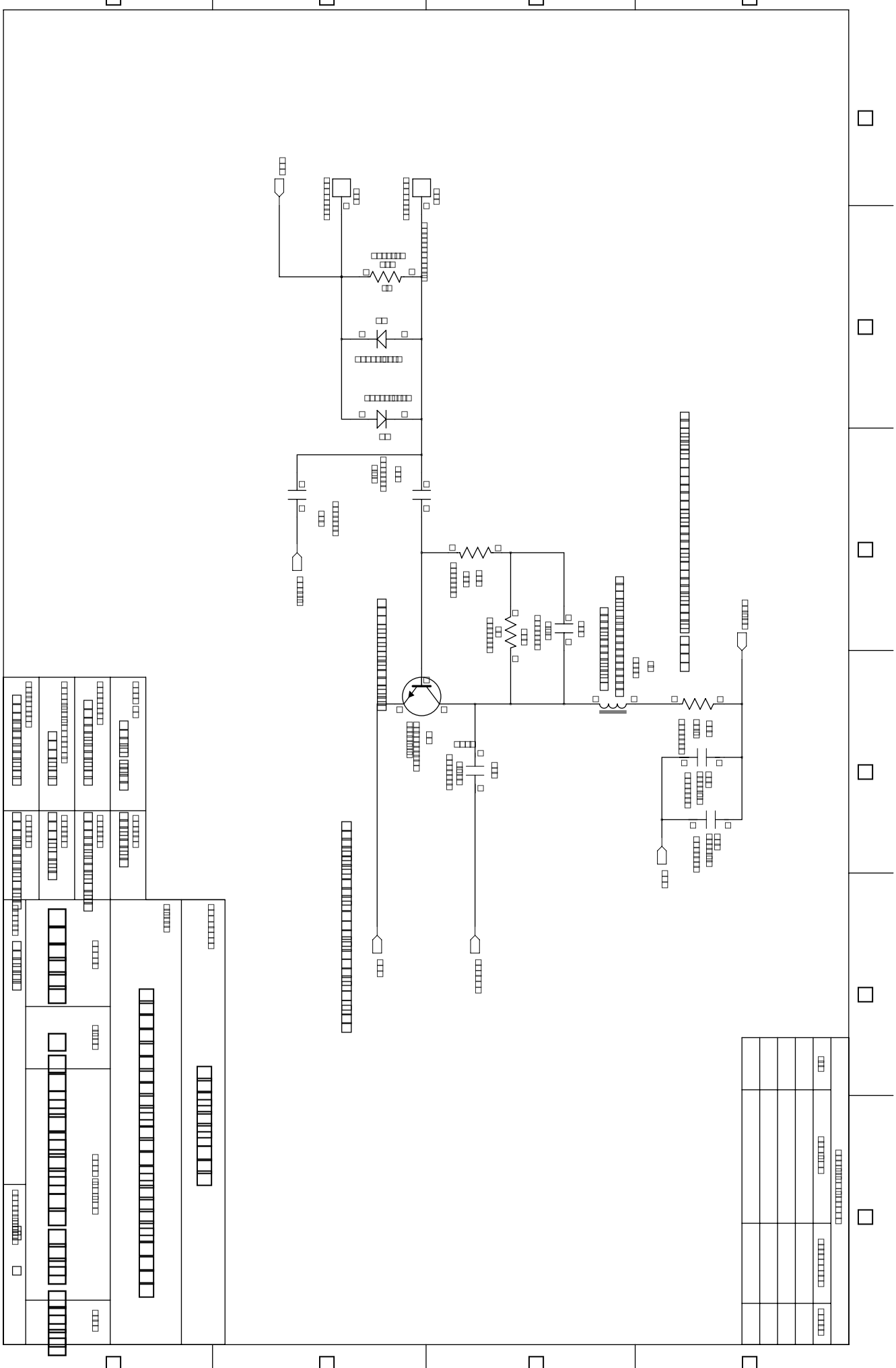

List of Figures

References

[1] Robert R. Wilson. Radiological Use of Fast Protons. *Radiology*, 47:487–491, Nov 1946. doi: 10.1148/47.5.487. URL https://pubs.rsna.org/doi/abs/10.1148/47.5.487.

[2] Alfred R Smith. Proton therapy. *Physics in Medicine and Biology*, 51(13):R491–R504, jun 2006. doi: 10.1088/0031-9155/51/13/r26. URL https://doi.org/10.1088%2F0031-9155%2F51%2F13%2Fr26.

[3] Giacometti et. al. Development of a high resolution voxelised head phantom for medical physics applications. *Physica Medica*, 33, 01 2017. doi: 10.1016/j.ejmp.2017.01.007.

[4] George Dedes et. al. Experimental comparison of proton CT and dual energy x-ray CT for relative stopping power estimation in proton therapy. *Physics in Medicine & Biology*, 64(16):165002, aug 2019. doi: 10.1088/1361-6560/ab2b72. URL https://doi.org/10.1088%2F1361-6560%2Fab2b72.

[5] C. Civinini et. al. Proton Computed Tomography: iterative image reconstruction and dose evaluation. *Journal of Instrumentation*, 12(01):C01034–C01034, jan 2017. doi: 10.1088/1748-0221/12/01/c01034. URL https://doi.org/10.1088%2F1748-0221%2F12%2F01%2Fc01034.

[6] PSTAR. Stopping Power Calculation Program. date accessed: 12-11-2020. URL https://physics.nist.gov/PhysRefData/Star/Text/PSTAR.html.

[7] Stefanie Kaser. Geant4 Simulations for Ion CT Image Reconstruction. *TU Wien Universitätsbibliothek*, Oct. 2019. URL https://repositum.tuwien.at/handle/20.500.12708/3190.

[8] Li et. al. Reconstruction for proton computed tomography by tracing proton trajectories: A Monte Carlo study. *Medical physics*, 33:699–706, 04 2006. doi: 10.1118/1.2171507.

[9] Scott Penfold and Censor. Techniques in Iterative Proton CT Image Reconstruction. *Sensing and Imaging*, 16, 10 2015. doi: 10.1007/s11220-015-0122-3.

[10] T. Bergauer. Teilchendetektoren VO. date accessed: 09-07-2020. URL https://www.oeaw.ac.at/hephy/ausbildung/studierende/lehrveranstaltungen/teilchendetektoren-bergauer.

[11] Hermann Kolanoski and Norbert Wermes. *Teilchendetektoren*. Springer, 2016. ISBN 9783662453490, 9783662453506. doi: 10.1007/978-3-662-45350-6.

[12] Safa Kasap. *Principles of Electronic Materials and Devices*. McGraw-Hill, Inc., USA, 3 edition, 2005. ISBN 0073104647.

[13] Frank Hartmann. *Evolution of Silicon Sensor Technology in Particle Physics*. 1615-0430. Springer, Berlin, Heidelberg, 2009. ISBN 978-3-540-44774-0. URL https://doi.org/10.1007/b106762.

[14] Cirrone et. al. A 62MeV proton beam for the treatment of ocular melanoma at Laboratori Nazionali del Sud-INFN. *Nuclear Science, IEEE Transactions on*, 51: 860 – 865, 07 2004. doi: 10.1109/TNS.2004.829535.

[15] Helmuth Spieler. Semiconductor Detector Systems. *Semiconductor Detector Systems*, pages 1–512, 01 2007. doi: 10.1093/acprof:oso/9780198527848.001.0001.

[16] R. Gross and A. Marx. *Festkörperphysik*. Festkörperphysik. De Gruyter, 2012. ISBN 9783486714869. URL `https://books.google.at/books?id=IaVJAAAAQBAJ`.

[17] N. Cartiglia et. al. Tracking in 4 dimensions. *Nuclear Instruments and Methods in Physics Research Section A: Accelerators, Spectrometers, Detectors and Associated Equipment*, 845:47 – 51, 2017. ISSN 0168-9002. URL `http://www.sciencedirect.com/science/article/pii/S0168900216304715`. Proceedings of the Vienna Conference on Instrumentation 2016.

[18] Hartmut F-W Sadrozinski, Abraham Seiden, and Nicolò Cartiglia. 4d tracking with ultra-fast silicon detectors. *Reports on Progress in Physics*, 81(2):026101, dec 2017. doi: 10.1088/1361-6633/aa94d3. URL `https://doi.org/10.1088%2F1361-6633%2Faa94d3`.

[19] Sola et. al. First FBK Production of 50μm Ultra-Fast Silicon Detectors. *Nuclear Instruments and Methods in Physics Research Section A: Accelerators, Spectrometers, Detectors and Associated Equipment*, 02 2018. doi: 10.1016/j.nima.2018.07.060. URL `https://doi.org/10.1016/j.nima.2018.07.060`.

[20] G. Pellegrini et. al. Recent technological developments on LGAD and iLGAD detectors for tracking and timing applications. *Nuclear Instruments and Methods in Physics Research Section A: Accelerators, Spectrometers, Detectors and Associated Equipment*, 831:24 – 28, 2016. ISSN 0168-9002. URL `http://www.sciencedirect.com/science/article/pii/S0168900216304557`. Proceedings of the 10th International "Hiroshima" Symposium on the Development and Application of Semiconductor Tracking Detectors.

[21] C. Gallrapp, M. Fernández García, Salvador Hidalgo, Isidre Mateu, Michael Moll, S. Ugobono, and Giulio Pellegrini. Study of gain homogeneity and radiation effects of Low Gain Avalanche Pad Detectors. *Nuclear Instruments and Methods in Physics Research Section A: Accelerators, Spectrometers, Detectors and Associated Equipment*, 875, 08 2017. doi: 10.1016/j.nima.2017.07.038.

[22] Apresyan et. al. Studies of the FBK Low-Gain Avalanche Detectors for the CMS Endcap Timing Layer. *U.S. Department of Energy*, 1 2019.

[23] G Poludniowski, N M Allinson, and P M Evans. Proton radiography and tomography with application to proton therapy. *The British Journal of Radiology*, 88(1053): 20150134, 2015. doi: 10.1259/bjr.20150134. URL `https://doi.org/10.1259/bjr.20150134`. PMID: 26043157.

[24] Robert P Johnson. Review of medical radiography and tomography with proton beams. *Reports on Progress in Physics*, 81(1):016701, nov 2017. doi: 10.1088/1361-6633/aa8b1d. URL `https://doi.org/10.1088%2F1361-6633%2Faa8b1d`.

[25] Berretti et. al. Test of Ultra Fast Silicon Detectors for the TOTEM upgrade project. *Journal of Instrumentation*, 12:P03024–P03024, 03 2017. doi: 10.1088/1748-0221/12/03/P03024.

[26] A. Vignati et. al. Innovative thin silicon detectors for monitoring of therapeutic proton beams: preliminary beam tests. *Journal of Instrumentation*, 12(12):C12056–C12056, dec 2017. doi: 10.1088/1748-0221/12/12/c12056. URL `https://doi.org/10.1088%2F1748-0221%2F12%2F12%2Fc12056`.

[27] Stock et. al. Development of Clinical Programs for Carbon Ion Beam Therapy at MedAustron. *International Journal of Particle Therapy*, 2, 10 2015. doi: 10.14338/IJPT-15-00022.1.

[28] Michael Benedikt and Albin Wrulich. MedAustron—Project overview and status. *European Physical Journal Plus*, 126:1–11, 07 2011. doi: 10.1140/epjp/i2011-11069-9.

[29] Stock et. al. The technological basis for adaptive ion beam therapy at MedAustron: Status and outlook. *Zeitschrift für Medizinische Physik*, 28, 10 2017. doi: 10.1016/j.zemedi.2017.09.007.

[30] Felix K. V. Ulrich-Pur. Simulation and optimization of a proton computed tomography setup at MedAustron. *TU Wien Universitätsbibliothek*, June 2018. URL `https://repositum.tuwien.at/handle/20.500.12708/3418`.

[31] cividec. cividec C2-HV broadband amplifier. date accessed: 09-07-2020. URL `https://cividec.at/electronics-C2-HV.html`.

[32] Agostinelli et. al. Geant4—a simulation toolkit. *Nuclear Instruments and Methods in Physics Research Section A: Accelerators, Spectrometers, Detectors and Associated Equipment*, 506:250–303, 11 2002. doi: 10.2172/799992.

[33] Olga Yevseyeva et. al. GEANT4 Tuning For pCT Development, 2011.

[34] J. Allison et. al. Recent developments in Geant4. *Nuclear Instruments and Methods in Physics Research Section A: Accelerators, Spectrometers, Detectors and Associated Equipment*, 835:186 – 225, 2016. ISSN 0168-9002. URL `http://www.sciencedirect.com/science/article/pii/S0168900216306957`.

[35] Maria Grazia Pia and Georg Weidenspointner. Monte Carlo Simulation for Particle Detectors, 2012.

[36] L L Carter and E D Cashwell. *Particle-transport simulation with the Monte Carlo method*. U. S. Department of Energy, 1 1975. ISBN 978-0-87079-021-8.

[37] Mark Thomson. *Modern Particle Physics*. Cambridge University Press, 2013. ISBN 978-1-107-03426-6.

[38] P.A.Zyla et al. (Particle Data Group). Atomic and Nuclear Properties of Materials. `http://pdg.lbl.gov/2019/AtomicNuclearProperties/index.html`, 2020. Accessed: 2020-10-30.

[39] Flavio Tosello. SDD Materials G10-FR4. http://personalpages.to.infn.it/~tosello/EngMeet/ITSmat/SDD/SDD_G10FR4.html, 2019. Accessed: 2020-10-30.

[40] Bernard Gottschalk. Radiotherapy proton interactions in matter. 03 2018. URL https://arxiv.org/pdf/1804.00022.pdf.

[41] V. A. Bashkirov, R. W. Schulte, R. F. Hurley, R. P. Johnson, H. F.-W. Sadrozinski, A. Zatserklyaniy, T. Plautz, and V. Giacometti. Novel scintillation detector design and performance for proton radiography and computed tomography. *Medical Physics*, 43(2):664–674, 2016. URL https://aapm.onlinelibrary.wiley.com/doi/abs/10.1118/1.4939255.

[42] Markus A. Hennig. Wikimedia n-dotiertes-si, 2006. URL https://commons.wikimedia.org/w/index.php?curid=10515060.

[43] Markus A. Hennig. Wikimedia p-dotiertes-si, 2006. URL https://commons.wikimedia.org/wiki/File:Schema_-_p-dotiertes_Silicium.svg.